

Electrodeposition of Manganese Oxide for Zinc-ion Batteries

By

Arjun Dhiman

A thesis submitted in partial fulfillment of the requirements for the degree of

Master of Science

In

MATERIALS ENGINEERING

Department of Chemical and Materials Engineering

University of Alberta

© Arjun Dhiman, 2019

Abstract

With growing concerns regarding climate change, researchers are focusing on developing energy storage devices to store renewable energy for later use. Currently, lithium-ion batteries (LIBs) dominate the energy storage market, from portable electronics and emerging electric vehicles to grid storage applications. However, issues regarding the increasing cost of LIB materials, limited material supply, and safety concerns have pushed research towards developing safer and more environmentally friendly energy storage devices. Zinc-ion batteries (ZIBs) are the latest battery technology to be explored as an alternative to LIBs. This is largely due to Zn being environmentally benign, abundant, cheap, and possessing a high theoretical capacity. Additionally, ZIBs use aqueous electrolytes, which are safer and more environmentally friendly compared with the organic electrolytes used in LIBs. Still, there are many limitations preventing the wide adoption of ZIBs. In general, many cathode materials used for ZIBs have exhibited poor capacities, poor rate capabilities, poor cycling performance, or a combination of each. This is particularly true for Mn oxide cathode materials. Furthermore, the reaction mechanism for the charge and discharge of ZIBs is not completely understood.

The purpose of this work is to use Mn oxide deposition techniques previously developed in the Ivey research group to develop high performing cathode materials for ZIBs. The first study employed two previously developed Mn oxide electrodeposition techniques to deposit Mn oxide onto stainless steel (SS) substrates to be used as a cathode for ZIBs. The first technique used was a direct anodic electrodeposition technique and the second technique was a pulsed anodic electrodeposition technique. This work was undertaken to determine if ZIBs could be fabricated in the laboratory and achieve comparable results to those observed in the literature. The first deposit was initially characterized using scanning electron microscopy (SEM) and energy

dispersive X-ray spectroscopy (EDS). The Mn oxide was deposited as rods with a flake-like morphology. Cyclic voltammetry (CV) testing and visual inspection showed that the first deposition method was not suitable for use as a cathode and was not pursued further. Samples from the second deposition method were initially characterized using SEM and EDS and showed a flake-like morphology that covered the entire SS surface. Through X-ray diffraction (XRD), the material was identified as a Mn_3O_4 spinel. When assembled into a ZIB, the cathode exhibited a good initial capacity of 287 mAh g^{-1} . However, the capacity quickly faded upon cycling, resulting in a capacity retention of 35.5% after 35 cycles (capacity of 102 mAh g^{-1}). The cathode was examined after the first charge and discharge and exhibited a plate-like morphology after discharge. The plate-like material is most likely zinc sulfate hydroxide (ZSH, $\text{Zn}(\text{OH})_2\cdot 3\text{ZnSO}_4\cdot x\text{H}_2\text{O}$). On charge the ZSH dissolved, however, the morphology of the sample changed. Further materials characterization and electrochemical analysis were not completed due to the poor cycling performance of the material.

The second study continued with the pulsed anodic electrodeposition technique that was explored in the first study. However, carbon paper (CP) was used as the substrate instead of SS. The deposited Mn oxide was initially characterized using SEM and transmission electron microscopy (TEM). The deposited material formed islands that had a flake-like morphology and were nano-crystalline in nature. Through a combination of XRD, X-ray photoelectron spectroscopy (XPS), and Raman spectroscopy (RS), the Mn oxide deposit was identified as Mn_3O_4 . When assembled into a ZIB, the battery showed excellent cyclability with a capacity retention of 139% after 200 cycles at a specific current of 1 A g^{-1} . The battery possessed a maximum capacity of 376 mAh g^{-1} using a specific current of 50 mA g^{-1} . The Mn_3O_4 electrode also showed excellent rate capability performance with capacities of 201, 180, 164, 143, and 217

mAh g⁻¹ at applied specific currents of 300, 600, 1200, 2400, and again at 300 mA g⁻¹, respectively.

Through a combination of electron microscopy, XPS, and electrochemical testing, the results point toward a two-step reaction mechanism for the Mn₃O₄ electrode.

Preface

This thesis is focused on the synthesis, characterization, and electrochemical testing of electrodeposited Mn oxide for use as a cathode for zinc-ion batteries (ZIBs). It should be noted that this work is the first of its kind in this laboratory and is exploratory in nature. The research presented in Chapter 3 and Chapter 4, along with any supporting information is my original work.

Chapter 3 summarizes the work conducted on the electrodeposition of Mn oxide on stainless steel (SS) for use as cathodes in ZIBs. Chapter 4 summarizes the work done with the electrodeposition of Mn oxide on carbon paper (CP) for use as cathodes in ZIBs. Dr. Ivey performed the TEM analysis in both chapters and provided support with editing. Chapter 5 concludes the work completed and provides direction for future work in the area of ZIBs.

A version of Chapter 4 of this thesis has been accepted for publication as follows:

Chapter 4: A. Dhiman and D. G. Ivey, Electrodeposited Manganese Oxide on Carbon Paper for Zinc-ion Battery Cathodes, *Batteries and Supercaps*, 2019, 2, DOI: 10.1002/batt.201900150

Dedication

To my friends and family who have helped to shape me into the person I am today. Their love and support throughout my life is what has made all the difference.

Acknowledgements

First, I would like to thank my supervisor, Dr. Douglas Ivey, for his ongoing support, feedback, and encouragement throughout this project. Particularly, I would like to thank him for his support and encouragement when circumstances surrounding the project and my personal life became very difficult. His love of teaching and helping students grow has shaped me in immeasurable ways.

I would like to thank all the group members of the Ivey Research Group for their guidance, support, and friendship. I am particularly grateful for the support of Michael Clark, who has provided invaluable support and guidance through this entire project. I would like to thank Wendy Thuy, Drew Aasen, and Matthew Labbe for their friendship and help with experiments. I would also like to thank our summer student, Yi Shen for her help with experiments.

For technical support and input, I would like to thank Mr. Shiraz Merali, Dr. Shihong Xu, and Dr. Anqiang He.

Financial support from the Natural Sciences and Engineering Research Council (NSERC) of Canada, Faculty of Graduate Studies and Research (FGSR), and the Graduate Student's Association (GSA) is also gratefully recognized.

Finally, I would like to acknowledge the support of my family and friends for their continued support in all the things I pursue in life. Without them, this process would have been much more difficult.

Table of Contents

Chapter 1: Introduction	1
1.1 Zinc-ion Batteries	1
1.2 Thesis Content	3
Chapter 2: Literature Review	5
2.1 Battery Capacity and Current	5
2.2 Battery Reaction Mechanisms	6
2.2.1 Intercalation Reactions	6
2.2.2 Conversion Reactions	7
2.2.3 Efficiency	8
2.3 Materials Used in Zinc-ion Batteries	8
2.3.1 Anode Material	9
2.3.2 Electrolyte Materials	10
2.3.3 Cathode Materials	12
2.4 Cathode Synthesis Methods	30
2.4.1 Hydrothermal Synthesis	31
2.4.2 Solution Precipitation	31
2.4.3 Electrodeposition	32
2.5 Characterization Techniques	44
2.5.1 X-ray Diffraction	44
2.5.2 Scanning Electron Microscopy	45
2.5.3 Transmission Electron Microscopy	46
2.5.4 X-ray Photoelectron Spectroscopy	47
2.5.5 Raman Spectroscopy	48
2.5.6 Cyclic Voltammetry	49
2.5.7 Galvanostatic Charge and Discharge	51
2.5.8 Electrochemical Impedance Spectroscopy	52
2.5.9 Galvanostatic Intermittent Titration Technique	54

2.6 Previous Work in the Ivey Group	56
2.7 Summary	60
Chapter 3: Electrodeposited Manganese Oxide on Stainless Steel for Zinc-ion Battery	
Cathodes	61
3.1 Introduction	61
3.2 Experimental	62
3.2.1 Material Synthesis and Electrode Preparation	62
3.2.2 Material Characterization	63
3.2.3 Electrochemical Measurements and Battery Testing	63
3.3 Results and Discussion	64
3.3.1 Deposition 1	64
3.3.2 Deposition 2	67
3.4 Summary	73
Chapter 4: Electrodeposited Manganese Oxide on Carbon Paper for Zinc-ion Battery	
Cathodes	75
4.1 Introduction	76
4.2 Experimental	79
4.2.1 Material Synthesis and Electrode Preparation	79
4.2.2 Material Characterization	79
4.2.3 Electrochemical Measurements and Battery Testing	80
4.3 Results and Discussion	81
4.3.1 Material Characterization Results	81
4.3.2 Electrochemical Results	84
4.3.3 Reaction Mechanism	87
4.4 Summary	98
4.5 Supplementary Information	99
Chapter 5: Conclusions and Recommendations	105

5.1 Conclusions	105
5.1.1 Mn Oxide on Stainless Steel (SS) Work	105
5.1.2 Mn Oxide on Carbon Paper (CP) Work	106
5.2 Future Work and Recommendations	106
5.2.1 Optimization of the Cathode and ZIB	106
5.2.2 Reaction Mechanism(s)	107
5.2.3 Synthesis Methods	107
References	109

List of Figures

Figure 1-1 Ragone plot comparing performance of ZIBs and other energy storage devices including Ni-ion batteries (NIB), Ni metal-hydride batteries (Ni-MH), and Ni-Cd batteries [13].	2
Figure 1-2 Schematic of a ZIB. Zn ions are stripped from the Zn plate and are inserted into the α -MnO ₂ electrode on discharge. The reverse occurs on charge. The inset image shows the basic structural unit of α -MnO ₂ , the MnO ₆ octahedron [14].	2
Figure 2-1 Depiction of an intercalation reaction for a LIB occurring in the cathode material on charge and discharge [24].	7
Figure 2-2 Depiction of a conversion reaction for a LIB occurring in the cathode material on charge and discharge [24].	8
Figure 2-3 Crystal structures of Mn oxide materials and their corresponding tunnel size if available. a) β -MnO ₂ (pyrolusite-type), b) R-MnO ₂ (ramsdellite-type), c) γ -MnO ₂ (nsutite-type), d) α -MnO ₂ (hollandite-type), e) romanechite-type MnO ₂ , f) todorokite-type MnO ₂ , g) δ -MnO ₂ (birnessite-type), h) λ -MnO ₂ (spinel-type) [16].	13
Figure 2-4 Summary of the phase transformations of most Mn oxide materials [2]. The green octahedra are MnO ₆ and the red and yellow dots represent O and Zn atoms, respectively. Yellow arrows indicate the new phase upon transformation, with many materials transforming into layered Zn-birnessite. Blue and red arrows indicate other simultaneous phase transformations. Question marks indicate that the phase transformation is unknown. The prohibition sign indicates that the shown transformation does not occur.	14
Figure 2-5 CV curves for two different MnO ₂ cathode battery systems that claim Zn ²⁺ intercalation reaction mechanisms. a) A single pair of redox peaks indicating Zn intercalation into one type of MnO ₂ site using 0.1 M Zn(NO ₃) ₂ electrolyte [57], b) Two pairs of redox peaks indicating Zn intercalation into two different MnO ₂ sites using 1 M ZnSO ₄ electrolyte [28].	16
Figure 2-6 Charge and discharge curves for different ZIBs. a) MnO ₂ on carbon fiber paper in 2M ZnSO ₄ + 0.2M MnSO ₄ electrolyte [39], b) Discharge curves of MnO ₂ in MnSO ₄ solution with and without ZnSO ₄ [39]. Two plateaus are observed for the electrolyte containing both MnSO ₄ and ZnSO ₄ , while only one plateau is observed for the electrolyte containing only MnSO ₄ .	17
Figure 2-7 Cyclic voltammetry curve for Mn ₃ O ₄ in 2M ZnSO ₄ [42]. R ₁ and O ₁ indicate the insertion and removal of Zn ²⁺ , respectively. R ₂ and O ₂ indicate the insertion and removal of H ⁺ , respectively.	18

Figure 2-8 Depiction of the intercalation and conversion discharge reaction mechanism proposed by Li et al. [71]. The reverse occurs on the charge..... 20

Figure 2-9 Cyclability of ZIBs under different conditions [71]. a) Comparison of cyclability of ZIBs with the discharge potential limit of one battery changed to 1.3V, b) Cycling results for ZIBs under different applied current densities..... 21

Figure 2-10 GCD curves for the first two cycles [67]. R and O represent reduction and oxidation reactions, respectively. R2 and O2 indicate where the intercalation mechanism occurs. R1 and O1 indicate where the conversion mechanism occurs. R2 occurs above 1.4 V and R1 occurs below 1.4 V. The first cycle shows a weak R2 plateau above the red line, while the second cycle shows a much stronger R2 plateau. The battery consisted of a MnO₂ cathode, Zn anode, and 2M ZnSO₄ + 0.5M MnSO₄ electrolyte. 21

Figure 2-11 The proposed insertion and conversion reaction mechanism by Huang et al. for MnO₂ cathode based ZIBs [67]. a) First cycle discharge; b) first cycle charge; c) subsequent charge and discharge cycles. 22

Figure 2-12 Structure of Prussian blue analogue CuHCF [48]. The large interstitial sites facilitate Zn²⁺ intercalation. 25

Figure 2-13 Change of V polyhedra structures with the addition of O atoms. Double bonds represent shorter bond lengths [16]..... 26

Figure 2-14 Depiction of the reversible intercalation of water and Zn²⁺ in Zn. Red spheres represent O, blue spheres represent H, and grey spheres represent Zn²⁺. V atoms in VO₆, VO₅, and VO₄ polyhedra are represented as green, purple, and magenta spheres, respectively [38]. 28

Figure 2-15 Plot of operating voltage versus specific capacity of different cathode materials and the Zn anode that have been used for ZIBs [31]...... 30

Figure 2-16 SEM secondary electron (SE) images of electrodeposited MnO₂ by Sun et al. [39]. a)-c) MnO₂ showing uniform coverage of CFP. d) interconnected nanoflake structure of MnO₂. 33

Figure 2-17 Energy level diagram for a molecule depicting the three different types of scattering that can occur [167]. Vibrational state m is at lower energy than vibrational state n. The up arrows indicate the energy of the incident photon and the excitation of the molecule to a virtual state. The down arrows indicate the energy of the scattered photon and the return of the molecule to vibrational states m or n. 49

Figure 2-18 a) Generic CV curve showing peak current (I) and potential (E) positions of the reduction (red) and oxidation (ox) reactions. I_p^{ox} and E_p^{ox} represent the peak current and potential for the oxidation process, respectively. I_p^{red} and E_p^{red} represent the peak current and potential for the reduction process, respectively, b) CV curves for a) reversible, b) quasi-reversible, and c) irreversible electrochemical processes [171]. 51

Figure 2-19 GCD curve for a ZIB tested under increasing applied currents from 1 C to 10 C [21]. The battery was composed of a Zn anode, an α -MnO₂ cathode, and an electrolyte containing 2 M ZnSO₄ and 0.1 M MnSO₄. 52

Figure 2-20 Equivalent circuit diagram and Nyquist plot for a simple battery system [172]. The ohmic resistor determines the high frequency intercept. The small semi-circle is due to the activation losses at the anode which are represented by a resistor and capacitor in parallel. The large semi-circle is due to the activation losses at the cathode. The low frequency diagonal line is from the infinite Warburg element modelling mass transport. 54

Figure 2-21 GITT results for a LIB using a 10 min pulse period, 10 min rest period, and a current of C/10 [178]: a) Full charge and discharge curve under GITT test conditions, b) two consecutive pulse and rest periods for the LIB charge cycle, depicting how ΔE_τ and ΔE_s are determined for diffusion coefficient calculations. 56

Figure 2-22 SEM SE images of plan view and cross section orientations of Mn oxide films deposited using different electrolytes. a) and b) 0.01 M MnSO₄ at 30 mA cm⁻², c) and d) 0.01 M Mn(CH₃COO)₂ at 5 mA cm⁻². Both films were deposited for 10 min at 60°C [179]. 57

Figure 2-23 SEM SE images of Mn oxide deposited using varying deposition times: a, d) 2.5 min, b, e) 5 min, and (c, f) 10 min. All films were deposited at 20 mA cm⁻² and 60°C using a rotation speed of 75 rpm [180]. 58

Figure 2-24 a) and b) SEM SE images of Mn oxide on porous carbon paper [182]. 59

Figure 2-25 SEM SE images of a) and b) unannealed Mn oxide, c) and d) annealed Mn oxide deposits, with the arrow indicating the α -Mn₂O₃ spheres [183]. 60

Figure 3-1 SEM secondary electron (SE) images and EDS spectra: a) and b) low and high magnification images of the deposited Mn oxide sample, c) EDS spectrum for the bare SS substrate, d) EDS spectra of the Mn oxide on the SS substrate. 65

Figure 3-2 CV results for Mn oxide on SS cathode (deposition 1) in a ZIB. The legend indicates the cycle number and the corresponding colour. 66

Figure 3-3 Photographs of Mn oxide on SS sample (deposition 1) a) before CV testing and b) after CV testing. The image on the left in (b) is the separator. 67

Figure 3-4 SEM SE images and EDS spectra: a) and b) low and high magnification images of the deposited Mn oxide sample, c) EDS spectrum for the bare SS substrate, d) EDS spectrum of Mn oxide on the SS substrate. 68

Figure 3-5 XRD pattern for Mn₃O₄ on SS. PDF cards for cubic spinel Mn₃O₄ (PDF#00-013-0162) and hausmannite Mn₃O₄ (PDF#01-071-6262) are superimposed on the pattern. 69

Figure 3-6 Electrochemical and battery performance of Mn₃O₄ on SS in an assembled ZIB: a) CV results at a scan rate of 2 mV s⁻¹ and b) GCD test with the conditioning cycle completed at an applied specific current of 50 mA g⁻¹ and the subsequent cycles at 300 mA g⁻¹. 70

Figure 3-7 a) CV plot showing that the cathodic (discharge) scan was stopped at 1.0 V for analysis, b) SEM SE image showing plate-like formation on the cathode surface, c) STEM annular dark field (ADF) image, d)-g) STEM EDS maps corresponding to the ADF image, and g) STEM EDS map showing an overlay of Zn, Mn, and S data. 71

Figure 3-8 a) CV plot showing that the anodic (charge) scan was stopped at 1.8 V for analysis, b) SEM SE image showing the cathode after the first charge cycle is completed, c) STEM ADF image, d)-g) STEM EDS maps corresponding to the ADF image, g) STEM EDS map showing an overlay of Zn, Mn, and S data. 73

Figure 4-1 Electron microscopy analysis of as deposited Mn₃O₄ on CP: a) and b) SEM secondary electron (SE) images showing island formation and flake-like morphology of Mn₃O₄, c) STEM annular dark field (ADF) image of Mn₃O₄, d)- f) EDS maps for Mn, O, and S in the deposit, g) overlain EDS maps (Mn, O, and S) for Mn₃O₄ deposit showing uniform distribution of Mn and O, h) High resolution TEM image depicting nanocrystalline nature of the deposited Mn₃O₄ with circles indicating some crystalline areas. 81

Figure 4-2 Characterization of as deposited Mn₃O₄: a) Mn 3s XPS spectrum showing the peak splitting used for oxidation state determination, b) Mn 2p XPS spectrum showing two satellite peaks (labeled Mn 3⁺ and Mn 2⁺) used for oxidation state determination, c) XRD pattern and PDF cards for cubic Mn₃O₄ (PDF#00-013-0162) and hausmannite Mn₃O₄ (PDF#01-071-6262), d) Raman spectrum with three peaks labeled. 82

Figure 4-3 Electrochemical and battery performance of assembled ZIB: a) CV results at a scan rate of 0.1 mV s⁻¹, b) GCD testing with the conditioning cycle done at an applied specific current

of 50 mA g⁻¹ and the subsequent cycles at 300 mA g⁻¹, c) battery cyclability results at an applied specific current of 1 A g⁻¹, d) rate capability test results at various applied current densities. 85

Figure 4-4 SEM SE images, STEM ADF images, and STEM EDS maps for the conditioning cycle at different points along discharge and charge: a) discharge point 1 (1.35 V), b) discharge point 2 (1.25 V) with arrows indicating ZSH plates, c) charge point 1 (1.54 V), and d) charge point 2 (1.63 V). The circled particles in b) indicate the Zn-S-O rich particles. The maps shown in the bottom righthand corner for each potential are overlays of Mn, O, Zn, and S. The inset GCD plots depict the positions along the cycle where the battery was stopped for analysis. 89

Figure 4-5 SEM SE images, STEM ADF images, and STEM EDS maps for the 1st cycle after conditioning at different points along discharge and charge: a) discharge point 1 (1.54 V), b) discharge point 2 with the arrows indicating ZSH plates (1.25 V), c) charge point 1 (1.54 V), and d) charge point 2 (1.63 V). The maps shown in the bottom right-hand corner for each potential are overlays of Mn, O, Zn, and S. The inset GCD plots depict the positions along the cycle where the battery was stopped for analysis. 91

Figure 4-6 XPS results for the full conditioning cycle discharge (1.0 V) and charge (1.8 V): a) Discharge survey scan, b) discharge O 1s spectrum, c) discharge Zn Auger LMM peak, d) charge survey scan, e) charge Mn 2p spectrum, f) charge O 1s spectrum, g) charge Mn 3s spectrum, and h) charge Zn Auger LMM spectrum. 93

Figure 4-7 XPS results for the full discharge (1.0 V) and charge (1.8 V) of the 5th cycle after conditioning: a) Discharge survey scan, b) discharge O 1s spectrum, c) discharge Zn Auger LMM spectrum, d) charge survey scan, e) charge Mn 2p spectrum, f) charge O 1s spectrum, g) charge Mn 3s spectrum, and h) charge Zn Auger LMM spectrum. 96

Figure S4-1 XPS survey scan for the as deposited Mn₃O₄ sample, showing strong Mn 2p and O 1s peaks, as well as a small Mn 3s peak. 99

Figure S4-2 Room temperature Raman spectra for (a) γ -MnOOH, (b) β -MnO₂, (c) α -Mn₂O₃, and (d) Mn₃O₄ [189]. It should be noted that several factors can influence Raman spectroscopy results including type of laser used, power of the laser, material crystallinity, amount of material, material stress and orientation, and material defects [167], [168]. 99

Figure S4-3 GITT results for the first cycle after conditioning. A 10 min ON period and a 20 min REST period were used. A specific current of 100 mA g⁻¹ was applied during the ON period. The

red circles and line show the calculated diffusion coefficient for Zn^{2+} for different points along the discharge cycle..... 100

(4-1)..... 100

Figure S4-4 SEM EDS spectrum for an uncycled Mn_3O_4 on CP sample that was submerged in ZIB electrolyte (2M $ZnSO_4$ and 0.2M $MnSO_4$) for one week. The arrows on the image indicate where the Zn peaks would be found if they were present in the sample. 101

Figure S4-5 SEM SE images, STEM ADF images, and STEM EDS maps for the 5th cycle after conditioning at different points along discharge and charge: a) discharge point 1 (1.35 V), b) discharge point 2 with the arrow indicating ZSH (1.25 V), c) charge point 1 (1.54 V), and d) charge point 2 (1.63 V). The maps shown in the bottom righthand corner for each potential are overlays of Mn, O, Zn, and S. The inset GCD plots depict the positions along the cycle where the battery was stopped for analysis. 102

Figure S4-6 a) TEM BF image of a ZSH flake and b) selected area diffraction (SAD) pattern obtained from the ZSH flake. The rings are labeled with corresponding Miller indices. The red arrow represents carbon and the blue arrows represent ZSH (CIF 9001719)..... 103

List of Tables

Table 2-1 Comparison of Zn and Li properties.....	9
Table 2-2 Electrolyte system conductivities [18].....	10
Table 2-3 List of cathode materials used for ZIBs and their synthesis method, proposed reaction mechanism, and performance.	34
Table 4-1 Summary of XPS data and comparison with other Mn oxide materials.....	84
Table 4-2 Battery cycling performance comparison between this work and other Mn ₃ O ₄ based ZIBs found in the literature.....	87
Table 4-3 Summary of XPS data collected for as deposited Mn ₃ O ₄ cathode, cathode after the conditioning cycle, and cathode after the 5 th cycle after conditioning	97
Table S4-1 Indexing of diffracted rings from SAD pattern in Figure S4-7b	104

List of Acronyms and Abbreviations

AAS	Atomic Absorption Spectroscopy
BF	Bright Field
BSE	Back Scattered Electron
CFP	Carbon Fiber Paper
CNT	Carbon Nanotube
CP	Carbon Paper
CV	Cyclic Voltammetry
DF	Dark Field
DFT	Density Functional Theory
DMSO	Dimethyl Sulfoxide
EDS	Energy Dispersive Spectroscopy
EELS	Electron Energy Loss Spectroscopy
EIS	Electrochemical Impedance Spectroscopy
GCD	Galvanostatic Charge and Discharge
GITT	Galvanostatic Intermittent Titration Technique
HAADF	High Angle Annular Dark Field
HCF	Hexacyanoferrate
HR-TEM	High Resolution Transmission Electron Microscopy
LIB	Lithium-ion Battery
NIB	Nickel-ion Battery
Ni-MH	Nickel Metal-Hydride
OER	Oxygen Evolution Reaction
ORR	Oxygen Reduction reaction
PEDOT	Polyethylenedioxythiophene
PHES	Pumped Hydroelectric Energy Storage
PTFE	Polytetrafluoroethylene
RS	Raman Spectroscopy
SDS	Sodium Dodecyl Sulfate
SE	Secondary Electron

SEM	Scanning Electron Microscopy
SHE	Standard Hydrogen Electrode
STEM	Scanning Transmission Electron Microscopy
SS	Stainless Steel
sXAS	Soft X-ray Absorption Spectroscopy
TEM	Transmission Electron Microscopy
XPS	X-ray Photoelectron Spectroscopy
XRD	X-ray Diffraction
XRF	X-ray Fluorescence
ZIB	Zinc-ion Battery
ZSH	Zinc Sulfate Hydroxide ($\text{Zn}(\text{OH})_2 \cdot 3\text{ZnSO}_4 \cdot x\text{H}_2\text{O}$)

Chapter 1: Introduction

1.1 Zinc-ion Batteries

Fossil fuels are currently the most widely used energy source in the world and are continuing to grow in consumption in an unsustainable manner [1]. However, with growing concerns of climate change and the limited availability of traditional energy sources, research has shifted to focus on developing new renewable energy sources, such as solar, hydro, and wind. Although there has been significant growth in the generation of renewable energy, these energy sources are intermittent and weather dependent; therefore, storing the energy generated by the numerous renewable sources for later use remains an issue [1]–[3]. Currently, the most common way to store renewable energy for grid applications is pumped hydroelectric energy storage (PHES) [3], although PHES is not without issues. Particularly, the geographical location of PHES is of utmost importance [4]. The lithium-ion battery (LIB) is one of most used energy storage devices for many different applications, ranging from portable electronics to emerging electric vehicles. LIBs are also being used for grid storage applications [5], [6]. However, LIBs face many challenges that limit their future practicality. Concerns regarding the increasing cost of LIB materials, limited availability of Li and other rare earth materials, battery lifetime, and public safety have pushed research towards developing safer and more environmentally friendly energy storage options [1], [3], [7]–[11]. Aqueous rechargeable zinc-ion batteries (ZIBs) are a relatively new technology that have recently garnered much interest in the academic community. This is largely due to Zn being environmentally benign, cheap, abundant, and possessing a high theoretical capacity and energy density [7], [9], [12]. Figure 1-1 compares ZIBs to other energy storage technologies in terms of specific power density and specific energy density. As seen in the figure, ZIBs have the potential to perform just as well as, if not better than, LIBs while also exhibiting specific power densities better than those for LIBs.

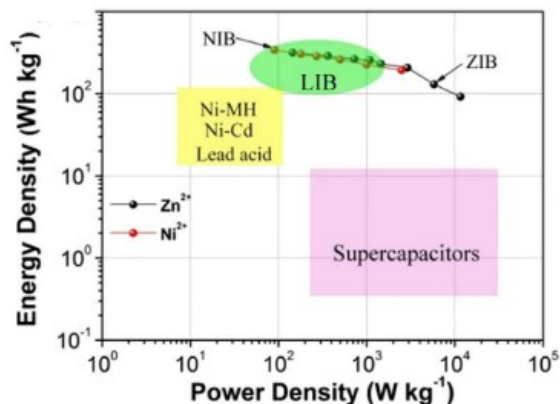


Figure 1-1 Ragone plot comparing performance of ZIBs and other energy storage devices including Ni-ion batteries (NIB), Ni metal-hydride batteries (Ni-MH), and Ni-Cd batteries [13].

Like most batteries, ZIBs consist of four major components: an anode, a cathode, an electrolyte, and a separator. During battery discharge, Zn ions flow from the anode to the cathode through the aqueous electrolyte, while electrons flow from the anode to the cathode through an external circuit. On recharge, the reverse process occurs with Zn ions and electrons flowing back to the anode. This process is depicted in Figure 1-2 with MnO₂ used as the cathode material. The separator (not shown in Figure 1-2) prevents short-circuiting by preventing the electrodes from coming into contact with each other and inhibiting electron transfer through the electrolyte.

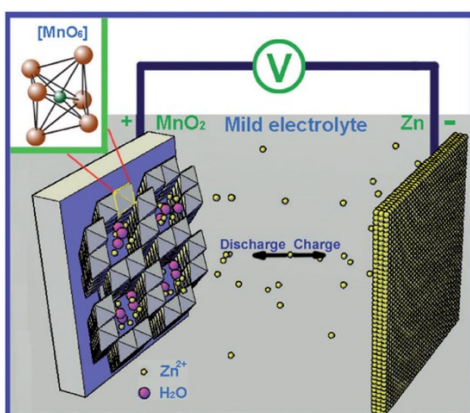


Figure 1-2 Schematic of a ZIB. Zn ions are stripped from the Zn plate and are inserted into the α -MnO₂ electrode on discharge. The reverse occurs on charge. The inset image shows the basic structural unit of α -MnO₂, the MnO₆ octahedron [14].

Presently, the major limiting technology in ZIB development and performance is the cathode material. In general, most cathode materials explored for ZIBs have exhibited poor capacities, poor rate capabilities, poor cycling performance, or a combination of each [7], [8]. Furthermore, there is debate regarding the reaction mechanism(s) that occurs at the cathode on battery charge and discharge, particularly regarding Mn oxide cathode materials [15], [16]. A number of different electrolyte materials have also been explored in an effort to improve the performance of the cathode and battery in general [17]. Efforts to improve the Zn anode have been documented in the literature as well. However, improving the performance of the cathode material and understanding the battery reaction mechanisms during charge and discharge are key in developing sustainable and economically viable ZIBs.

1.2 Thesis Content

This thesis consists of five chapters, with the first chapter being an introduction to this document. The second chapter discusses the literature regarding ZIBs, specifically focusing on the cathode materials used and the proposed reaction mechanisms for those cathodes. Focus is given to Mn oxide materials. Different synthesis methods, material and electrochemical characterization techniques, and previous work conducted within the Ivey research group regarding the electrodeposition of Mn are also discussed in the second chapter. It should be noted that this work is exploratory in nature as ZIBs have not been previously studied by the Ivey research group and are a relatively new area of research in the literature.

The main objective of this work is to utilize electrodeposition techniques previously developed by the Ivey research group to fabricate cathode materials for use in ZIBs as a proof of concept. The third chapter focuses on two different Mn oxide electrodeposition techniques previously developed by the Ivey research group. The first technique is a direct anodic electrodeposition and the second technique is a pulsed anodic electrodeposition. These two techniques were adopted to fabricate cathode materials for use in ZIBs. Only initial materials and electrochemical characterization and performance behavior of the two different types of deposits are presented, since these approaches were not pursued.

The second objective of this work is to produce a high performing cathode material for ZIBs. The fourth chapter focuses on the development of a high performing Mn oxide cathode material used for ZIBs. The pulsed anodic electrodeposition explored in chapter three was employed again for this study. The deposited material is initially characterized using various materials characterization techniques. The cathode is then used in ZIBs and subjected to various electrochemical tests to characterize performance. Using the materials and electrochemical data, further insight is gained into the reaction mechanism for the cathode material. However, further analysis is required to determine the exact mechanism occurring during charge and discharge.

The fifth chapter concludes the thesis and includes recommendations for future work in the area of cathode materials for ZIBs.

Chapter 2: Literature Review

2.1 Battery Capacity and Current

Capacity is the measure of the total amount of electric charge stored in a battery. Typically, capacity is measured in units of milliampere-hours (mAh). The units of mAh describe a battery that can provide the labelled current on discharge for 1 h, after which the battery will be completely discharged at the specified nominal voltage. Specific capacity is the capacity of the battery measured per gram of active material (mAh g^{-1}). The active material is the material that participates in the electrochemical reaction [18]. For example, if Mn oxide is the active material for a cathode, the mass of the active material is only that of Mn oxide and does not include the mass of the current collector or any other additives used for the cathode. The theoretical specific capacity of the active material can be calculated using Equation (2-1) [19]:

$$\text{Theoretical Specific Capacity } \left(\frac{\text{mAh}}{\text{g}} \right) = \frac{n * F}{3.6 * MW} \quad (2-1)$$

where n is the number of electrons transferred (or the valence change), F is Faraday's constant ($96,485 \text{ C mol}^{-1}$), 3.6 is the conversion factor between coulombs (C) and mAh, and MW is the molecular weight of the active electrode material (g mol^{-1}). To convert the capacity to a volume basis, the density of the electrode material is required. Discharge and charge current are measured in milliamperes (mA). Current density is measured in milliamperes per unit area (mA area^{-1}), typically cm^2 . Specific current is the current per gram of active material and is measured using units of milliamperes per gram (mA g^{-1}). Specific current is also frequently referred to as current density in the literature.

Another common designation used to describe the applied charge or discharge current is C-rate. The C-rate for a battery is represented as C/R , where R is the number of hours until the battery has completely discharged its nominal capacity [20]. 1C is commonly taken as the nominal capacity of the electrode that is being tested. The nominal capacity can be defined as the theoretical capacity of the electrode, the maximum capacity that was measured, or an arbitrary value assigned

by the researcher. The rate of discharge will affect the electrical capacity of the battery; as the discharge current increases, the effective capacity of the battery decreases [20]. C-rates are also used when describing applied current densities and specific currents.

2.2 Battery Reaction Mechanisms

Zinc-ion batteries (ZIBs) are typically described as intercalation type batteries, similar to lithium-ion batteries (LIBs) that currently dominate the market in mobile devices, electric vehicles, and energy storage [7]–[9]. However, some groups have argued that some ZIBs may operate under a conversion type mechanism, rather than intercalation [21], [22].

2.2.1 Intercalation Reactions

Intercalation is one type of electrochemical reaction that can occur in batteries. Intercalation involves the reversible insertion and extraction of metallic ions from a host material. The metallic ions are inserted into interstitial sites within the host material, without altering the host material structure [20] [23]. However, the insertion of the metallic ions can result in a change in the host material volume. The repeated change in material volume can lead to structural damage over time, resulting in decreased battery performance. Equation (2-2) describes the general reaction for the intercalation process [20]:



where A is the species that is being intercalated, B is a transition metal, and X is an anion. Upon insertion of the guest ion, the valence of the host metal is reduced to accommodate the charge of the inserted guest ion; hence, the extensive use of transition metals that can achieve multiple valence states. Figure 2-1 depicts an intercalation reaction occurring in the cathode of a LIB during discharge and charge.

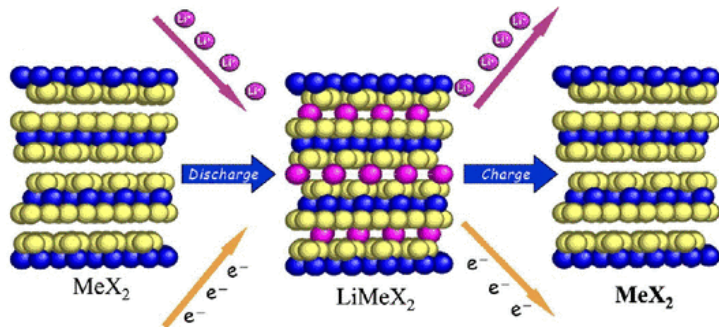


Figure 2-1 Depiction of an intercalation reaction for a LIB occurring in the cathode material on charge and discharge [24].

2.2.2 Conversion Reactions

Conversion reactions, or reconstitution reactions, are another type of electrochemical reaction that can occur in batteries. Conversion reactions involve the breaking and forming of bonds and may include the displacement of one species by another [20]. The repeated structural change can also lead to structural damage, similar to that observed in intercalation reactions. Equation (2-3) and (2-4) represent general conversion reactions that may occur in a battery [20]:

$$A + B = AB \tag{2-3}$$

$$A + BX = AX + B \tag{2-4}$$

where A is the anode material and B and BX are the cathode material. Figure 2-2 depicts a conversion reaction occurring in the cathode of a LIB on discharge and charge.

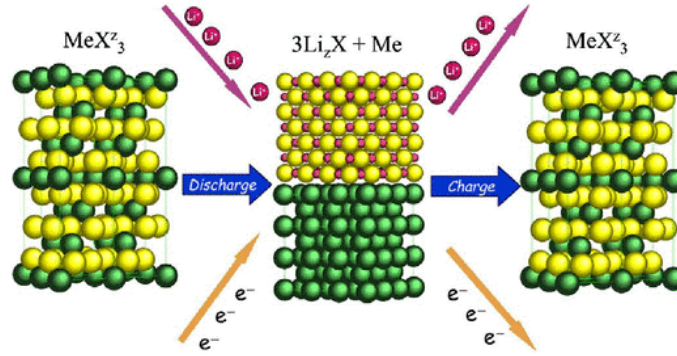


Figure 2-2 Depiction of a conversion reaction for a LIB occurring in the cathode material on charge and discharge [24].

2.2.3 Efficiency

The efficiency of a battery can be measured in a variety of ways. Coulombic efficiency, voltaic efficiency, and round trip efficiency are the most commonly used methods. Coulombic efficiency is often used to determine the reversibility of a battery or the charge efficiency. Coulombic efficiency is the ratio of the capacity achieved on discharge to the capacity achieved on the prior charge over one whole cycle [25]. A large Coulombic efficiency is indicative of a highly reversible reaction mechanism in the battery. Voltaic efficiency is determined as the ratio of the average discharge voltage over the charge voltage. For batteries, the charge voltage is always higher than the discharge voltage, resulting in voltage efficiencies less than 100%. The closer the charging voltage is to the discharge voltage, the better the voltaic efficiency of the battery. LIBs have a voltaic efficiency of 80-90%. This is based on nominal discharge potentials between 3.6 and 3.85 V and charge potentials between 4.0 and 4.4 V [26]. The voltaic efficiency of ZIBs can range from less than 50% and reach up to 85%, depending on the cathode material used. Round trip efficiency for an energy storage device is the ratio between the energy recovered on discharge (Wh) to the energy input on charge (Wh) [27].

2.3 Materials Used in Zinc-ion Batteries

Various materials have been explored for ZIBs, with a focus on cathode materials to improve battery performance and durability. In general, porous structures and nanomaterials are

better suited for electrode use because of their high surface area and short diffusion lengths, allowing for better reaction kinetics [18]. Several different electrolyte materials with varying concentrations have also been researched to improve battery performance and durability, but not as extensively as the cathode materials.

2.3.1 Anode Material

Metallic Zn is the major material used for ZIB anodes due to its stability in aqueous environments, high abundance, non-toxicity, low potential versus the standard hydrogen electrode (SHE) (-0.76 V), and environmentally benign behaviour [28]. Furthermore, for every Zn ion that is produced, two electrons are produced, compared with a single electron for Li. Zn also possesses a high theoretical capacity and atomic and ionic radii similar to those for Li. Table 2-1 compares the potential, theoretical capacities, and atomic and ionic radii for Zn and Li.

Table 2-1 Comparison of Zn and Li properties.

Element	Potential vs SHE (V)	Specific Capacity (mAh g ⁻¹)	Volumetric Capacity (mAh cm ⁻³)	Atomic Radius (Å) [29]	Ionic Radius (Å) [29]	Hydrated Ionic Radius (Å) [16]
Zn/Zn ²⁺	-0.76	820	5854	1.53	0.74	4.04-4.30
Li/Li ⁺	-3.05	3829	2044	2.05	0.76	3.40-3.82

During battery operation, Zn is stripped and plated during discharge and charge, respectively. Equation (2-5) describes the behaviour of Zn at the anode on charge and discharge.



While possessing many benefits, divalent Zn ions also present a challenge for batteries because of their stronger steric and electrostatic interactions with the cathode material and electrolyte, compared with monovalent ions such as Li⁺ and Na⁺ [30]. Additionally, the solvated

Zn ion is larger compared with the solvated Li ion, which will cause difficulty regarding intercalation. Initially, the Zn metal anode displayed poor reversibility and Coulombic efficiency. However, these issues have mostly been addressed by optimizing the electrolyte used in ZIBs and are discussed in the following section. Although metallic Zn foil is the most commonly used Zn anode, coating metallic Zn onto various C-based substrates to improve Zn anode performance and durability has been considered [31].

2.3.2 Electrolyte Materials

There are several different classes of electrolyte materials for use in batteries. Currently, LIBs are dominated by the use of organic electrolytes. However, organic electrolytes can be toxic, expensive, and explosive if not handled correctly [7], [9], [32], [33]. Both organic and ionic-liquid electrolytes have been used for some ZIB systems, but have generally resulted in poor performance and are expensive [34]–[36]. Aqueous electrolytes are the most common electrolytes used for ZIBs. Aqueous electrolytes are relatively cheap, environmentally benign, provide high ionic conductivities, and are not flammable [7], [9]. Table 2-2 compares the conductivities of aqueous electrolytes with other electrolyte classes.

Table 2-2 Electrolyte system conductivities [18]

Electrolyte System	Conductivity ($\Omega^{-1}\text{cm}^{-1}$)
Aqueous electrolytes	$1-5 \times 10^{-1}$
Molten salts	$\sim 10^{-1}$
Inorganic electrolytes	$2 \times 10^{-2}-10^{-1}$
Organic electrolytes	$10^{-3}-10^{-2}$
Polymer electrolytes	$10^{-7}-10^{-3}$
Inorganic solid electrolytes	$10^{-8}-10^{-5}$

Aqueous electrolytes also help mitigate the steric and electrostatic effects of Zn^{2+} ions by partially shielding their charge, allowing easier Zn ion movement in the electrolyte and reduced interactions with cathode materials [30], [37]. Conversely, the use of aqueous electrolytes presents some challenges, particularly the potential generation of H_2 and O_2 during battery operation. This limits battery operation to within a specific narrow potential window, which is dependent on the electrode materials, electrolyte concentrations, and electrolyte pH [9], [38]. Additionally, using aqueous electrolytes may result in side reactions, co-intercalation of other ions, and dissolution of electrode materials [7], [21], [39]–[42].

There are three main aqueous electrolyte materials that have been used in the development of ZIBs: KOH, ZnSO_4 , and $\text{Zn}(\text{CF}_3\text{SO}_3)_2$. KOH is a common electrolyte, which is found in primary Zn/MnO₂ alkaline batteries used today. However, using KOH electrolyte in ZIBs produces irreversible by-products and Zn dendrites on the anode, resulting in poor Coulombic efficiency and rapid capacity degradation [40], [43], [44]. This phenomenon is similar to that observed in primary alkaline batteries. The most common electrolyte for ZIBs is ZnSO_4 , with concentrations varying between 1 M and 3 M with a pH value between 4 and 6 [14], [21], [28], [30], [38]–[50]. ZnSO_4 is relatively cheap and environmentally benign, making it an excellent electrolyte option. Compared with KOH, ZnSO_4 provides much improved cyclability and higher battery capacity [40]. If relatively low concentrations of ZnSO_4 are used and the pH is weakly acidic, the formation of Zn dendrites and precipitates can be completely avoided [38], [43], [44]. ZnSO_4 also allows for a wide electrochemical window, thus suppressing H_2 and O_2 evolution. However, Zhang et al. found that ZnSO_4 caused cracks to form in the Zn anode on repeated plating and stripping [40]. $\text{Zn}(\text{CF}_3\text{SO}_3)_2$ is another aqueous electrolyte with growing interest as a viable electrolyte option. Compared with ZnSO_4 , $\text{Zn}(\text{CF}_3\text{SO}_3)_2$ provides better cycling of the Zn anode; no cracks were observed on the anode after repeated plating and stripping [40]. Zhang et al. attributed the improved behaviour of $\text{Zn}(\text{CF}_3\text{SO}_3)_2$ to a reduction in the solvation effect on Zn ions and higher conductivities and reaction kinetics compared with ZnSO_4 [33], [40]. Like ZnSO_4 , $\text{Zn}(\text{CF}_3\text{SO}_3)_2$ also possesses a wide electrochemical window, which effectively suppresses H_2 and O_2 evolution in the battery [33]. Still, $\text{Zn}(\text{CF}_3\text{SO}_3)_2$ is not widely used as it is almost 60 times more expensive than ZnSO_4 [51], [52]. For both ZnSO_4 and $\text{Zn}(\text{CF}_3\text{SO}_3)_2$, it was observed that increasing the concentration of the electrolyte increased the Coulombic efficiency due to reduced water activity, water side reactions, and altered cation/anion solvation and transport [31]. Several other aqueous

electrolytes including ZnCl_2 , $\text{Zn}(\text{ClO}_4)_2$ and $\text{Zn}(\text{NO}_3)_2$ have also been used for ZIBs, but resulted in poor performance for various reasons, such as electrode degradation [16], [31].

2.3.3 Cathode Materials

The cathode is currently the limiting technology in ZIBs. Materials used for cathodes in ZIBs must exhibit a large storage capacity, stability in the electrolyte environment, and long-term cyclability without significant loss in capacity. Materials used as cathodes in ZIBs can be grouped into four main categories: Mn oxide materials, hexacyanoferrates (HCF), V oxide materials, and others. Several different materials make up the category of others. While the majority of cathode materials are classified as intercalation type, there is some debate whether some materials are conversion type or a combination of conversion and intercalation. Table 2-3 and Figure 2-15 provide a list and depiction of all the different types of cathode materials used for ZIBs and their performance.

2.3.3.1 Manganese Oxides

Manganese oxide materials are one of the most studied materials for cathode use in ZIBs [12]–[15], [21], [22], [28], [30], [32], [33], [39]–[42], [45], [47], [53]–[59]. Manganese oxide is cheap, environmentally benign, and possesses a high theoretical capacity of 308 mAh g^{-1} [14], [41], [59]. Furthermore, Mn has several different stable valence states and crystal structures. These structures are large and open, which allow for easy access to the bulk material for intercalation to occur [60]. These oxides are made up of MnO_6 octahedra and can form several 1D, 2D, and 3D structures [57], [61]. Of the numerous Mn oxide materials available, MnO_2 is the most studied for use as the cathode in ZIBs [13], [14], [21], [22], [28], [30], [39], [40], [45], [47], [53]–[59]. Figure 2-3 depicts several stable MnO_2 crystal structures utilized for ZIBs. Of the different MnO_2 phases that have been investigated (α , β , δ , ϵ , γ , λ , R), α - MnO_2 is the most widely studied due to its large 2×2 tunnel structure [13], [14], [21], [22], [28], [40], [45], [53], [56]–[58]. Other Mn oxide materials that have been used as cathode materials for ZIBs include Mn_2O_3 , Mn_3O_4 , ZnMn_2O_4 , and MgMn_2O_4 , [32], [33], [41], [42], [62]. Several studies have also combined Mn oxides with

other Mn oxide materials, polymers, and other materials to produce high performance cathodes [63]–[66].

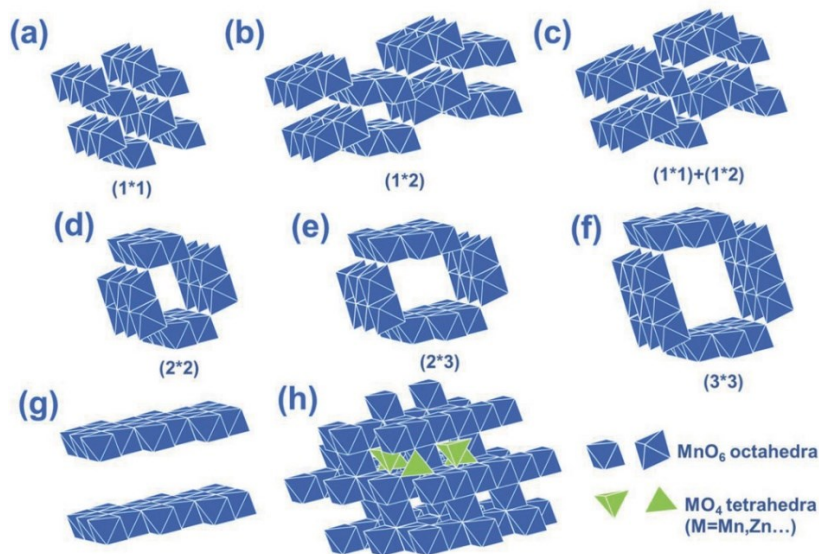


Figure 2-3 Crystal structures of Mn oxide materials and their corresponding tunnel size if available. a) β - MnO_2 (pyrolusite-type), b) R - MnO_2 (ramsdellite-type), c) γ - MnO_2 (nsutite-type), d) α - MnO_2 (hollandite-type), e) romanechite-type MnO_2 , f) todorokite-type MnO_2 , g) δ - MnO_2 (birnessite-type), h) λ - MnO_2 (spinel-type) [16].

When initially used as a cathode for ZIBs, Mn oxide materials showed poor cyclability and significant capacity fading with increasing current densities [14], [42], [45], [56]. The poor cycling and capacity fading were attributed to a phase change in the Mn oxide structure during cycling and the repeated ion insertion and extraction, causing irreversible damage due to increasing internal stress [21], [40], [41], [54]. Several groups have observed that on repeated cycling, the cathode material will revert back to its original phase once the battery is recharged [28], [45], [55], [56]. However, other groups have reported that after several charge and discharge cycles the cathode material does not revert back to its original starting phase [40], [42], [67], [68]. Upon discharge, Mn oxide cathodes have been reported to transform into a wide variety of different structures. Several layered and spinel structures that have been reported to form, such as Zn-birnessite, Zn-buserite, and ZnMn_2O_4 [14], [21], [40], [41], [45], [55], [56], [58]. Both Zn-birnessite and Zn-buserite have similar structures, with Zn-buserite containing extra layers of water between the Mn

oxide layers compared with Zn-birnessite [69], [70]. Lee et al. believe that the Zn-birnessite structure after battery cycling is actually Zn-buserite that has undergone a phase transformation with the loss of water molecules [45]. There is no confirmed chemical formula for Zn-buserite; however, it is considered to be similar to that for Ca-buserite [40], [54]. Other groups have reported that the original cathode material will transform to Mn_3O_4 , Mn_2O_3 , $MnOOH$ and other compounds as well [67], [71]. Regardless, whether the active material reverts back to its original structure or not, the phase change of Mn oxide during battery cycling causes irreversible damage leading to a short cathode life span and rapid loss in performance [33], [40], [45], [54]. Figure 2-4 depicts all the different transformations of Mn oxide during cycling that have been reported/suggested in the literature.

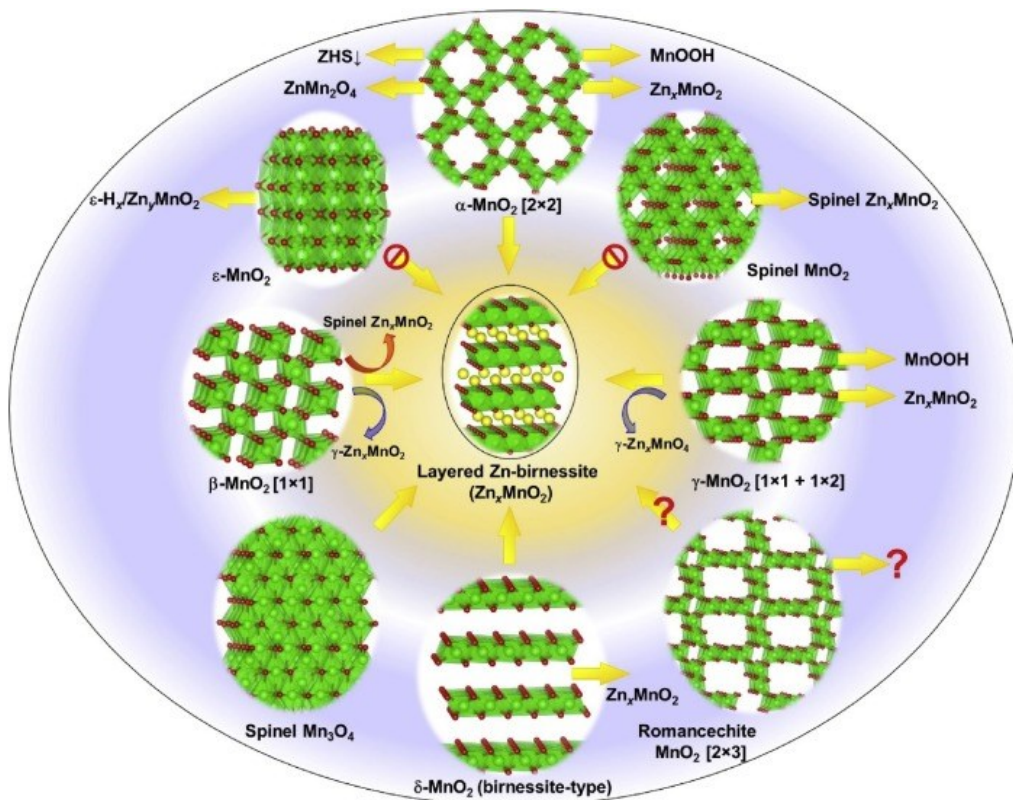


Figure 2-4 Summary of the phase transformations of most Mn oxide materials [2]. The green octahedra are MnO_6 and the red and yellow dots represent O and Zn atoms, respectively. Yellow arrows indicate the new phase upon transformation, with many materials transforming into layered Zn-birnessite. Blue and red arrows indicate other simultaneous phase transformations. Question marks indicate that the phase transformation is unknown. The prohibition sign indicates that the shown transformation does not occur.

Poor performance was also attributed to Mn dissolution upon battery discharge [21], [40], [41], [54]. Manganese dissolution is a result of the change in Mn oxidation state upon Zn intercalation. When unstable Mn^{3+} is produced in the Mn oxide structure, it will further disproportionate into Mn^{4+} and Mn^{2+} [21], [28], [40], [45]. Mn^{2+} then dissolves into the electrolyte, further degrading the cathode and decreasing electrochemical performance. This type of dissolution is caused by Jahn-Teller distortion on the formation of Mn^{3+} [2], [31]. Manganese dissolution from the cathode has been reported to be suppressed by the addition of $MnSO_4$ or $Mn(CF_3SO_3)_2$ into the electrolyte. The addition of $MnSO_4$ or $Mn(CF_3SO_3)_2$ shifts the equilibrium concentration of Mn^{2+} to help prevent or reduce the dissolution of Mn into the electrolyte [21], [22], [32], [40], [41]. Protective coatings such as polyethylenedioxythiophene (PEDOT) have also been used to help improve cyclability and prevent dissolution [65], [72]. Additionally, Mn oxide materials are inherently poor ionic and electronic conductors, which also hinders their performance as battery cathodes [28], [41], [47]. To counteract the inherently poor conductivity of Mn oxide materials, many groups will combine Mn oxide with conductive additives, such as carbon, to improve performance [47], [72]–[75]. Additionally, reducing the thickness of the active material can also improve conductivity by shortening the distance electrons need to travel.

In addition to being the most studied cathode material for ZIBs, Mn oxide materials are also the most complex and widely debated regarding the reaction mechanism during battery cycling. The following reaction mechanisms, while focused primarily on MnO_2 based materials, are representative of all reported reaction mechanisms for other Mn oxide materials as well. The type of reaction mechanisms proposed for all the different Mn oxide materials studied are listed in Table 2-3. Generally, Mn oxide cathode materials are categorized as intercalation type batteries. Equations (2-6) and (2-7) describe a general Zn^{2+} intercalation reaction that can occur in ZIBs using MnO_2 cathodes [14], [53].



Initially, it was believed that Mn oxide would intercalate only Zn ions into its structure. Many groups observed only a single plateau during galvanostatic charge and discharge (GCD) testing or a single pair of reduction and oxidation (redox) peaks during cyclic voltammetry (CV) testing (Figure 2-5a) [14], [47], [57], [58]. The single pair of peaks in the CV results and the single plateau in the GCD testing correspond to the insertion and removal of Zn^{2+} from the active electrode material. Other groups observed two plateaus during GCD testing and two pairs of redox peaks in CV testing (Figure 2-5b) [28], [33], [40], [41], [53], [55]. The two pairs of peaks and plateaus were attributed to the insertion and removal of Zn^{2+} into multiple sites, with some sites requiring more energy for insertion than other sites.

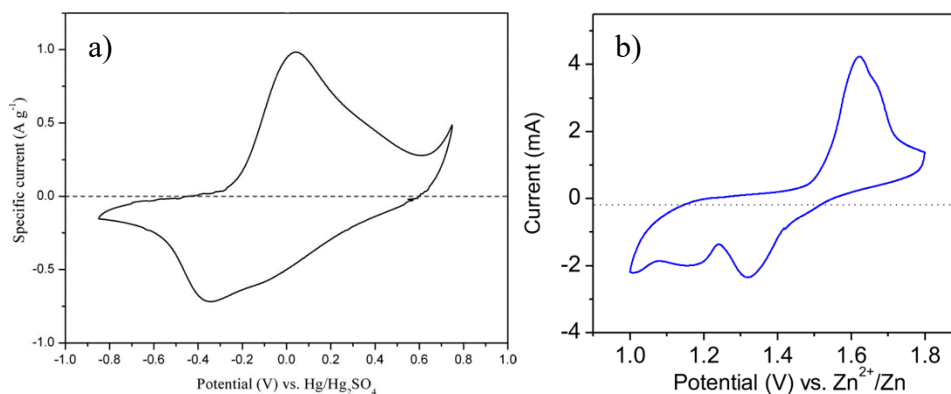


Figure 2-5 CV curves for two different MnO_2 cathode battery systems that claim Zn^{2+} intercalation reaction mechanisms. a) A single pair of redox peaks indicating Zn intercalation into one type of MnO_2 site using 0.1 M $\text{Zn}(\text{NO}_3)_2$ electrolyte [57], b) Two pairs of redox peaks indicating Zn intercalation into two different MnO_2 sites using 1 M ZnSO_4 electrolyte [28].

Conversely, Sun et al. and Hao et al. have suggested that MnO_2 cathodes may intercalate both H^+ and Zn^{2+} during battery discharge and undergo co-intercalation [39], [42]. Sun et al. showed that both H^+ and Zn^{2+} intercalated into $\epsilon\text{-MnO}_2$ by testing the battery with two different electrolytes; one containing only MnSO_4 and the other containing both MnSO_4 and ZnSO_4 [39]. The charge and discharge test results are presented in Figure 2-6. The MnSO_4 electrolyte produced only one voltage plateau (Figure 2-6b). With the addition of ZnSO_4 , two voltage plateaus and an

increase in capacity were recorded during discharge testing (Figure 2-6b). The first plateau was accredited to H^+ insertion, with the second plateau ascribed to Zn^{2+} insertion.

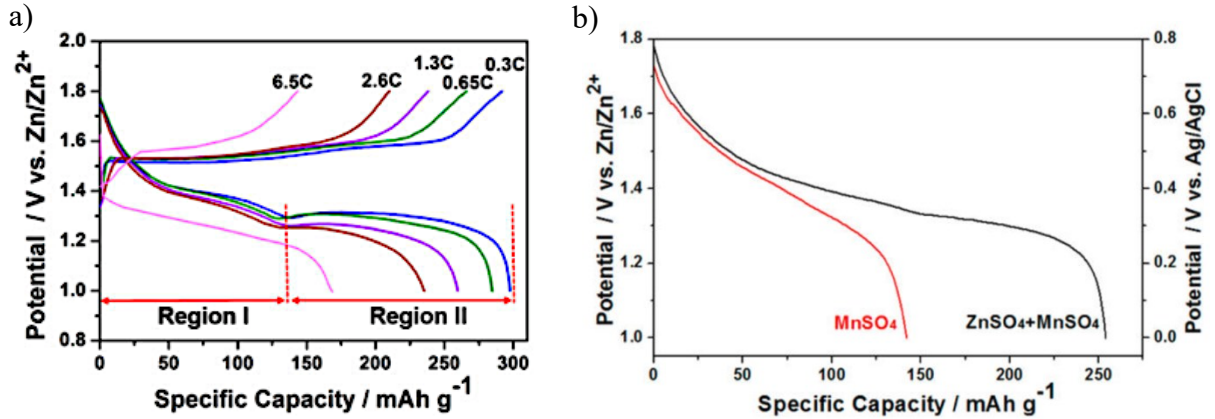
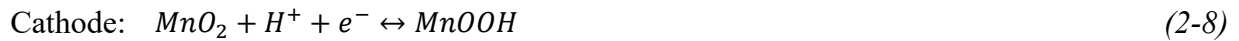


Figure 2-6 Charge and discharge curves for different ZIBs. a) MnO_2 on carbon fiber paper in $2M ZnSO_4 + 0.2M MnSO_4$ electrolyte [39], b) Discharge curves of MnO_2 in $MnSO_4$ solution with and without $ZnSO_4$ [39]. Two plateaus are observed for the electrolyte containing both $MnSO_4$ and $ZnSO_4$, while only one plateau is observed for the electrolyte containing only $MnSO_4$.

Using ex-situ X-ray diffraction (XRD) measurements, Sun et al. reported the appearance of $MnOOH$ peaks, followed by the formation of $ZnMn_2O_4$ peaks [39]. The sequential appearance of the peaks suggests that H^+ intercalation is followed by Zn^{2+} intercalation in the cathode. Hao et al. and Sun et al. both reported two pairs of redox peaks during CV testing, which they attributed to the insertion and removal of both H^+ and Zn^{2+} [39], [42]. The CV curve obtained by Hao et al. is shown in Figure 2-7. The pair of redox peaks also correspond to the pair of plateaus observed in the charge and discharge tests. Equations (2-8) through (2-10) describe a general co-intercalation reaction mechanism that may occur in ZIBs [39].



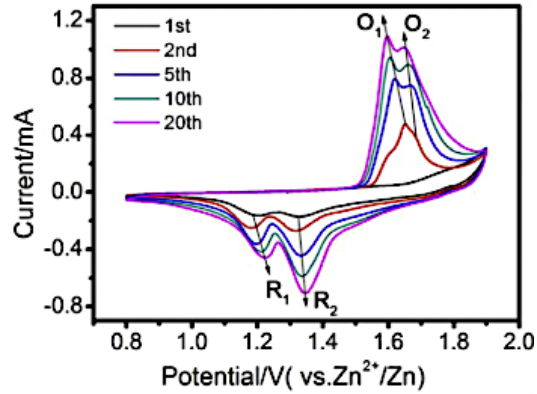
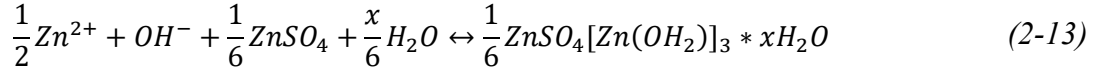


Figure 2-7 Cyclic voltammetry curve for Mn_3O_4 in $2M ZnSO_4$ [42]. R_1 and O_1 indicate the insertion and removal of Zn^{2+} , respectively. R_2 and O_2 indicate the insertion and removal of H^+ , respectively.

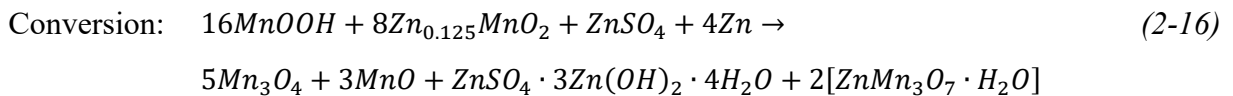
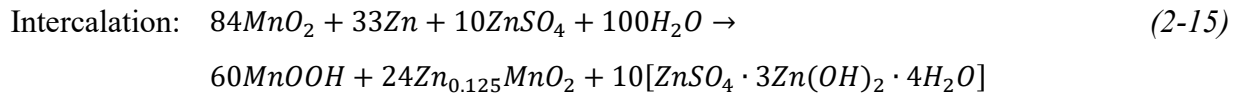
Although usually characterized as intercalation type cathodes, there has been some debate whether Mn oxide materials are actually conversion type, or a combination of both intercalation and conversion. Lee et al. reported a localized pH increase at a MnO_2 during discharge, resulting in a zinc sulfate hydroxide (ZSH, $Zn_4(OH)_6(SO_4) \cdot 5H_2O$) precipitate forming on the cathode, rather than Zn intercalation into a α - MnO_2 structure [22]. The increase in pH was accredited to the dissolution of α - MnO_2 during discharge. Furthermore, on recharge, the localized pH became acidic and the precipitates dissolved back into the electrolyte. Pan et al. also reported the formation of precipitates and did not observe any evidence of Zn^{2+} intercalation in the material. Using high resolution transmission electron microscopy (HR-TEM) analysis, they reported the formation of $MnOOH$ on discharge, indicating a reaction between MnO_2 and H^+ [21]. In addition, it is suggested that OH^- reacted with $ZnSO_4$ and H_2O from the electrolyte to form a ZSH, similar to the precipitate reported by Lee et al. On recharge, Pan et al. reported that the lattice distance and crystallinity of the electrode reverted to its original structure. Equations (2-11) through (2-14) describe general conversion reactions that can occur at the Mn oxide cathode and Zn anode [21], [22].





As mentioned previously, Hao et al. described a Zn^{2+} and H^{+} intercalation mechanism for the cathode material. However, the formation of $MnOOH$ and ZSH due to a change in pH during discharge was also reported by them [42]. This battery was characterized as an intercalation type even though conversion reactions occurred during discharge and charge.

Recently, Huang et al. and Li et al. have both proposed a new reaction mechanism for ZIBs that involves both conversion and intercalation [67], [71]. Li et al. propose that both Zn^{2+} and H^{+} intercalation occur simultaneously during the first discharge plateau, with Zn^{2+} and H^{+} conversion reactions taking place during the second plateau for MnO_2 cathodes [71]. Through a combination of XRD, X-ray fluorescence (XRF), soft X-ray absorption spectroscopy (sXAS) and scanning electron microscopy (SEM) imaging, $MnOOH$ and Zn_xMnO_2 were reported to form due to H^{+} and Zn^{2+} intercalation, respectively, during the first discharge plateau. During the second discharge plateau, Li et al. reported the formation of Mn_3O_4 , MnO and $ZnMn_3O_7 \cdot mH_2O$ through a series of conversion reactions. Furthermore, ZSH flakes form primarily during the second discharge plateau; however, a small amount also forms during the first discharge plateau. Equations (2-15) and (2-16) summarize the mechanism proposed by Li et al [71]. The chemical reactions presented were determined using density functional theory (DFT) and only represent the discharge portion of the cycle. Figure 2-8 depicts the proposed reaction process.



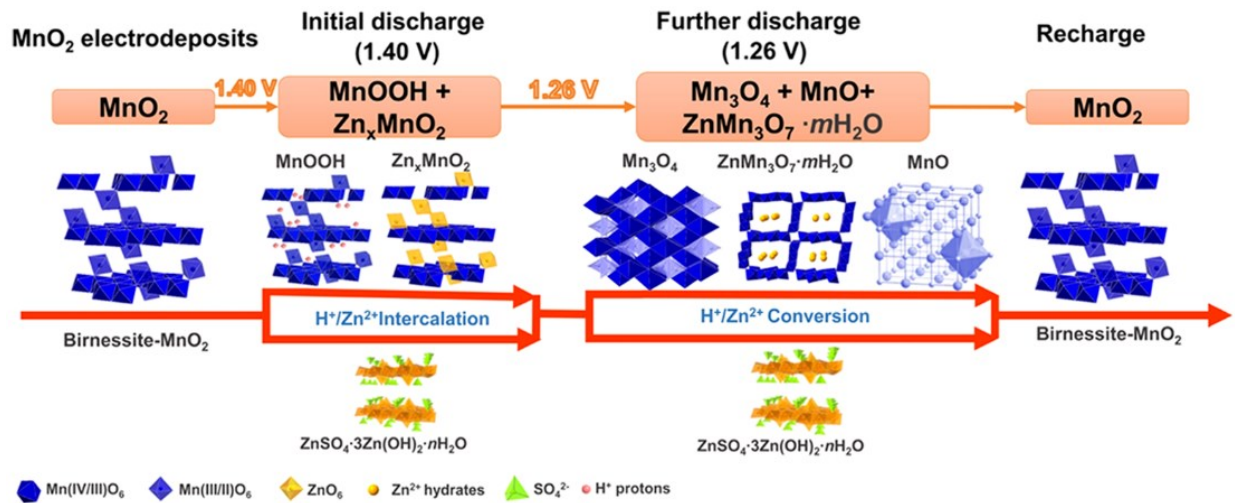


Figure 2-8 Depiction of the intercalation and conversion discharge reaction mechanism proposed by Li et al. [71].
The reverse occurs on the charge.

Interestingly, Li et al. also noticed that higher current densities resulted in fewer ZSH flakes forming and that they were smaller in size when compared with lower current densities [71]. Furthermore, by discharging the ZIB to 1.3 V (the potential before the second plateau begins), the formation of ZSH and the proposed conversion reaction are suppressed [71]. However, by reducing the discharge voltage, the initial battery capacity was significantly reduced as well. Both increasing the applied current and reducing the discharge voltage resulted in a drastic increase in cyclability performance of the battery. Figure 2-9 shows the effects of reducing the discharge potential and increasing the applied current on ZIB cyclability.

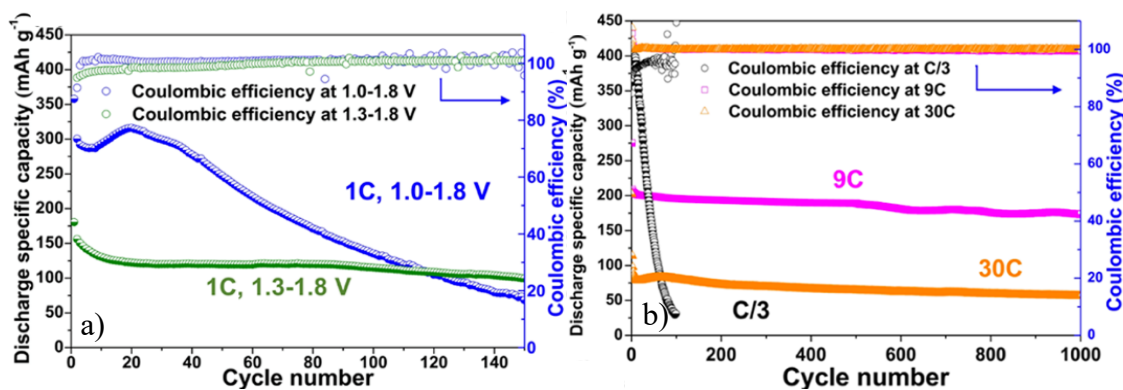


Figure 2-9 Cyclability of ZIBs under different conditions [71]. a) Comparison of cyclability of ZIBs with the discharge potential limit of one battery changed to 1.3V, b) Cycling results for ZIBs under different applied current densities.

Huang et al. also proposed a combination conversion and intercalation mechanism. However, a different reaction for the first cycle compared with the subsequent cycles was suggested. This is due to the different shape of the GCD curve for the first cycle versus subsequent cycles, as shown in Figure 2-10.

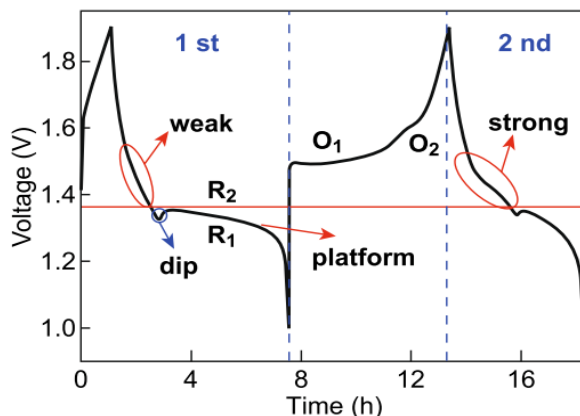


Figure 2-10 GCD curves for the first two cycles [67]. R and O represent reduction and oxidation reactions, respectively. R2 and O2 indicate where the intercalation mechanism occurs. R1 and O1 indicate where the conversion mechanism occurs. R2 occurs above 1.4 V and R1 occurs below 1.4 V. The first cycle shows a weak R2 plateau above the red line, while the second cycle shows a much stronger R2 plateau. The battery consisted of a MnO_2 cathode, Zn anode, and 2M $\text{ZnSO}_4 + 0.5\text{M MnSO}_4$ electrolyte.

Using XRD and HR-TEM analysis, Huang et al. reported that during the first discharge plateau of the first cycle Zn^{2+} intercalates into $\alpha\text{-MnO}_2$, resulting in the formation of $\text{Zn}_x\text{Mn}_2\text{O}_4$ [67]. During the second discharge plateau, both H^+ intercalation and conversion occur, resulting in the formation of MnOOH and Mn_2O_3 [67]. ZSH is also formed during the second discharge plateau. On charge, $\text{Zn}_x\text{Mn}_2\text{O}_4$, MnOOH , and Mn_2O_3 revert back to $\alpha\text{-MnO}_2$. However, ZSH reacts with Mn^{2+} in the electrolyte to form ZnMn_3O_7 . Huang et al. state that the formation of ZnMn_3O_7 on the first charge is responsible for the difference in shape between the first GCD cycle and subsequent cycles [67]. Other groups have also noted the different shape of the first discharge cycle versus the subsequent cycles and many explanations have been suggested for the difference. These include: the cathode going through an activation process, a phase change in the material, the extraction of K^+ ions present in the structure, or a change in morphology [21], [45], [55]. During subsequent cycles, Zn^{2+} is reported to intercalate within $\alpha\text{-MnO}_2$, gradually transforming irreversibly into ZnMn_2O_4 . Additionally, ZnMn_2O_4 will undergo a conversion reaction via Zn^{2+} and Mn^{2+} in solution to produce ZSH [67]. The reaction mechanism proposed by Huang et al. is depicted in Figure 2-11.

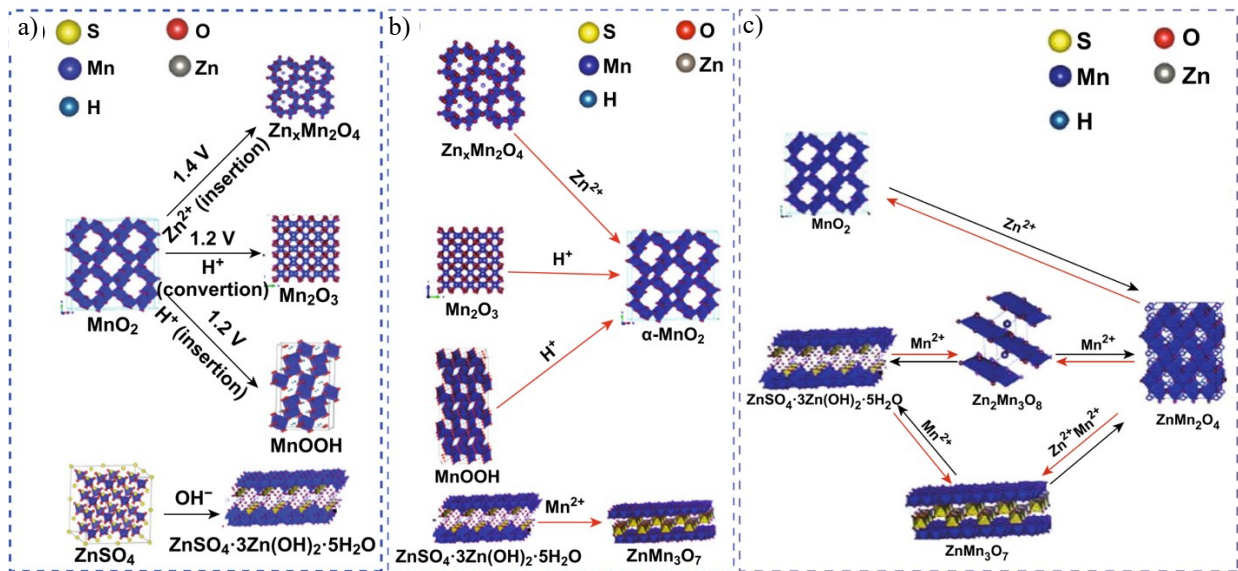


Figure 2-11 The proposed insertion and conversion reaction mechanism by Huang et al. for MnO_2 cathode based ZIBs [67]. a) First cycle discharge; b) first cycle charge; c) subsequent charge and discharge cycles.

Overall, the reaction mechanisms for Mn oxide cathode materials are very complex and not completely understood. For example, α -MnO₂ materials alone have been described to undergo four different reaction mechanisms: Zn²⁺ intercalation, Zn²⁺ and H⁺ intercalation, conversion and a combination of intercalation and conversion [14], [21], [67], [75]. Further testing and analysis are required to resolve the mechanisms for the many different Mn oxide structures. The proposed reaction mechanism for other Mn oxide-based cathode materials can be found in Table 2-3.

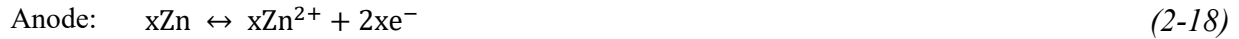
In general, ZIBs using Mn oxide as a cathode have an average operating voltage between 1.2 V and 1.4 V. The minimum discharge and maximum charge voltages are generally around 1.0 and 1.9 V, respectively. Batteries are tested within this voltage window to avoid side reactions with the water in the electrolytes. Several notable ZIBs that use Mn oxide cathodes were able to achieve very good electrochemical performance. Sun et al. produced a battery that was able to retain 99.7% capacity after 10,000 cycles at a high specific discharge current of 1.89 A g⁻¹ [39]. They also achieved a maximum capacity of 290 mAh g⁻¹, which is close to the theoretical value of MnO₂ based on the intercalation of 0.5 mol of Zn²⁺. Zhang et al.'s battery was cycled 2000 times while retaining 94% capacity at a discharge rate of 6.5 C [40]. They used a β -MnO₂ cathode material, which is generally considered to be a poor cathode material compared with other Mn oxide phases. Zhang et al. also achieved similar results when using α -MnO₂ and γ -MnO₂. Pan et al. produced a cathode for ZIBs that was able to retain 92% capacity after 5000 cycles and maintain a capacity of 85 mAh g⁻¹ [21]. This was achieved at a high specific discharge current of 1.54 A g⁻¹. Information regarding the performance of other ZIBs using Mn oxide cathodes can be found in Table 2-3.

2.3.3.2 Hexacyanoferrates

HCF materials are an analogue of Prussian blue and are cheap, nontoxic, and relatively easy to produce [76]. These materials are classified as intercalation type cathodes and have a face centered cubic (FCC) structure. HCF materials have a general formula of MFe(CN)₆, where M is a metal (M = Zn, Fe, Cu, Mg, etc.) and Fe(CN)₆ is the HCF. The M and Fe (III) atoms are separated and bonded by CN bridges and occupy alternating sites within the structure [7], [46]. Fe (III) bonds with C to form FeC₆ octahedra, while M bonds with N to form MN₆ octahedra, as shown in Figure

2-12 [16]. Other atoms and water molecules may occupy the large interstitial sites within HCF and are sometimes written as $A_xM[Fe(CN)_6]_y \cdot zH_2O$ ($A = Li, Na, K, \text{etc.}$) [16]. The large interstitial sites of HCF materials are where guest ions intercalate upon battery cycling. When used as a cathode for ZIBs, HCF materials generally show high Coulombic efficiencies greater than 95% and discharge potentials between 1.1 and 1.7 V versus Zn/Zn^{2+} [34], [36], [46], [48], [49], [77]. However, maximum capacities achieved for HCF materials are usually between 50-70 mAh g^{-1} at specific currents at or below 60 mA g^{-1} . The capacity of HCF materials is determined by the amount of Fe (III) and M ions that can be reduced upon guest ion insertion.

CuHCF is one of the most studied HCF materials for cathode use and is depicted in Figure 2-12. It has a general composition of $KCuFe(CN)_6 \cdot zH_2O$. Potassium ions are usually found in the interstitial sites of the material but are typically not shown in the crystal structure schematics. Figure 2-12 shows the large interstitial sites of CuHCF, where Zn^{2+} intercalation occurs on discharge. The general reactions that occur at the CuHCF cathode and Zn anode on charge and discharge are presented in Equations (2-17) and (2-18) [46]:



where $0 < x < 0.5$. Equations (2-17) and (2-18) are also representative of the intercalation mechanism for other HCF materials. It has been reported that $Fe(CN)_6$ vacancies and the insertion of water molecules in the host HCF material aid in the insertion of Zn^{2+} by reducing steric hinderance [77]. However, the capacity of CuHCF can be affected by inconsistent ferricyanide vacancy concentrations, varying hydration, incomplete reduction and oxidation of HCF, and structural damage upon ion insertion and extraction [7], [16], [77]. Trocoli and La Mantia were able to develop a zinc-ion battery using CuHCF with an average discharge potential of 1.73 V vs. Zn/Zn^{2+} and a capacity retention of 96.3% after 100 cycles at a specific current of 60 mA g^{-1} [46]. However, the maximum capacity obtained was only 56 mAh g^{-1} . Furthermore, they observed H_2 generation and ZnO precipitation at the anode during the first few cycles of testing, but not after the cathode stabilized. $ZnHCF$ was also studied as a candidate cathode material and showed similar

performance to CuHCF. The ZnHCF battery developed by Zhang et al. achieved an average discharge voltage of 1.7 V vs. Zn/Zn^{2+} with a capacity retention of 76% after 100 cycles, while operating at a specific current of 60 mA g^{-1} [49]. However, the cathode displayed a low capacity of 65.4 mAh g^{-1} . A reaction similar to that for CuHCF was observed at the cathode for ZnHCF. Other HCF materials such as NiHCF and FeHCF have also been studied using ionic liquids and organic electrolytes, but suffer from severe capacity fading at specific discharge currents greater than 10 mA g^{-1} and operate at average discharge potentials of 1.1 V [34], [36], [76]. The severe fade in capacity at higher current densities was explained by the relatively low conductivities and higher viscosities of the organic and ionic liquid electrolytes [36], [76]. Table 2-3 contains further details regarding individual ZIBs using various HCF cathode materials and electrolytes.

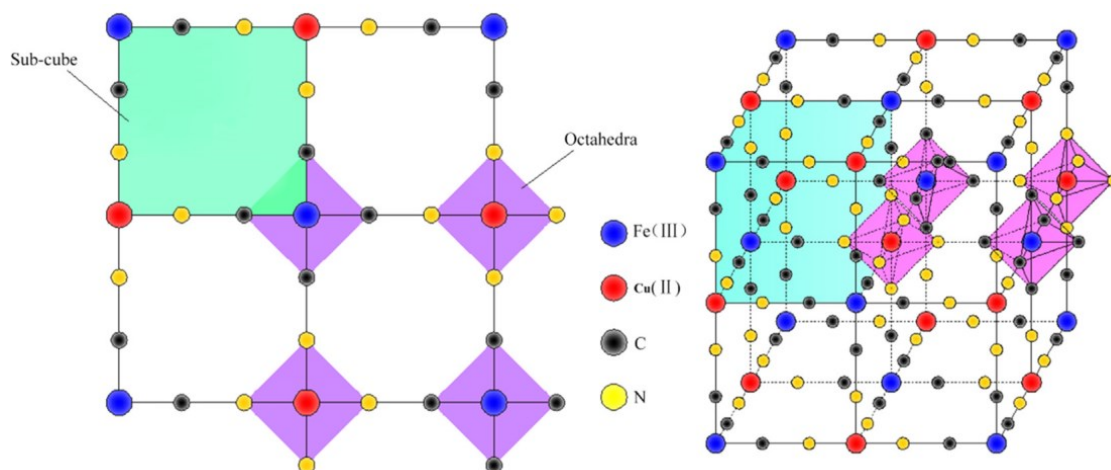


Figure 2-12 Structure of Prussian blue analogue CuHCF [48]. The large interstitial sites facilitate Zn^{2+} intercalation.

2.3.3.3 Vanadium Oxides

Vanadium oxide materials have garnered much interest as cathode materials for ZIBs in the last few years. This is due to the ability of V to occupy several different stable valence states and crystal structures, similar to Mn. Vanadium oxide materials used for ZIBs are composed of several different polyhedra (Figure 2-13): tetrahedron, square pyramidal, trigonal bipyramidal, distorted and undistorted octahedral.

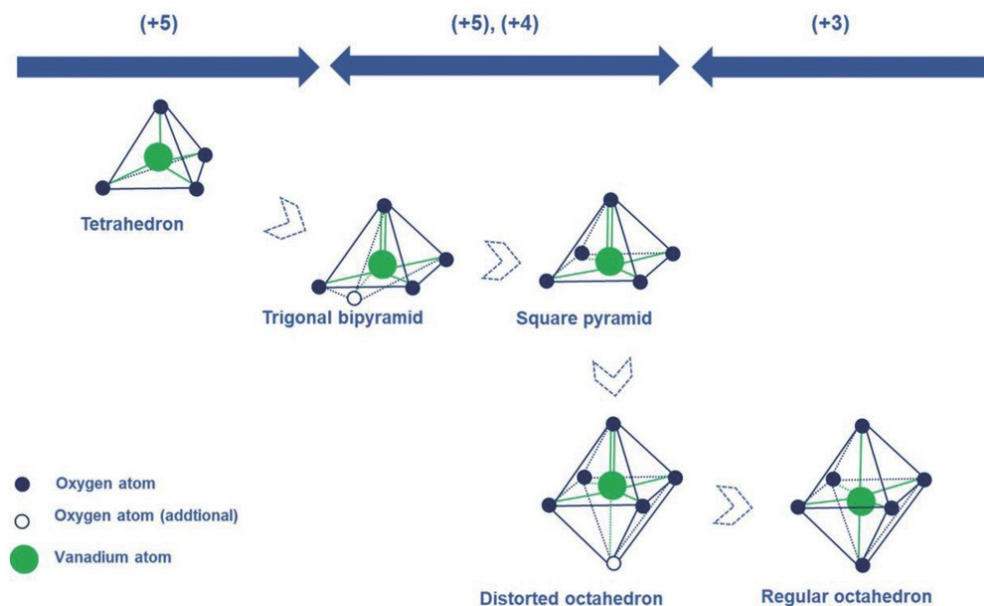


Figure 2-13 Change of V polyhedra structures with the addition of O atoms. Double bonds represent shorter bond lengths [16].

In general, V oxide materials used for ZIBs have a layered, porous structure that allows for the easy insertion and extraction of Zn ions. The layered structure is composed of a V polyhedron or a combination of several V polyhedra, but it can also be composed of ZnO [37], [38], [44], [78]. The layered structures are generally bonded together and separated by water molecules via hydrogen bonding, ZnO₆ polyhedra, pillars of V oxide, or a combination of water and ZnO₆ [37], [38], [44], [78]. The most commonly studied oxide for ZIBs is V₂O₅ and its variations [37], [79]–[84]. While relatively cheap, V₂O₅ and other V oxide materials are slightly toxic to humans [85], [86].

Overwhelmingly, the literature indicates that V oxide cathode materials store charge in ZIBs via the intercalation of Zn²⁺ ions [2], [12], [15], [16], [31]. Equations (2-19) and (2-20) represent an intercalation reaction that may occur in V oxide cathodes [84]. Intercalation reactions for other V oxide cathodes have also been proposed in the literature. However, there is one case where a combination H⁺ and Zn²⁺ intercalation mechanism was proposed for a battery using a V oxide cathode [87].



During Zn intercalation, water molecules are expelled from the structure and reinserted upon recharge [38]. The removal and insertion of water is accompanied by a change in material dimensions. It was discovered that the water molecules in the cathode structure aided in the insertion and removal of Zn ions. This is due to the water molecules coordinating with Zn^{2+} and reducing its effective charge by shielding the Zn ions, which enables fast Zn ion transport; the structural water molecules act as a lubricant to facilitate Zn intercalation [37], [81], [88], [89]. Metal ions hydrated by water molecules have also been reported to help stabilize V oxide structures by filling in vacant sites and forming pillars between the V oxide layers [2], [44], [87], [90]. Furthermore, H_2 evolution and Zn dendrite formation do not occur during battery testing. However, the potential window of V oxide is limited due to the generation of structural stress that can cause capacity fading with the intercalation/deintercalation of large amounts of Zn and the possibility of side reactions occurring [38]. Additionally, many V oxide materials still suffer from strong interactions between Zn^{2+} and the host material, which can result in poor intercalation kinetics and trapping of Zn^{2+} within the cathode lattice and the formation of a Zn containing phase [37], [80], [91], [92].

ZIBs using V oxide cathodes have an average operating voltage of 0.8 V versus Zn/Zn^{2+} , Coulombic efficiencies greater than 96%, and maximum capacities between 200 and 400 mAh g^{-1} while operating at specific currents between 50 and 100 mA g^{-1} [37], [38], [44], [78], [79], [87]. Kundu et al developed one of the better performing V oxide compounds. A single crystal $Zn_{0.25}V_2O_5 \cdot yH_2O$ nanobelt cathode material was developed that was able to achieve a large capacity of 260 mAh g^{-1} while retaining 80% capacity after 1000 cycles at a specific current of 2.4 A g^{-1} [38]. Figure 2-14 depicts the V oxide structure produced by Kundu et al. The layered structure is made of various different V oxide polyhedra, while the channels are bonded and separated by water molecules and ZnO_6 . The Zn insertion and extraction process is also depicted in Figure 2-14.

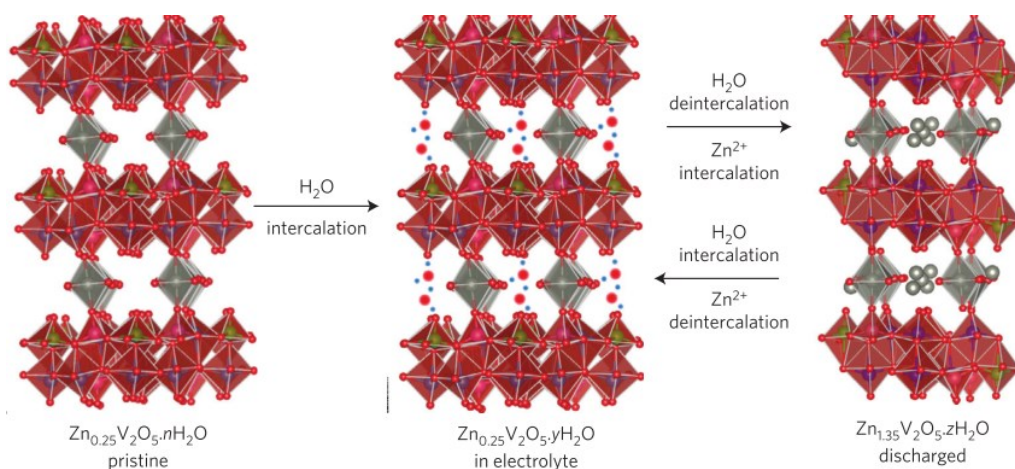


Figure 2-14 Depiction of the reversible intercalation of water and Zn^{2+} in Zn. Red spheres represent O, blue spheres represent H, and grey spheres represent Zn^{2+} . V atoms in VO_6 , VO_5 , and VO_4 polyhedra are represented as green, purple, and magenta spheres, respectively [38].

Wan et al. developed a ZIB capable of a large capacity of 380 mAh g^{-1} under an applied specific current of 100 mA g^{-1} that used a $\text{NaV}_3\text{O}_8 \cdot 1.5\text{H}_2\text{O}$ cathode and an electrolyte containing both ZnSO_4 and Na_2SO_4 [87]. They also achieved a capacity retention of 82% after 1000 cycles using a specific current of 4 A g^{-1} . He et al. developed a ZIB using $\text{H}_2\text{V}_3\text{O}_8$ as the cathode and was able to achieve a high capacity of 423.8 mAh g^{-1} at a specific current of 100 mA g^{-1} [78]. Additionally, they were able to maintain 93.6% capacity after 1000 cycles at a high specific current of 5 A g^{-1} . However, the battery consisted of a $\text{Zn}(\text{CF}_3\text{SO}_3)_2$ electrolyte, rather than ZnSO_4 or a combination ZnSO_4 and MnSO_4 that is most commonly used. As mentioned before, $\text{Zn}(\text{CF}_3\text{SO}_3)_2$ has enhanced capacity and cyclability compared with ZnSO_4 , but it is also 60 times more expensive. It should be noted that a significant number of the ZIBs that use V oxide cathodes use $\text{Zn}(\text{CF}_3\text{SO}_3)_2$ as the electrolyte. The V oxide based batteries using $\text{Zn}(\text{CF}_3\text{SO}_3)_2$ also typically show superior cyclability and capacity performance compared with the batteries that do not. For example, Qin et al. developed a ZIB that was able to achieve an excellent capacity of 132 mAh g^{-1} and maintain 82.5% of its initial capacity after 6200 cycles at an applied specific current of 10 A g^{-1} [84]. This was achieved using V_2O_5 hollow spheres as the cathode material and a $\text{Zn}(\text{CF}_3\text{SO}_3)_2$ electrolyte. While generally showing better stability versus Mn oxide materials, the low potential window of V oxide materials is still an issue restricting the wide adoption of V oxide cathodes.

Further details on the individual performances of ZIBs using V oxide cathodes can be found in Table 2-3.

2.3.3.4 Other Materials

There are a variety of other materials that have been considered for use as cathodes in ZIBs, including Chevrel phase compounds, sustainable quinone compounds, polyanion compounds and others [93]–[102]. These materials have not been studied in as much depth as Mn oxide, V oxide and HCF compounds and have only been explored fairly recently in the literature.

Liu et al. explored MoO_3 , TiO_2 , Fe_3O_4 , MoS_2 , WS_2 and MnS as potential cathode materials [102]. However, all these materials showed poor capacity, poor reversibility, poor charge retention or a combination of the three. Recently, Zhao et al. described a ZIB using organic calix[4]quinone as the cathode [97]. The battery was able to achieve a capacity of 335 mAh g^{-1} at an applied specific current of 20 mA g^{-1} while maintaining 87% of its initial capacity after 1000 cycles at an applied specific current of 500 mA g^{-1} [97]. One of the better forming polyanion compounds for ZIBs was developed by Li et al., who used $\text{Na}_3\text{V}_2(\text{PO}_4)_2\text{F}_3$ as the cathode material [93]. The battery was able to achieve a capacity of 62 mAh g^{-1} with an applied specific current of 200 mA g^{-1} and maintained 95% capacity after 4000 cycles with an applied specific current of 1 A g^{-1} [93]. Regarding Chevrel phase compounds, Cheng et al. produced a Mo_6S_8 cathode that was able to achieve a capacity of 90 mAh g^{-1} under an applied current of 0.1 C [99]. They also achieved good cyclability with a capacity retention of roughly 94% after 350 cycles at an applied specific current of 600 mA g^{-1} [99]. Further information regarding the individual performance of the discussed materials and other cathode materials can be found in Table 2-3. Figure 2-15 summarizes the various cathode materials that have been used for ZIBs and compares them in terms of operating voltage and capacities.

Other battery systems based on Zn anodes or Zn-based electrolytes have also been studied in the literature. While these systems may utilize a Zn anode or Zn containing electrolyte, other metal ions are involved in the reaction mechanism or they are considered to be hybrid supercapacitors. These batteries are not classified as ZIBs as they do not involve the intercalation or conversion of Zn/Zn^{2+} . Hybrid batteries generally involve the intercalation of Na, Li, Al or the

adsorption or desorption of ions [9], [43], [103]–[105]. Therefore, hybrid battery systems are not discussed, as they are not true ZIBs.

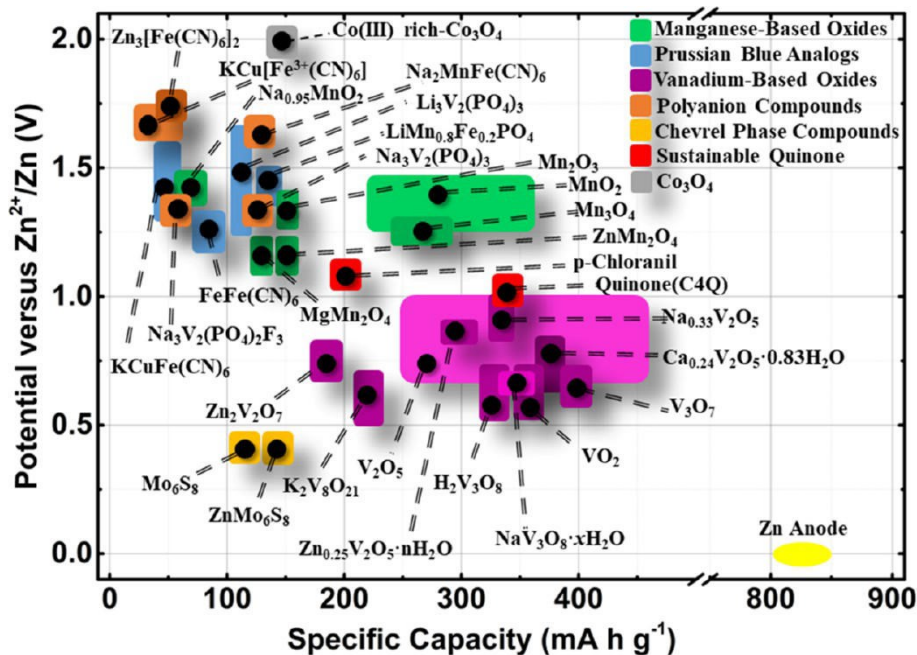


Figure 2-15 Plot of operating voltage versus specific capacity of different cathode materials and the Zn anode that have been used for ZIBs [31].

2.4 Cathode Synthesis Methods

Synthesis of the cathode material is very important for the development and acceptance of ZIBs. The fabrication method should be relatively cheap, easily reproducible and consistent from sample to sample. Most commonly, the cathode materials are fabricated using different powder production methods, with hydrothermal synthesis and solution precipitation methods being the most popular [21], [22], [28], [30], [32], [40], [55], [56], [78], [91]. Purchased powder materials have also been used for cathodes [41], [43]. Once the powder is produced, it is mixed with a binder and carbon black in solution to form a paste. The paste is then applied to a current collector, which is generally made of stainless steel or Ti with varying thicknesses. Once applied, the cathode is heated for several hours to remove the binder and to allow the solution to evaporate. The paste application method is relatively simple and allows for easy deposition onto the substrate material.

However, the paste application method requires a lot of time and heat to remove the binder material and the deposit may not always be uniform. Another relatively easy to use synthesis and application method is electrodeposition. This method combines the material synthesis and application methods into one-step. While electrodeposition is widely used method for many applications, it is not readily employed for the fabrication of cathodes in ZIBs. Other synthesis methods that have also been used for fabrication of cathodes are mentioned in Table 2-3.

2.4.1 Hydrothermal Synthesis

Hydrothermal synthesis of powder materials is described as the heterogeneous reaction of species occurring in water solvent at temperatures and pressures above 100°C and 1 bar (101.325 kPa), respectively [106], [107]. This method is easy to implement and has the ability to produce a wide variety of materials. Hydrothermal synthesis requires the use of an autoclave to reach the necessary temperature and pressure conditions for the reaction to occur and to produce precipitates. Temperature, time, pressure, and nature of the solvent all influence the shape, crystallinity, and size distribution of the powders, allowing for good control over the process [107]. Hydrothermal synthesis of powder particles has several advantages, including the use of cheap raw materials, controlled particle size and shape, low impurity content, and no requirement of post heat treatment [106]. However, initial equipment costs are very high, particles have a tendency to aggregate, there is potential for contamination due to corrosion, and there is a need to implement stringent safety requirements [106]. This method also is very time consuming compared with other methods, as materials may be in an autoclave for up to 24h [22], [28], [56].

2.4.2 Solution Precipitation

Solution precipitation is another commonly used method to produce materials for cathodes, because it is cheap and straightforward to implement [107], [108]. Knowledge of nucleation, growth, and supersaturation are key in implementing this process [107], [108]. In general, the method involves reactions of chemicals in solution to produce an insoluble product that precipitates out. Coprecipitation is a particular solution precipitation method where products that are generally soluble under set conditions will precipitate out of the solution. Solution precipitation

methods may also be known by other names, such as drip precipitation, redox precipitation, and precipitation reaction. Several different parameters can be controlled to influence cathode material precipitation. Temperature, pressure, concentration, pH, stir rate, precursors, inhibitors, surfactants, and reaction time all play a role in controlling size, shape, and particle distribution of the cathode material [107]. The large number of controllable parameters allows for fine-tuning of the process, but also makes the process difficult to control. Depending on the particle size and shape, the particles can be separated from solution using filters, settling, or centrifuges.

2.4.3 Electrodeposition

Electrodeposition involves the deposition of a species in solution onto a conductive substrate by applying an external potential. Electrodeposition has been adopted for many applications because it is inexpensive, simple to use, and can uniformly coat very complex objects of varying size. Additionally, electrodeposition can be done at room temperature without the requirement of vacuum systems and does not require the use of binder materials. Electrodeposition is a relatively fast technique, since the material synthesis step and electrode fabrication are combined into a single step. The deposited material properties are influenced by several parameters, such as stir rate, temperature, electrolyte concentration, pH, substrate material, current, and potential [109], [110]. The large number of variable parameters allows for precise control of the deposited material.

The two major electrodeposition techniques are cathodic deposition and anodic deposition. Cathodic deposition involves the reduction of species in solution from a higher oxidation state to a lower oxidation state. Anodic deposition involves the oxidation of species in solution from a lower oxidation state to a higher oxidation state. Both electrodeposition methods can be done under galvanostatic or potentiostatic conditions. Galvanostatic deposition allows for control over reaction rate, providing control over morphology and strong adhesion [109]. However, the deposited material may contain multiple phases due to changing potential during deposition. Potentiostatic deposition allows for the deposition of a pure product, but reaction rates are inconsistent as current will rapidly decay during the process [109]. Potentiostatic electrodeposition requires a three electrode system, while galvanostatic electrodeposition can be conducted with a two electrode system [111].

Only a handful of groups have used electrodeposition to fabricate cathode materials for ZIBs [39], [65], [68], [71], [112]. Sun et al. deposited MnO_2 by anodic deposition of the Mn^{2+} within the assembled battery using the ZIB electrolyte solution onto carbon fiber paper (CFP). A three-electrode set-up was used, with the CFP as the working electrode and Zn foil as the counter and reference electrode [39]. An aqueous electrolyte consisting of 2 M ZnSO_4 and 0.2 M MnSO_4 was used for deposition. The CFP was galvanostatically charged at 0.2 mA cm^{-2} to 1.8 V (vs Zn/Zn^{2+}) and then held at 1.8 V for 8 h [39]. The CFP with the MnO_2 deposit was then dried at 80°C overnight in a vacuum for characterization purposes [39]. Figure 2-16 shows the MnO_2 deposit on CFP. The MnO_2 deposit appears to be composed of interconnected nanoflakes which gives the material a very porous structure (Figure 2-16) [39]. Li et al. employed a similar method for fabricating MnO_2 cathodes, using an electrolyte of 0.2 M MnSO_4 and 1 M ZnSO_4 at an applied current density of 0.01 mA cm^{-2} for 30 h [71].

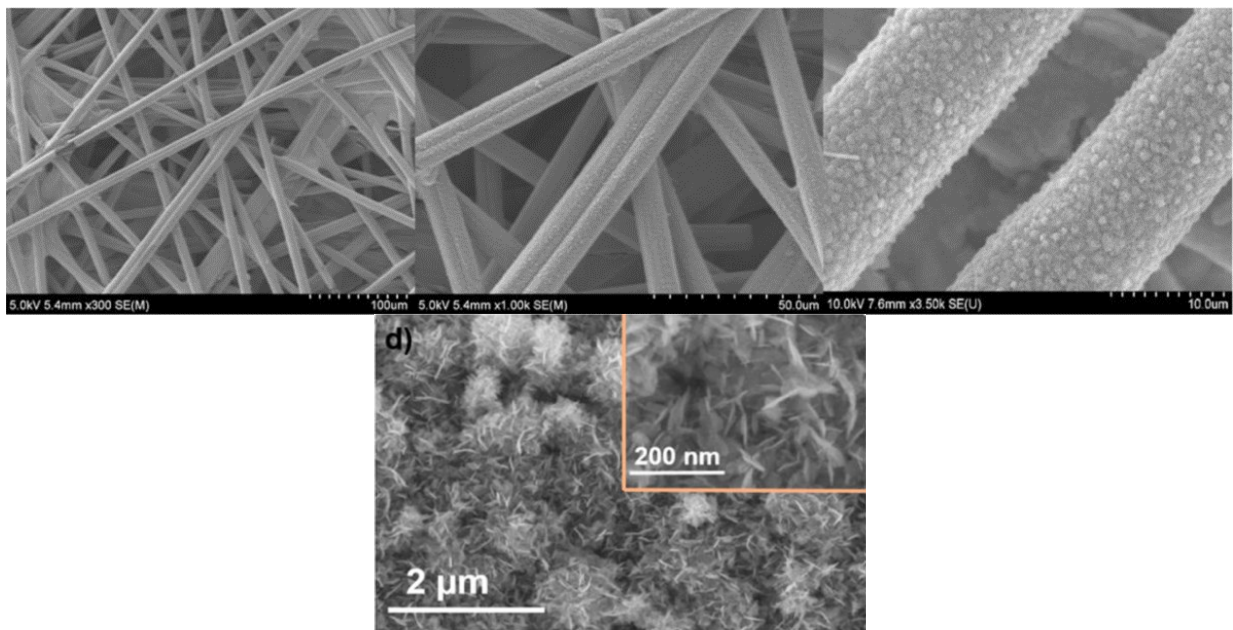


Figure 2-16 SEM secondary electron (SE) images of electrodeposited MnO_2 by Sun et al. [39]. a)-c) MnO_2 showing uniform coverage of CFP. d) interconnected nanoflake structure of MnO_2 .

Table 2-3 List of cathode materials used for ZIBs and their synthesis method, proposed reaction mechanism, and performance.

Cathode	Synthesis	Reaction Mechanism	Mass Loading (mg cm ⁻²)	Specific Current (mA g ⁻¹)	Capacity (mAh g ⁻¹)	Capacity Retention	Potential Range (V) vs Zn/Zn ²⁺	Electrolyte	Ref.
3D-NRAs-V₂O₅	Condensed Xerogel	Intercalation	-	50	336	85% after 5000 cycles at 10 A g ⁻¹	0.4 - 1.6	1M Zn(ClO ₄) ₂	[113]
Ag_{0.4}V₂O₅	Hydrothermal	Displacement/ Intercalation	-	500	335*	77% after 1000 cycles at 5000 mA g ⁻¹ *	0.4 - 1.4	3M ZnSO ₄	[114]
Birnessite MnO₂ @ CNF	Electroless deposition	Intercalation / Pseudocapacitance	-	308	305	73% after 1000 cycles at 3080 mA g ⁻¹ *	0.9 - 1.9	0.25M ZnSO ₄ + 0.75M Na ₂ SO ₄	[115]
BL-V₂O₅*nH₂O @ CFS	Electrodeposition	Intercalation	3.2	14.4	196	87% after 120 cycles at 14.4 mA g ⁻¹ *	0.3 - 1.5	0.5M Zn(CF ₃ SO ₃) ₂ in Acetonitrile	[112]
Ca_{0.24}V₂O₅*0.83H₂O	Hydrothermal	Intercalation	5.7	0.2C	340	64% after 5000 cycles at 80C*	0.6 - 1.6	1M ZnSO ₄	[116]
Calix[4]quinone	diazotization-coupling reaction	Intercalation	2.5 - 10.0	20	335	87% after 1000 cycles at 500 mA g ⁻¹	0.8 - 1.3	3M Zn(CF ₃ SO ₃) ₂	[97]
Co[III] rich Co₃O₄	Hydrothermal	Conversion	1.05	500	205	92% after 5000 cycles at 4000 mA g ⁻¹	0.8 - 2.2	2M ZnSO ₄ + 0.2M CoSO ₄	[117]
Cu²⁺ intercalated V₂O₅	Hydrothermal	Intercalation	-	1000	359	88% after 10000 cycles at 10 A g ⁻¹	0.3 - 1.4	2M ZnSO ₄	[118]
FeFe(CN)₆	Solution precipitation	Intercalation	20.0	0.1	54	96% after 50 cycles at 5 mA g ⁻¹ *	0.5 - 1.8	1M Zn(CH ₃ COO) ₂ + [Ch] (CH ₃ COO) (70%)	[34]
FeFe(CN)₆	Solution precipitation	Intercalation	5.0	10	122	94% after 10 cycles at 10 mA g ⁻¹ *	0.8 - 2.0	1M Zn(CH ₃ COO) ₂ + [Ch](CH ₃ COO) (70%)	[76]

H₂V₃O₈	Hydrothermal	Intercalation	1.2	100	423.8	94.3% after 1000 cycles at 5000 mA g ⁻¹	0.2-1.6	3M Zn(CF ₃ SO ₃) ₂	[78]
H₂V₃O₈ / graphene	Hydrothermal	Intercalation	1.0	100	394	87% after 2000 cycles at 6000 mA g ⁻¹	0.2-1.6	3M Zn(CF ₃ SO ₃) ₂	[119]
KCuFe(CN)₆	Coprecipitation	Intercalation	-	20	56	77% after 20 cycles at 20 mA g ⁻¹	0.0 - 1.1	1M ZnSO ₄	[48]
KCuFe(CN)₆	Coprecipitation	Intercalation	5.0	60	52.7*	96.3% after 100 cycles at 60 mA g ⁻¹	1.4 - 2.2 Vs SCE	0.02M ZnSO ₄	[46]
K_{0.86}Ni[Fe(CN)₆]_{0.954}(H₂O)_{0.766}	Precipitation	Intercalation	2.2	11.2	55.6	90% after 35 cycles at varying rates	0.7 - 1.8	0.5M Zn(ClO ₄) ₂ in acetonitrile	[36]
K₂V₆O₁₆*2.7H₂O	Hydrothermal	Intercalation	3.0	200	329.6	82% after 495 cycles at 6000 mA g ⁻¹	0.4 - 1.4	1M ZnSO ₄	[120]
K₂V₈O₂₁	Hydrothermal	Intercalation	-	300	247	-	0.4 - 1.4	2M ZnSO ₄	[90]
K_{0.07}Zn[Fe(CN)₆]_{0.69}	Coprecipitation	Intercalation	8.0	60	66.5	80% after 200 cycles at 300 mA g ⁻¹	0.8 - 2.0	3M ZnSO ₄	[121]
Layered MnO₂	Thermal decomposition	Intercalation	-	100	233	42% after 50 cycles at 100 mA g ⁻¹ *	1.0 - 1.8	1M ZnSO ₄	[54]
LiV₂(PO₄)₃	Spray drying / electrochemical extraction	Intercalation	10.0	300	168	86% after 500 cycles at 300 mA g ⁻¹ *	0.2 - 1.9	4M Zn(CF ₃ SO ₃) ₂	[122]
LiV₃O₈	Ball milling	Intercalation	-	133	200	75% after 65 cycles at 133 mA g ⁻¹	0.6 - 1.2	1M ZnSO ₄	[123]
MgMn₂O₄	Pyrosynthesis	Co-intercalation	3.0 - 3.5	100	269	80% after 500 cycles at 500 mA g ⁻¹	0.5 - 1.9	1M ZnSO ₄ + 1M MgSO ₄ + 0.1M MnSO ₄	[62]

Mn₃O₄	Solution precipitation	Co-intercalation	-	100	239.2	72% after 300 cycles at 500 mA g ⁻¹ *	0.8 - 1.9	2M ZnSO ₄	[42]
MnO₂	Hydrothermal	Intercalation	3.5	5000	115.9	97.7% after 4000 cycles at 5000 mA g ⁻¹	0.8 - 1.8	3M Zn(CF ₃ SO ₃) ₂ + 0.1M Mn(CF ₃ SO ₃) ₂ + 2vol% Et ₂ O	[124]
MnO₂	Electrodeposition	H intercalation	0.23	500	253.8	56.7% after 200 cycles at 200 mA g ⁻¹ *	1.0 - 1.8	2M ZnSO ₄ + 0.1M MnSO ₄	[68]
MnO₂	Electrodeposition	Intercalation and conversion	0.54	114.7	400	64% after 1000 cycles at 10.32 A g ⁻¹	1.0 - 1.8	1M ZnSO ₄ + 0.2M MnSO ₄	[71]
MnO₂	purchased	Co-intercalation	5.0 - 10.0	60	232*	233% after 100 cycles at 60 mA g ⁻¹ *	1.0 - 1.8	2M ZnSO ₄ + 0.1M MnSO ₄	[125]
MnO₂ / CF	Purchased	Conversion	10.0	70	158	N/A	0.8 - 1.5	ZnCl ₂ + NH ₄ Cl	[126]
MnO₂ / PEDOT	Electrodeposition	N/A	5.38	740	366.6	83.7% after 300 cycles at 1860 mA g ⁻¹	1.0 - 1.8	2M ZnCl ₂ + 0.4M MnSO ₄	[65]
MnOOH / MnO₂	Coprecipitation	Intercalation	2.0 - 3.0	100	248	93.9% after 2000 cycles at 4000 mA g ⁻¹	1.0 - 1.85	1M ZnSO ₄ + 0.1M MnSO ₄	[64]
MnOx@N-C	Hydrothermal / solvothermal	Intercalation	1.5	100	385	116% after 1600 cycles at 2000 mA g ⁻¹ *	0.8 - 1.8	2M ZnSO ₄ + 0.1M MnSO ₄	[127]
MnS	Purchased	Intercalation	-	100	221	63.6% after 100 cycles at 500 mA g ⁻¹	1.0 - 1.8	2M ZnSO ₄	[102]
MoO₂ / Mo₂N	Hydrothermal / thermal treatment	Intercalation	-	1000	113	78.8% after 1000 cycles at 1000 mA g ⁻¹	0.25 - 1.35	Zn(CF ₃ SO ₃) ₂	[101]
Mo₆S₈	Solid-state synthesis / copper-ion extraction	Intercalation	4.9	6.4	134	-	0.25 - 1.0	0.1M ZnSO ₄	[100]

Mo₆S₈	Precipitation / solid-state synthesis / acid leaching	Intercalation	1.0	0.1C	90	94% after 350 cycles at 600 mA g ⁻¹ *	0.25 - 1.0	1.1M ZnSO ₄	[99]
MoS₂	Hydrothermal	Intercalation	7-8	100	232	-	0.2 - 1.4	Zn(CF ₃ SO ₃) ₂	[128]
Na_{1.1}V₃O_{7.9}	Precipitation / calcination	Intercalation	1.2	5000	150*	168% after 1000 cycles at 5 A g ⁻¹ *	0.4 - 1.4	-	[129]
Na_{0.33}V₂O₅	Hydrothermal	Intercalation	1.0 - 2.0	100	367.1	93% after 1000 cycles at 1000 mA g ⁻¹	0.2 - 1.6	3M Zn(CF ₃ SO ₃) ₂	[130]
Na_{1.1}V₃O_{7.9}@rGO	Hydrothermal / calcination	Intercalation	1.2	300	223	77% after 100 cycles at 300 mA g ⁻¹	0.4 - 1.4	1M Zn(CF ₃ SO ₃) ₂	[131]
Na₂V₆O₁₆*1.63H₂O	Hydrothermal	Intercalation	-	50	352	90% after 6000 cycles at 5000 mA g ⁻¹	0.2 - 1.6	3M Zn(CF ₃ SO ₃) ₂	[132]
Na₂V₆O₁₆*3H₂O	Microwave synthesis	Intercalation	3.0 - 3.5	101	361	84.5% after 1000 cycles at 14440 mA g ⁻¹	0.4 - 1.4	1M ZnSO ₄	[133]
Na₅V₁₂O₃₂	Hydrothermal	Intercalation	2.0	200	281	71% after 2000 cycles at 4000 mA g ⁻¹	0.4 - 1.4	2M ZnSO ₄	[92]
NaV₃O₈*1.5H₂O	Precipitation	Co-intercalation	2.0	100	380	82% after 1000 cycles at 4000 mA g ⁻¹	0.3 - 1.25	1M ZnSO ₄ + 1M Na ₂ SO ₄	[87]
Na₃V₂(PO₄)₂F₃	Sol-gel	Intercalation	10.0	200	62	95% after 4000 cycles at 1000 mA g ⁻¹	0.8 - 1.9	2M Zn(CF ₃ SO ₃) ₂	[93]
Na₃V₂(PO₄)₃	Spray drying / calcination	Na/Zn Co-intercalation	-	50	114	75% after 200 cycles at 500 mA g ⁻¹	0.6 - 1.8	2M Zn(CF ₃ SO ₃) ₂	[94]
Na₃V₂(PO₄)₃	Hydrothermal / calcination	Intercalation	-	50	97	74% after 100 cycles at 50 mA g ⁻¹	0.8 - 1.7	0.5M Zn(CH ₃ COO) ₂	[95]

Na₃V₂(PO₄)₃	Sol-gel	Intercalation	-	0.2C	128	84% after 200 cycles at 0.2C	0.7 - 2.1	1M LiSO ₄ + 2M ZnSO ₄	[96]
p-chloranil	Purchased	Intercalation	3.0 - 5.0	43.4	205	52.9% after 100 cycles at 43.4 mA g ⁻¹	0.8 - 1.4	1M Zn(CF ₃ SO ₃) ₂	[134]
PANI coated Ni Foam	Electrophoretic deposition / slurry casting	Intercalation	-	-	183.28	91% after 50 cycles at 5 mA cm ⁻² *	-0.2 - 0.8 vs SCE	1M ZnSO ₄ + 0.3M (NH ₄) ₂ SO ₄	[50]
PANI intercalated δ-MnO₂	Polymerization / reduction	Co-intercalation	2.0	200	280	83% after 5000 cycles at 2000 mA g ⁻¹ *	1.0 - 1.8	2M ZnSO ₄ + 0.1M MnSO ₄	[63]
PBQS	Polymerization / oxidation	Intercalation	1.0	20	203	86% after 50 cycles at 40 mA g ⁻¹	0.2 - 1.8	3M Zn(CF ₃ SO ₃) ₂	[135]
SSWM@Mn₃O₄	Thermal Decomposition	Conversion	-	100	296	100% after 500 cycles at 500 mA g ⁻¹ *	1.0 - 1.8	2M ZnSO ₄ + 0.1M MnSO ₄	[136]
Todorokite-MnO₂	Precipitation / hydrothermal	Intercalation	2.0	50	108	92% after 50 cycles at 50 mA g ⁻¹	0.7 - 2.0	1M ZnSO ₄	[30]
V_{1-x}Al_xO_{1.52}(OH)_{0.77}	Solvothermal	Intercalation	-	15	156	68% after 50 cycles at 15 mA g ⁻¹ *	0.2 - 1.13	1M ZnSO ₄	[137]
V₁₀O₂₄*12H₂O	Hydrothermal	Intercalation	2.0	200	164.5	80.1% after 3000 cycles at 10 000 mA g ⁻¹	0.7 - 1.7	3M Zn(CF ₃ SO ₃) ₂	[88]
V₂O₅	Hydrothermal	Co-Intercalation	-	50	238	80% after 2000 cycles at 2000 mA g ⁻¹	0.2 - 1.6	21 M LiTFSI + 1M Zn(CF ₃ SO ₃) ₂	[79]
V₂O₅	Precipitation	Intercalation	-	100	224	45% after 400 cycles at 1000 mA g ⁻¹ *	0.4 - 1.4	3M ZnSO ₄	[80]
V₂O₅	Ball milling	Intercalation	2.0	200	470	91.1% after 4000 cycles at 5000 mA g ⁻¹	0.2 - 1.6	3M Zn(CF ₃ SO ₃) ₂	[81]

V₂O₅	Electrospinning / calcination	Intercalation	2.0	20	319	81% after 500 cycles at 588 mA g ⁻¹	0.5 - 1.5	3M Zn(CF ₃ SO ₃) ₂	[82]
V₂O₅	Freeze dried	Intercalation	4.0	100	450	72% after 3000 cycles at 5 A g ⁻¹	0.3 - 1.6	3M Zn(CF ₃ SO ₃) ₂	[83]
V₂O₅	Solvothermal	Intercalation	1.5	200	280	82.5% after 6200 cycles at 10 A g ⁻¹	0.2 - 1.6	3.65M ZnSO ₄	[84]
V₂O₅*nH₂O / graphene	Self-assembled hydrogel	Intercalation	2.5	60	381	71% after 900 cycles at 6000 mA g ⁻¹	0.2 - 1.6	3M Zn(CF ₃ SO ₃) ₂	[37]
V₂O₅ / MWCNT	Precipitation / filtration	intercalation	3.0	500	375	78.9% after 500 cycles at 10 A g ⁻¹ *	0.2 - 1.6	2M ZnSO ₄	[138]
V₃O₇*H₂O	Microwave hydrothermal	Intercalation	-	375	375	80% after 200 cycles at 3000 mA g ⁻¹	0.4 - 1.1	1M ZnSO ₄	[89]
V⁴⁺-V₂O₅	Hydrothermal	Intercalation	1.5	1000	262.1	72% after 1000 cycles at 10 A g ⁻¹ *	0.4 - 1.4	2M ZnSO ₄	[139]
V₆O₁₃	Hydrothermal	Intercalation	1.0 - 1.5	200	360	92% after 2000 cycles at 4000 mA g ⁻¹	0.2 - 1.5	3M Zn(CF ₃ SO ₃) ₂	[140]
VO₂	Hydrothermal	Intercalation	-	100	357	91% after 300 cycles at 5C*	0.3 - 1.5	3M Zn(CF ₃ SO ₃) ₂	[141]
VS₂	Hydrothermal	Intercalation	-	50	190.3	98% after 200 cycles at 500 mA g ⁻¹	0.4 - 1.0	1M ZnSO ₄	[142]
Zn stabilized birnessite-MnO₂	Coprecipitation	Co-intercalation	-	300	358	76% after 2000 cycles at 3 A g ⁻¹ *	1.0 - 1.9	2M ZnSO ₄ + 0.1M MnSO ₄	[143]
Zn_{0.25}V₂O₅*nH₂O	Hydrothermal	Intercalation	5.0 - 7.0	50	300	80% after 1000 cycles at 2400 mA g ⁻¹	0.5 - 1.4	1M ZnSO ₄	[38]

Zn₂V₂O₇	Hydrothermal	Intercalation	3.0 - 3.5	300	227.8	85% after 1000 cycles at 4000 mA g ⁻¹	0.4 - 1.4	1M ZnSO ₄	[144]
Zn₃V₂O₇(OH)₂*2H₂O	Microwave Synthesis	Intercalation	4.0 - 5.0	50	213	68% after 300 cycles at 200 mA g ⁻¹	0.2 - 1.8	1M ZnSO ₄	[44]
Zn₄(OH)₆SO₄*5H₂O	Precipitation	Conversion	5.0	50	123.2	100% after 1500 cycles at 500 mA g ⁻¹	1.0 - 1.8	2M ZnSO ₄ + 0.24M MnSO ₄	[145]
Zn₃[Fe(CN)₆]₂	Coprecipitation	Intercalation	8.0	60	65.4	81% after 100 cycle at 300 mA g ⁻¹	0.8 - 2.0	1M ZnSO ₄	[49]
ZnHCF@MnO₂	Chemical oxidation / coprecipitation	Intercalation	1.2	100	118	77% after 1000 cycles at 500 mA g ⁻¹	1.4 - 1.9	0.5M ZnSO ₄	[146]
ZnMn₂O₄ / C	Precipitation	Intercalation	2.0	50	150	94% after 500 cycles at 500 mA g ⁻¹	0.8-1.9	3M Zn(CF ₃ SO ₃) ₂	[33]
ZnMn₂O₄ / C	Hydrothermal	Intercalation	2.0 - 3.0	3200	70.2	124% after 300 cycles at 100 mA g ⁻¹ *	0.8 - 1.9	1M ZnSO ₄ + 0.05M MnSO ₄	[32]
ZnMn₂O₄ / Mn₂O₃	Surfactant-assisted solvothermal	Intercalation	-	500	111.9	136% after 300 cycles at 500 mA g ⁻¹ *	0.8 - 1.9	1M ZnSO ₄	[66]
Zn_xMo_{2.5+y}VO_{9+z}	Hydrothermal / microwave insertion	Intercalation	-	2	220	67% after 35 cycles at 20 mA g ⁻¹ *	0.0 - 1.7	0.5 M Zn(CH ₃ COO) ₂	[91]
α-Mn₂O₃	Purchased	Intercalation	-	100	148	87% after 30 cycles at 100 mA g ⁻¹	1.0 - 1.9	2M ZnSO ₄	[41]
α-MnO₂	Hydrothermal	Intercalation	5.0	10.5	205	66% after 30 cycles at 10.5 mA g ⁻¹ (2 cycles), 42 mA g ⁻¹ (28 cycles)	0.7 - 2.0	1M ZnSO ₄	[56]

α -MnO ₂	Hydrothermal	Intercalation	5.0	10.5	195	70% after 30 cycles at 10.5 mA g ⁻¹ (2 cycles), 42 mA g ⁻¹ (28 cycles)	0.7 - 2.0	1M ZnSO ₄	[45]
α -MnO ₂	Calcination	Intercalation	-	16	323	46% after 75 cycles at 83 mA g ⁻¹ *	1.0 - 1.8	1M ZnSO ₄	[53]
α -MnO ₂	Hydrothermal	Intercalation	3.2	83	233	63% after 50 cycles at 83 mA g ⁻¹	1.0 - 1.8	1M ZnSO ₄	[28]
α -MnO ₂	Hydrothermal	Conversion	1.0 - 5.0	103	285	92% after 5000 cycles at 1540 mA g ⁻¹	1.0 - 1.8	2M ZnSO ₄ + 0.1M MnSO ₄	[21]
α -MnO ₂	Coprecipitation	Intercalation	5.0	0.5C	210	100% after 100 cycles at 6C	1.0 - 1.9	1M ZnSO ₄ or 1M Zn(NO ₃) ₂	[14]
α -MnO ₂	Hydrothermal / coprecipitation	-	-	100	145	~167.7% after 500 cycles at 500 mA g ⁻¹ *	0.9 - 1.8	PNA + 0.3 M ZnSO ₄ + 0.015M MnSO ₄	[147]
α -MnO ₂ / AT-CNT	Coprecipitation	Intercalation	-	100	665	99% after 500 cycles at 5000 mA g ⁻¹ *	1.0 - 1.9	2M ZnSO ₄ + 0.5M MnSO ₄	[47]
α -MnO ₂ @C	Coprecipitation / gel formation	Intercalation	-	66	272	69% after 50 cycles at 66 mA g ⁻¹	1.0 - 1.8	1M ZnSO ₄	[72]
α -MnO ₂ / graphene	Hydrothermal	Intercalation	-	100	382.2	94% after 3000 cycles at 3000 mA g ⁻¹	1.0 - 1.85	2M ZnSO ₄ + 0.2M MnSO ₄	[73]
α -MnO ₂ / N-doped CC	Hydrothermal / thermal reduction / acid treatment / electrodeposition	Intercalation	3.2	500	353	93.6% after 1000 cycles at 1000 mA g ⁻¹	1.0 - 1.8	2M ZnCl ₂ + 0.4M MnSO ₄	[74]
α -MnO ₂ / OLC	One pot molten salt	Intercalation	3.0 - 3.5	246	168	93% after 100 cycles at 246 mA g ⁻¹	1.0 - 1.8	1M ZnSO ₄ + 0.1M MnSO ₄	[148]

α-MnO₂ / rGO	Hydrothermal	Co-intercalation	3.0	300	332.2	96% after 500 cycles at 6 A g ⁻¹	1.0 - 1.9	2M ZnSO ₄ + 0.1M MnSO ₄	[75]
α-MnO₂ /CNT	Hydrothermal / co precipitation	Conversion	1.0 - 2.5	61.6	306	97% after 1000 cycles at 2772 mA g ⁻¹	0.8 - 1.8	Gelatin/PAM/PAN + 2M ZnSO ₄ + 0.1M MnSO ₄	[149]
α-MnO₂ / CNT / PANI	Coprecipitation / polymerization	Intercalation	-	100	317*	106% after 350 cycles at 500 mA g ⁻¹ *	1.0 - 1.8	2M ZnSO ₄ + 0.5M MnSO ₄	[150]
β-MnO₂	Microwave hydrothermal	Intercalation	2.1	100	270	75% after 200 cycles at 200 mA g ⁻¹	1.0 - 1.8	1M ZnSO ₄ + 0.1M MnSO ₄	[151]
β-MnO₂	Hydrothermal	Intercalation	2.0	200	258	94% after 2000 cycles at 2000 mA g ⁻¹	0.8 - 1.9	3M Zn(CF ₃ SO ₃) ₂ 0.1M Mn(CF ₃ SO ₃) ₂	[40]
β-MnO₂	Coprecipitation	Co-intercalation	-	100	326	78% after 700 cycles at 2000 mA g ⁻¹ *	0.98 - 1.8	3M ZnSO ₄ + 0.1M MnSO ₄	[152]
γ-MnO₂	-	Intercalation	3.0	3.33	105	65% after 65 cycles at 66.7 mA g ⁻¹ *	0.8 - 1.9	Zn(CF ₃ SO ₃) ₂ in PC+EC+PVDF	[153]
γ-MnO₂	Coprecipitation	Intercalation	-	0.05 mAh cm ⁻²	285	63% after 40 cycles at 0.5 mA cm ⁻²	1.0 - 1.8	1M ZnSO ₄	[55]
δ-MnO₂	Hydrothermal / etching	Intercalation	0.5	0.5	405	113% after 100 cycles at 1C*	1.0 - 1.8	1M ZnSO ₄ + 0.2M MnSO ₄	[154]
δ-MnO₂	Precipitation	Intercalation	1.5 - 2.0	12.3	123	48% after 125 cycles at 12.3 mA g ⁻¹ *	0.05 - 1.9	0.5M Zn(CF ₃ SO ₃) ₂ in Acetonitrile	[155]
δ-MnO₂	Microwave hydrothermal	Intercalation	-	30	210 mWh/g	34% after 80 cycles at 30 mA g ⁻¹ *	1.0 - 1.8	1M ZnSO ₄	[156]
δ-MnO₂	Thermal decomposition	Intercalation	-	83	252	92% after 100 cycles at 83 mA g ⁻¹	1.0 - 1.8	1M ZnSO ₄	[157]

δ-MnO₂	Precipitation	Co-intercalation	3.0 - 4.0	100	200	106% after 100 cycles at 100 mA g ⁻¹ *	1.0 - 1.8	1M ZnSO ₄ + 0.1M MnSO ₄	[158]
δ-MnO₂ on Graphite	Hydrothermal	Intercalation	-	200	320*	49% after 100 cycles at 400 mA g ⁻¹ *	1.0 - 1.8	1M ZnSO ₄	[159]
ϵ-MnO₂	Electrodeposition	Co-intercalation	0.6	90	290	99.3% after 10000 cycles at 1885 mA g ⁻¹	1.0 - 1.8	2M ZnSO ₄ + 0.2M MnSO ₄	[39]
λ-MnO₂	Acid leaching	Intercalation	7.0	13.6	442.6*	-	-0.8 - 1.0 vs SCE	1M ZnSO ₄	[59]

* Values were not explicitly stated in the reference and were determined from the data presented in the reference.

2.5 Characterization Techniques

Both materials and electrochemical techniques are used to characterize the various materials developed for ZIBs. Material techniques are used to determine material structure, morphology and composition, while electrochemical techniques are used to characterize the electrochemical performance and behaviour of the material.

2.5.1 X-ray Diffraction

X-ray diffraction (XRD) is a common materials characterization technique used to determine material phases and crystal structures. This method utilizes a collimated beam of X-rays which strikes the sample being analyzed. The X-ray beam is diffracted at specific angles as the sample and detector are rotated. A plot of the diffracted beam intensity versus the 2θ angle is generated. The generated XRD patterns are compared against a database of reference XRD patterns to identify the material.

X-rays are produced in a cathode ray tube by heating a filament to produce electrons, which are accelerated at high potentials and strike an anode target. The most commonly used target material is Cu; however Co, Mo, and Cr are also used [160]. The incident electrons eject inner shell electrons and produce characteristic X-rays when electrons transition from high energy levels to the inner shells. The generated X-ray spectrum consists of a combination of characteristic X-rays (K_{α} and K_{β} X-rays are usually the most intense signals) and background radiation [160]. The K_{α} X-rays are a combination of $K_{\alpha 1}$ and $K_{\alpha 2}$ X-rays, which are very similar in energy [160]. Monochromatic X-rays are required for XRD analysis. This is achieved by using filters that strongly absorb X-rays other than the desired X-rays or crystal monochromators [160]. K_{α} X-rays are the most commonly used monochromatic X-rays for XRD. Interplanar spacings (d-spacing) are calculated according to Bragg's Law, Equation (2-21):

$$\lambda = 2d \sin \theta \quad (2-21)$$

where λ (Å) is the wavelength of the K_{α} X-rays of the target material, d is the d-spacing (Å), and θ (°) is the Bragg angle of the diffracted electron beam. The d-spacing values can then be used to determine the Miller indices (hkl) of the diffracting planes and the lattice parameter(s) of the material. Using the d-spacing and the corresponding Miller indices, the material structure can be identified. XRD analysis can be used to identify phases in inorganic materials, organic materials, polymers, metals, and composites.

2.5.2 Scanning Electron Microscopy

Scanning electron microscopy (SEM) is a powerful materials characterization technique. SEM utilizes a focused electron beam under high vacuum conditions that is scanned over the surface of the sample [160]. The interaction between the sample and electron beam results in the ejection of several different electrons and photons, which are used to image the sample and collect chemical information. Brighter areas in the resulting image indicate the ejection of more electrons compared to darker areas. Generally, SEM can achieve spatial resolutions between 1 and 100 nm depending on the signal used [161]. The resolving power of SEM is dependent on several operating variables, such as electron probe size and current, accelerating voltage, working distance, and the type of signal utilized. The achievable resolution is also dependent on the instrument used. The sample material will affect the resolving power of SEM as well. Generally, the sample being imaged should be conductive to utilize SEM; non-conductive samples are usually coated with C or Au to prevent charging [160].

Generally, the emitted electrons and photons are secondary electrons (SE), back scattered electrons (BSE), and characteristic X-rays. SEs have energies typically between 3 and 5 eV and are ejected close to the surface of the sample (within 5-50 nm) [160]. SEs are typically used to obtain topographical information about the sample and have good spatial resolution (~1-5 nm) [162]. BSEs typically have energies that are 60-80% of the accelerating voltage and are ejected from deeper within the sample (50-300 nm) and have a lower spatial resolution compared to SEs (~10-100 nm) [160], [162]. BSEs provide compositional contrast; higher atomic number elements backscatter a larger number of electrons and appear brighter in images compared with lower atomic number elements. This is helpful in determining element distribution in the sample. SEM can also utilize energy dispersive X-ray spectroscopy (EDS), a technique used to determine the chemical

composition of samples. EDS measures the number and energies of characteristic X-rays emitted from the sample and presents the data in a plot of X-ray counts vs X-ray energy. During EDS operation, the incident electron beam may eject electrons from lower energy shells in the target specimen, resulting in the formation of an electron hole. Characteristic X-rays are generated when electrons from a higher energy shell drop down to fill holes in a lower energy shell, with the difference in energies between the shells being released as a characteristic X-ray [160]. Characteristic X-ray energies are well defined, specific to the elements present in the sample, and can be used to determine the elemental composition of the sample. EDS typically has a depth and spatial resolution of $\sim 1 \mu\text{m}$ due to the large sample interaction volume of X-rays.

2.5.3 Transmission Electron Microscopy

Transmission electron microscopy (TEM) is a high-resolution materials characterization technique, which utilizes a focused electron beam under high vacuum conditions that is transmitted through the sample being characterized. TEM can operate in imaging mode and diffraction mode. In imaging mode, the direct transmitted beam is used for bright field (BF) imaging and one of the diffracted beams is used for dark field (DF) imaging. There are three contrast mechanisms that affect TEM imaging: mass-density, diffraction, and phase contrast. A thorough understanding of each contrast mechanism is required to interpret BF and DF images correctly. Mass-density contrast is the primary mechanism used for imaging non-crystalline samples [160]. Mass-density contrast relies on changes in the thickness and density of the sample. A larger thickness or density results in more scattering and a lower electron intensity at the imaging plane. Diffraction contrast is the primary mechanism for image formation for crystalline samples and is very sensitive to sample tilt [160]. Diffraction contrast arises when Bragg conditions between the electron beam and sample are satisfied, resulting in strong electron diffraction [160]. Phase contrast is the primary mechanism for high-resolution (atomic scale) TEM imaging HR-TEM [160]. This mechanism relies on the collection of two or more beams. Crystalline samples generate a phase difference between the transmitted and diffracted beams, and on recombination an interference pattern is generated [160]. Electron diffraction patterns for crystalline samples can be obtained through operation in diffraction mode. Diffraction patterns can provide information regarding crystal structure and crystallographic orientation, much in the same way as X-ray diffraction [163].

Electron energy loss spectroscopy (EELS) is a TEM technique that can be used to gather composition information about the sample. This method involves the analysis of the energy distribution of electrons that have travelled through the specimen. A plot of counts versus electron energy loss is obtained. High-loss electrons (energy loss > 50 eV) are characteristic of the atoms present in the material and are used to collect information regarding chemical composition, atomic bonding, and valence states [164]. TEM instruments are also able to provide EDS compositional analysis of samples, as with the SEM. The major difference is a significant improvement in the spatial resolution for TEM EDS analysis relative to the SEM (<10 nm for TEM vs $1 \mu\text{m}$ for SEM). The improved spatial resolution is due to the smaller interaction volume for TEM samples compared with SEM samples.

TEM can achieve imaging resolutions smaller than 0.1 nm using phase contrast [160]. TEM resolution is largely influenced by accelerating voltage. However, larger accelerating voltages may damage the sample. Specimens must be less than 200 nm thick to be electronically transparent for TEM analysis, with high resolution imaging requiring even thinner samples (<50 nm) [160].

Scanning transmission electron microscopy (STEM) is essentially a hybrid of SEM and TEM. STEM utilizes a focused electron beam that is scanned across the surface of an electron transparent sample. The most common imaging mode using STEM is high angle annular dark field (HAADF) imaging. HAADF images are formed by collecting transmitted electrons that are incoherently scattered by the specimen at angles larger than 50 mrad. At high scattering angles, Bragg diffracted electrons are avoided, resulting in mass-density contrast as the imaging mode. However, sample thickness will still contribute to HAADF contrast. In addition to HAADF, STEM can also be used to collect EDS maps and line scans of the sample being imaged, which cannot be done using conventional TEM [165].

2.5.4 X-ray Photoelectron Spectroscopy

X-ray photoelectron spectroscopy (XPS) is a widely used surface analysis technique. The system is under an ultrahigh vacuum and the sample surface is bombarded with monochromatic X-rays. The incident X-rays are absorbed by the sample, leading to ejection of electrons (called photoelectrons) from the sample surface ($1-10$ nm depth) [166]. The number of ejected

photoelectrons and their kinetic energy are recorded. The kinetic energy of the ejected photoelectrons is equal to the energy of the bombarding X-rays minus the electron binding energy, as shown in Equation (2-22).

$$E_k = h\nu - E_b \quad (2-22)$$

where E_k (eV) is the kinetic energy of the emitted photoelectron, h is Plank's constant ($4.136 \cdot 10^{-15}$ eV*s), ν (Hz) is the frequency of the X-ray, and E_b (eV) is the binding energy of the ejected electron. A plot of electron counts versus the binding energy of the ejected electrons is generated. The binding energies of the ejected photoelectrons are characteristic of the atomic species within the sample and are used to identify the elements present. XPS can also provide information about the chemical state, short-range bonding, and the relative amount of each element present within the near surface region (<10 nm) of the sample [166].

2.5.5 Raman Spectroscopy

Raman spectroscopy (RS) is a technique that is used to complement other materials characterization techniques to identify material crystal structure and phase. RS uses a monochromatic laser to irradiate a sample and generate a spectrum from the scattered light [167]. The laser light will interact with the material and its energy will be shifted. The shift in the laser energy is recorded and corresponds to different vibrational modes in the material [167]. The generated spectrum is characteristic of the material and can be used to identify the sample.

RS relies on the Raman effect to generate characteristic patterns to identify materials. The Raman effect occurs when the laser light polarizes the cloud of electrons around the nuclei of a molecule [167]. This causes the molecule to be excited to an unstable virtual energy state from either a ground or excited state [167]. In the virtual state, there are three different types of light scattering that can occur as the molecule returns to either a ground or an excited state: Rayleigh scattering, Stokes scattering, and anti-Stokes scattering. The majority of light will undergo Rayleigh scattering (elastic scattering) in which the vibrational energy of the molecule does not

change [168]. This type of scattering is filtered as there is no shift in the energy of the light; the incoming photon and scattered photon have the same energy. Stokes scattering (inelastic scattering) occurs when the molecule starts at a lower vibrational state and ends at a higher vibrational state [168]. In this case, the incident photon transfers energy to the molecule, resulting in a scattered photon with lower energy. Anti-Stokes scattering (inelastic scattering) occurs when the molecule transfers energy to the scattered photon, causing the molecule to end at a lower vibrational state compared with its initial state [168]. This case results in a scattered photon with more energy than the incident photon. However, it should be noted that anti-Stokes scattering is extremely rare compared with Stokes scattering and is not commonly used for RS. Figure 2-17 shows an energy level diagram for a molecule that depicts the different types of scattering that can occur.

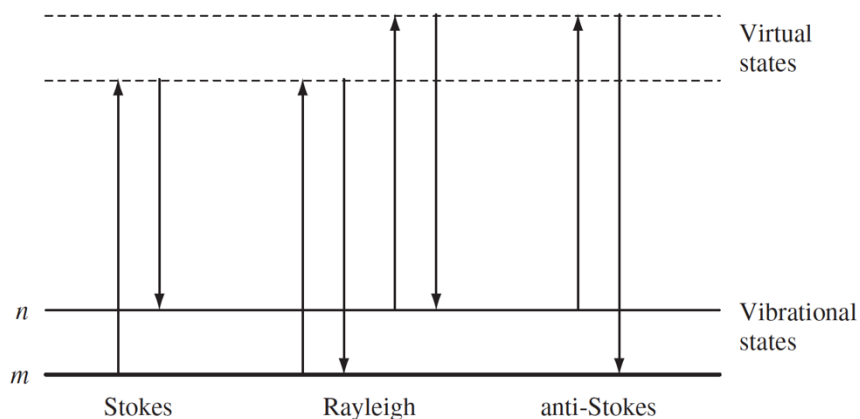


Figure 2-17 Energy level diagram for a molecule depicting the three different types of scattering that can occur [167]. Vibrational state m is at lower energy than vibrational state n . The up arrows indicate the energy of the incident photon and the excitation of the molecule to a virtual state. The down arrows indicate the energy of the scattered photon and the return of the molecule to vibrational states m or n .

2.5.6 Cyclic Voltammetry

Cyclic voltammetry (CV) is a common electrochemical characterization technique that can provide quantitative and qualitative information regarding electrode processes. CV involves the application of a linearly sweeping voltage over time between a lower and upper potential limit of

interest [169]. The collected data are presented as a graph called a voltammogram, where the x-axis is the potential and the y-axis is current, specific current, or current density. Voltammograms provide information regarding the redox reactions occurring at an electrode during battery cycling. Figure 2-18a depicts a generic voltammogram for a reversible electrochemical process. The positive current portion represents an oxidation reaction (charge) and the negative current portion represents a reduction reaction (discharge). Reversible electrochemical processes possess several well defined characteristics: voltage separation of the peak currents is equal to $(59/n)$ mV, the positions of the peak voltages remain constant for changing scan rates, the ratio of the peak currents is equal to 1, and the peak currents are proportional to the square root of the scan rate used [18]. CV testing can also show irreversible and quasi-reversible processes. The pair of current peaks for quasi-reversible processes are separated by a larger potential, they are less sharp, and the summit is more rounded (curve b in Figure 2-18b) [18]. Generally, a greater potential difference between the current peaks indicates a larger battery overpotential. There are three types of overpotentials that are observed in a battery: activation, ohmic, and concentration. Activation overpotentials are a result of poor reaction kinetics. Ohmic overpotentials arise from contact resistances and the resistance to the flow of electrons and ions throughout the cell. Concentration overpotentials are caused by poor mass transport of reactants and products, resulting in large concentration gradients. Irreversible processes only produce one current peak (oxidation or reduction) for a complete CV sweep and not a pair of redox peaks, illustrated as curve c in Figure 2-18b. The scan rate will also influence the shape of the CV curves. At low scan rates, reactions will occur under steady-state conditions as the diffusion layer will be able to reach equilibrium, resulting in smaller current peaks [170]. Higher scan rates will push the reaction further from steady-state and result in larger peaks.

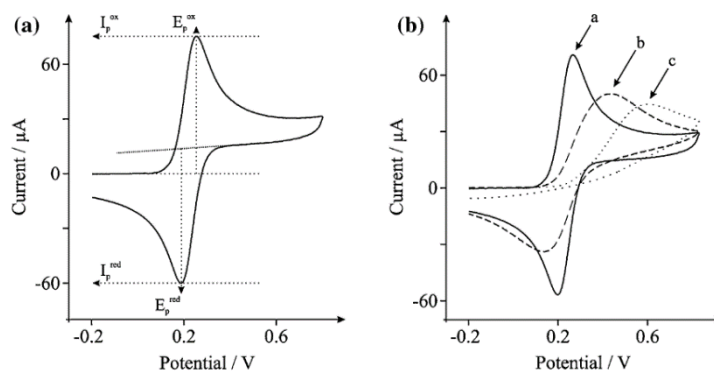


Figure 2-18 a) Generic CV curve showing peak current (I) and potential (E) positions of the reduction (red) and oxidation (ox) reactions. I_p^{ox} and E_p^{ox} represent the peak current and potential for the oxidation process, respectively. I_p^{red} and E_p^{red} represent the peak current and potential for the reduction process, respectively, b) CV curves for a) reversible, b) quasi-reversible, and c) irreversible electrochemical processes [171].

2.5.7 Galvanostatic Charge and Discharge

Galvanostatic charge and discharge (GCD) testing is another common technique used to characterize ZIBs. During GCD testing, the battery is discharged at a constant current until a lower potential limit is reached. The battery is then recharged at the same constant current until an upper potential limit is reached. The time taken to reach the upper and lower potential is recorded. The upper and lower potential limits are selected to avoid side reactions from occurring in the battery, such as H_2 and O_2 evolution. The collected data are presented as a plot where the x-axis is specific capacity (C , mAh g^{-1}) and the y-axis is potential (V). Specific capacity of the battery is determined using Equation (2-23) [14]:

$$C = I * t/m \quad (2-23)$$

where C is the specific capacity (mAh g^{-1}), I is the applied current (mA), t is the time for charge and discharge (h), and m is the active mass of the cathode material (g). GCD testing can provide information regarding the capacity of the battery at different applied currents, insight into the redox reactions occurring, Coulombic efficiency, cycling performance, and rate capability of the battery. Figure 2-19 shows a GCD curve for a ZIB tested at different applied currents. The upward sloping

curves represent the charge cycle and the downward sloping curves represent the discharge cycle. Generally, as the current applied is increased, the effective capacity of the battery is decreased.

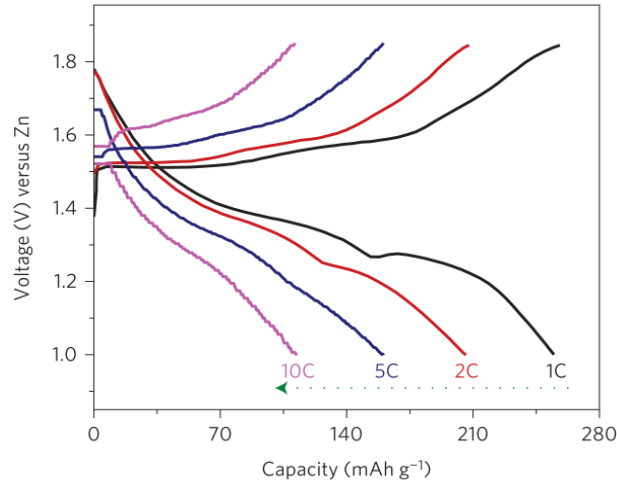


Figure 2-19 GCD curve for a ZIB tested under increasing applied currents from 1 C to 10 C [21]. The battery was composed of a Zn anode, an α - MnO_2 cathode, and an electrolyte containing 2 M $ZnSO_4$ and 0.1 M $MnSO_4$.

2.5.8 Electrochemical Impedance Spectroscopy

Electrochemical impedance spectroscopy (EIS) is used to determine and differentiate between the major sources of loss in battery systems. Unlike typical resistance measurements, EIS can measure time and frequency dependent resistances as well. Impedance measurements are made by applying a small sinusoidal voltage perturbation and monitoring the responding phase-shifted current [172]. The impedance response of a system is represented by Equation (2-24) [172];

$$Z = \frac{V_0 e^{j\omega t}}{i_0 e^{(j\omega t - j\phi)}} = Z_0 e^{j\phi} = Z_0 (\cos \phi + j \sin \phi) \quad (2-24)$$

where V_O and i_O are the voltage and current amplitude, ω is the radial frequency (Hz), Z_O is the impedance amplitude, j is the imaginary number ($j=\sqrt{-1}$), and ϕ is the phase shift between the responding current and voltage perturbation.

The impedance of the system is recorded in a Nyquist plot, which records the imaginary impedance component ($Z_i = Z_O j \sin \phi$) versus the real component ($Z_r = Z_O \cos \phi$). Equivalent circuit models are used to represent the losses recorded in the Nyquist plot. From the equivalent circuit model, ohmic, activation, and mass transport losses can be resolved separately. Figure 2-20 depicts a simple battery and its corresponding Nyquist plot and equivalent circuit model. The ohmic resistance (R_Ω) of the battery is represented as a simple resistor and is shown as a point on Nyquist plots as the intercept on the x-axis. The imaginary component of a resistor is 0 and the impedance does not change with frequency [172]. The ohmic resistor represents ohmic losses from all parts of the battery. R_Ω is sometimes referred to as contact resistance or solution resistance. Activation losses at the cathode and anode are depicted as a combination of a resistor (R_f) and capacitor (C_{dl}). R_f represents the Faradaic resistance, which models the kinetics of the electrochemical reaction [172]. C_{dl} represents the double-layer capacitance, which models the capacitive behaviour of the reaction interface [172]. The impedance of a capacitor is purely imaginary [172]. Activation loss is presented as a semi-circle region (Figure 2-20). The diameter of the semi-circle region is interpreted as the charge transfer resistance [173]. Mass transport losses are modelled using Warburg circuit elements. The Warburg circuit element can be modelled as infinite or finite, depending on thickness of the diffusion layer [172]. In Figure 2-20, mass transport is modelled using the infinite Warburg model. The Warburg impedance is shown as the positive sloped line in the low frequency region of the Nyquist plot, to the right of the semi-circles. The Warburg impedance measurement can be used to determine the diffusion coefficient of the reaction [173].

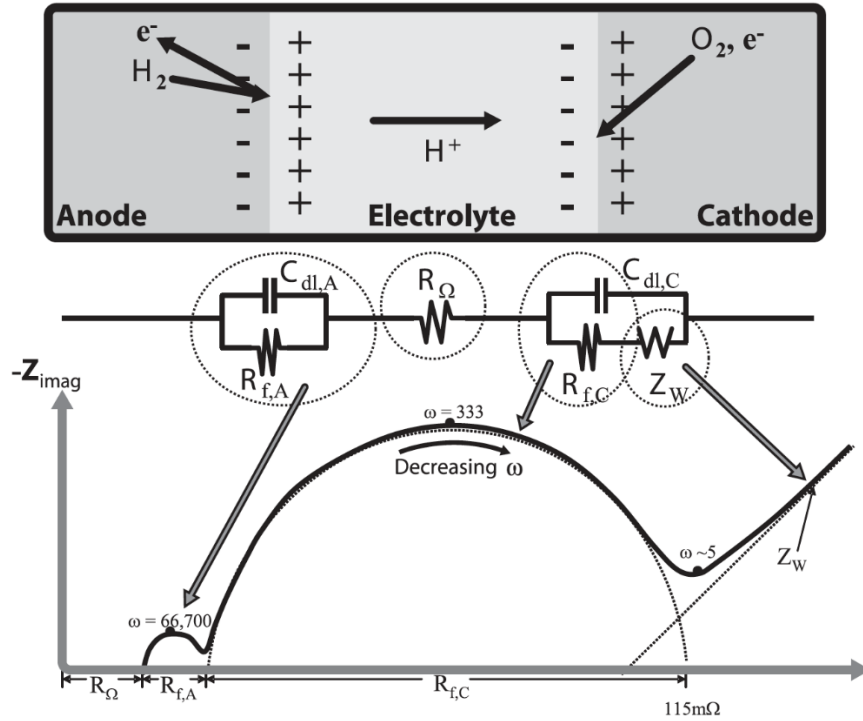


Figure 2-20 Equivalent circuit diagram and Nyquist plot for a simple battery system [172]. The ohmic resistor determines the high frequency intercept. The small semi-circle is due to the activation losses at the anode which are represented by a resistor and capacitor in parallel. The large semi-circle is due to the activation losses at the cathode. The low frequency diagonal line is from the infinite Warburg element modelling mass transport.

2.5.9 Galvanostatic Intermittent Titration Technique

Galvanostatic intermittent titration technique (GITT) testing is used to determine the diffusion coefficient of an ion within an electrode material [174]. This test can be conducted using a half-cell or a full-cell set up. Essentially, GITT involves the application of a series of galvanostatic current pulses, which are followed by a rest period where no current is applied. This test can be used for both the charge cycle and discharge cycle of a battery. Figure 2-21a shows a plot of a GITT test for one complete charge and discharge cycle of a LIB. The diffusion coefficient for an ion can be determined using the following formula [174]:

$$D = \frac{4}{\pi} \left(\frac{iV_m}{z_A FS} \right)^2 \left[\frac{\left(\frac{dE}{d\delta} \right)}{\left(\frac{dE}{d\sqrt{t}} \right)} \right]^2 \quad (2-25)$$

where D ($\text{cm}^2 \text{s}^{-1}$) is the diffusion coefficient of the ion, i (A) is the current, V_m ($\text{cm}^3 \text{mol}^{-1}$) is the molar volume of the electrode, z_A is the charge number, F (96485 C mol^{-1}) is Faraday's constant, S (cm^2) is the contact area between the electrode and electrolyte, $dE/d\delta$ is the slope of the coulometric titration curve, and $dE/d\sqrt{t}$ is the slope of the potential (V) versus linearized pulse time (s) plot. If the applied current is sufficiently small, then, $dE/d\sqrt{t}$ and $dE/d\delta$ can both be considered linear and Equation (2-25) can be simplified to the following equation [174], [175]:

$$D = \frac{4}{\pi\tau} \left(\frac{m_m V_m}{M_m S} \right)^2 \left(\frac{\Delta E_s}{\Delta E_\tau} \right)^2 \quad (2-26)$$

where τ (s) is the current pulse time, m_m (g) is the mass of the active material, M_m (g mol^{-1}) is the molar mass of the active material, S (cm^2) is the contact area between the electrode and electrolyte, ΔE_s (V) is the potential change between two consecutive rest periods, and ΔE_τ (V) is the change in potential during a constant current pulse period (V). Figure 2-21b depicts how ΔE_τ and ΔE_s are determined from the data collected for a GITT test for the charge step. The applied current, pulse time length, and rest time length will influence the calculated diffusion coefficient [176]. Applied current, pulse time, and rest time can vary for different battery systems as well as for battery systems with similar chemistries. In the literature, different applied currents and pulse periods have been used to determine the diffusion coefficient for ZIB with similar chemistries [45], [136], [177].

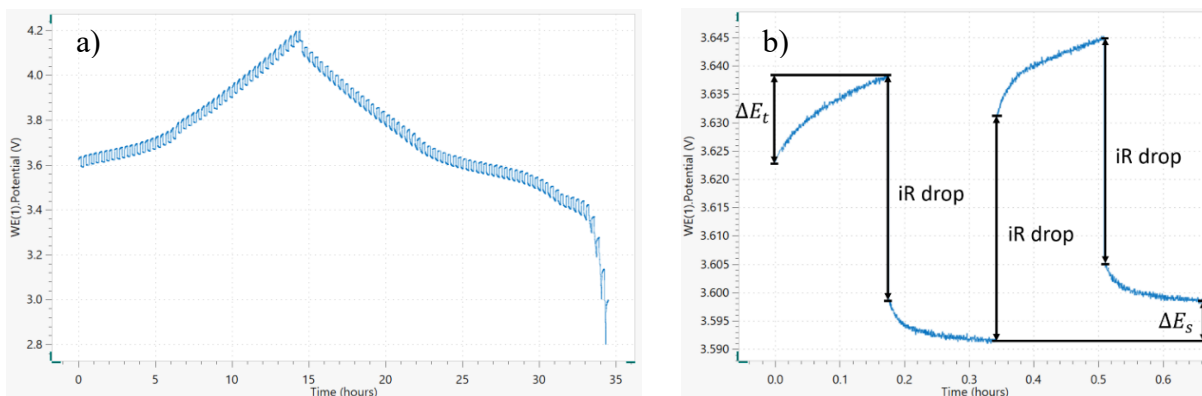


Figure 2-21 GITT results for a LIB using a 10 min pulse period, 10 min rest period, and a current of $C/10$ [178]: a) Full charge and discharge curve under GITT test conditions, b) two consecutive pulse and rest periods for the LIB charge cycle, depicting how ΔE_t and ΔE_s are determined for diffusion coefficient calculations.

2.6 Previous Work in the Ivey Group

The Ivey research group has extensive knowledge and experience with the anodic deposition of Mn oxide materials for supercapacitor applications that may translate well to ZIBs. Initial work was conducted by Babakhani and Ivey, which focused on Mn oxide electrochemical capacitors. Mn oxide was anodically deposited onto Au coated Si using two different solutions (0.01 M MnSO_4 and 0.01 M $\text{Mn}(\text{CH}_3\text{COO})_2$) at 60°C [179]. The depositions were done for 10 min with current densities ranging between 5 and 30 mA cm^{-2} ; solution pH was maintained at 6.5 and the solution was agitated using a stir bar with a speed of 300 RPM [179]. After deposition, the samples were dried for 1 h at 100°C in air. Two different structures were formed: a continuous porous layer from the MnSO_4 electrolyte and a rod-like structure from the $\text{Mn}(\text{CH}_3\text{COO})_2$ electrolyte (Figure 2-22). The rod-like structures deposited from 0.01 M $\text{Mn}(\text{CH}_3\text{COO})_2$ at 5 mA cm^{-2} and 60°C for 10 min resulted in the best electrochemical performance (185 F g^{-1}) [179]. Using TEM diffraction patterns and XPS analysis, the rod-like structure was identified as a combination of a cubic MnO_2 structure and amorphous MnOOH [179].

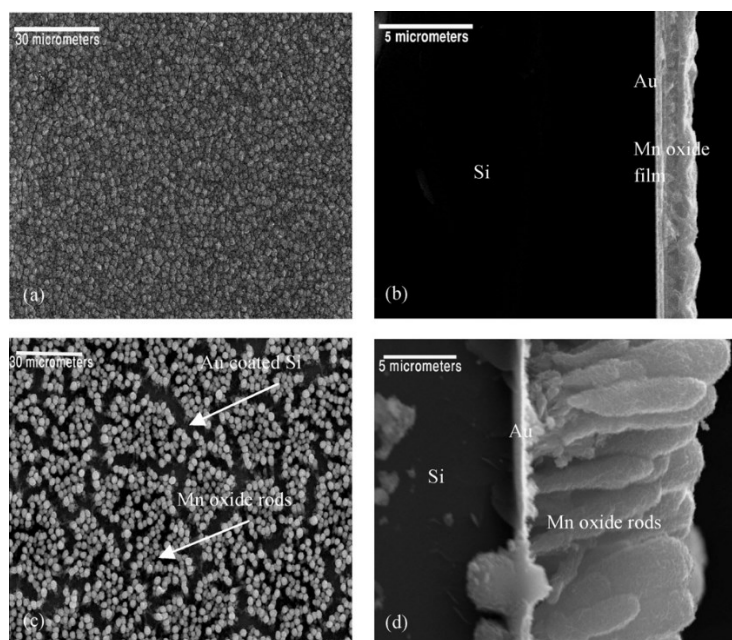


Figure 2-22 SEM SE images of plan view and cross section orientations of Mn oxide films deposited using different electrolytes. a) and b) 0.01 M MnSO_4 at 30 mA cm^{-2} , c) and d) 0.01 M $\text{Mn}(\text{CH}_3\text{COO})_2$ at 5 mA cm^{-2} . Both films were deposited for 10 min at 60°C [179].

In 2016, Clark and Ivey continued work on Mn oxide electrochemical capacitors based on the previous work conducted by Babakhani and Ivey. Manganese oxide was anodically deposited onto Ni foam using an electrolyte solution of 0.01 M $\text{Mn}(\text{CH}_3\text{COO})_2$, 0.02 M $\text{NH}_4(\text{CH}_3\text{COO})$, and 10% $\text{C}_2\text{H}_6\text{OS}$ (dimethyl sulfoxide (DMSO)) [180]. $\text{NH}_4(\text{CH}_3\text{COO})$ and DMSO were added to the electrolyte previously used by Babakhani and Ivey to improve reproducibility and deposit uniformity [181]. The depositions were done at 60°C using current densities between 5 and 20 mA cm^{-2} and deposition times between 2.5 and 10 min. The samples were then dried for 1h at 100°C . The best material coverage and performance were obtained for depositions at 20 mA cm^{-2} for 5 min using a stir speed of 75 RPM [180]. A maximum capacitance of 120 F g^{-1} (290 mF cm^{-2}) was achieved. Figure 2-23 shows the deposited Mn oxide on Ni foam using a current density of 20 mA cm^{-2} . The deposited nanorods were fibrous and were composed of nanosheets, resulting in high surface area and capacity [180]. Utilizing XPS, Clark et al. identified the deposited Mn oxide as either a cubic Mn_3O_4 (spinel) or a hexagonal MnO_2 (birnessite) [180].

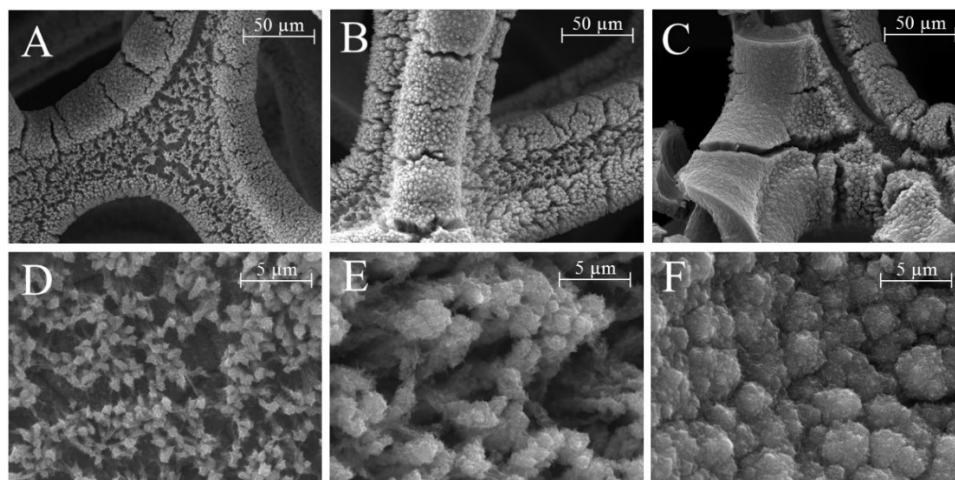


Figure 2-23 SEM SE images of Mn oxide deposited using varying deposition times: a, d) 2.5 min, b, e) 5 min, and (c, f) 10 min. All films were deposited at 20 mA cm^{-2} and 60°C using a rotation speed of 75 rpm [180].

More recently, Xiong and Ivey have used Mn oxide films as catalysts for the oxygen reduction reaction (ORR) in Zn-air batteries. Mn oxide was deposited onto carbon paper made with polytetrafluoroethylene (PTFE) binder using anodic electrodeposition, with an electrolyte consisting of 0.1 M MnSO_4 , 0.1 M NaCH_3COO , and 100 mg L^{-1} of SDS (sodium dodecyl sulfate) [182]. Depositions were done using a constant current of 40 mA for 10 min at room temperature. During deposition, the electrolytic cell was agitated by placing the cell in an ultrasonic bath. The deposited material had an irregular shape and was very porous, as shown in Figure 2-24. Using a combination of XRD and XPS, Xiong et al. identified the deposit as a combination of MnO_2 and $\text{MnOOH/Mn}_2\text{O}_3$, with more MnO_2 [182]. When used as a catalyst for both the ORR and oxygen evolution reaction (OER), the Zn-air battery was able to achieve an efficiency of 55% at an applied current density of 10 mA cm^{-2} [182]. However, when combined with a Co-Fe catalyst to create a bifunctional catalyst for both ORR and OER, the battery was able to achieve an efficiency of 62% at an applied current density of 10 mA cm^{-2} , which was better than the efficiency of Pt/C (60%) [182]. The bifunctional catalyst was then tested for stability under an applied current density of 5 mA cm^{-2} . The battery was able to maintain an efficiency of 59.6% after 13 h of cycling, similar to that for Pt-based catalysts [182].

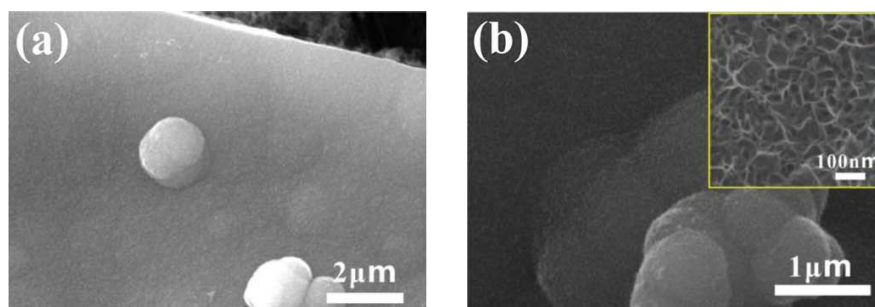


Figure 2-24 a) and b) SEM SE images of Mn oxide on porous carbon paper [182].

Xiong and Ivey continued the development of electrodeposited Mn oxide catalysts for the ORR mechanism in Zn-air batteries. Mn oxide was anodically electrodeposited on carbon paper made with PTFE binder, using an electrolyte of 0.02M $\text{Mn}(\text{CH}_3\text{COO})_2$, 0.02M NaCH_3COO , and 100 mg L^{-1} of SDS [183]. The material was pulse electrodeposited at a current of 6 mA with an ON time of 0.25 s and an OFF time of 0.5 s for each cycle. A total of 2400 cycles were completed, resulting in a total ON time of 10 min and an OFF time of 20 min. The electrolyte was agitated during deposition using an ultrasonic bath. Following the deposition, the material was annealed for 30 min at 300°C. The annealed and unannealed Mn oxide deposit are shown in Figure 2-25. Using a XPS and TEM, Xiong et al. identified the unannealed and annealed Mn oxide as a combination of cubic $\alpha\text{-Mn}_2\text{O}_3$ (bixbyite) spheres and tetragonal Mn_3O_4 (hausmannite) nanorods [183]. Both the unannealed and annealed materials were very similar in terms of morphology; however, the annealed Mn oxide possessed a higher oxidation state, as determined by XPS. The increase in oxidation state was due to the formation of $\gamma\text{-Mn}_2\text{O}_3$ during annealing [183]. At applied current densities of 2, 5, 10, and 20 mA cm^{-2} , the Mn oxide catalyst was able to deliver almost identical ORR potentials to that of Pt-Ru [183]. The deposited Mn oxide was then assembled into a Zn-air battery utilizing a tri-electrode set up. The electrodeposited Mn oxide was used as the ORR catalyst and Co-Fe was used as the OER catalyst. The third electrode was Zn foil. With the ORR and OER catalysts separated, the battery was able to achieve an average efficiency of 58% after 50 h of cycling at an applied current density of 10 mA cm^{-2} , similar to that of Pt-Ru/C [183].

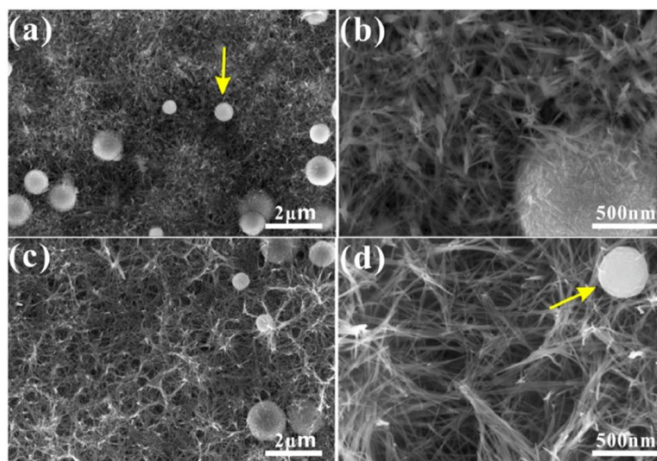


Figure 2-25 SEM SE images of a) and b) unannealed Mn oxide, c) and d) annealed Mn oxide deposits, with the arrow indicating the $\alpha\text{-Mn}_2\text{O}_3$ spheres [183].

2.7 Summary

In this chapter, the literature regarding zinc-ion batteries (ZIBs) was reviewed. An overview of ZIB technology and its components was presented. Several electrolytes that have been used for ZIBs have been covered, as well materials used for the anode. An in-depth analysis of numerous materials used for the cathode of ZIBs, along with their limitations, were discussed. Several different cathode material synthesis and fabrication methods were compared. Electrodeposition was found to be a good technique for the rapid and inexpensive preparation of diverse cathode materials for ZIBs. Various material characterization and electrochemical characterization techniques were summarized. To summarize, the following aspects need to be addressed for the further development of ZIBs:

- 1) The material used for the ZIB cathode should be synthesized using a cost-effective, repeatable and simple method.
- 2) The cathode material should possess a large capacity with stable performance during cycling for an extended period of time.
- 3) The reaction mechanisms associated with discharging and charging at the cathode need to be elucidated.

Chapter 3: Electrodeposited Manganese Oxide on Stainless Steel for Zinc-ion Battery Cathodes

3.1 Introduction

Zinc-ion battery (ZIB) development is a relatively new area of research in the literature and began to garner attention in 2012 through the work of Xu et al. [14]. Since then, there has been a surge in the number of publications in the field. Mn oxide materials are the most commonly studied materials for use as cathodes in ZIBs. This is due to Mn oxide being inexpensive, abundant, environmentally benign, and possessing a high theoretical capacity [2], [15]. However, Mn oxide materials have generally shown poor capacities, cyclability, or a combination of both [7], [8].

Typically, a hydrothermal method is used to produce Mn oxide materials for the cathode. Once produced, the Mn oxide is mixed with a conductive carbon material and a binding material to make a slurry. The slurry is then cast onto a conductive substrate, with stainless steel (SS) foil or mesh commonly used along with Ti foil or mesh [2]. Other substrates include carbon based substrates, such as carbon cloth [2]. However, the entire fabrication process can take well over 24 h to produce a single sample and the application may not be uniform and consistent. On the other hand, electrodeposition is a fast, simple, and inexpensive technique that can deposit a wide variety of materials very quickly. This allows for a short turnaround time between sample preparation and testing. Additionally, electrodeposition does not require the use of additive materials, allowing for intimate contact with the substrate.

The Ivey research group has extensive experience with the electrodeposition and characterization of Mn oxide materials for supercapacitor and Zn-air battery applications. However, Mn oxide had not been previously used for ZIB applications in the Ivey research group. Therefore, this study was exploratory in nature with the goal of using previously developed Mn oxide electrodeposition techniques to fabricate cathodes for ZIBs. Another goal of this work was to produce a battery with similar results to those found in the literature as a proof of concept. In this study, Mn oxide was deposited onto stainless steel (SS) using two different electrodeposition techniques previously developed in the Ivey research group for supercapacitor and Zn-air battery applications. The first method used was an anodic Mn oxide electrodeposition developed for

supercapacitor applications. The second method was a pulsed anodic electrodeposition technique developed for Zn-air battery applications. Deposits obtained using the first deposition technique were characterized using SEM and EDS analysis, with some electrochemical characterization. The approach was not pursued further due to poor electrochemical performance. Deposits from the second deposition technique were also examined using a number of materials characterization techniques. Deposits were identified as Mn_3O_4 and are hereafter referred to as such. The Mn_3O_4 -based cathode showed improved electrochemical performance compared with deposits using the first deposition method. However, the cathode still suffered from severe capacity loss upon cycling.

3.2 Experimental

3.2.1 Material Synthesis and Electrode Preparation

All electrodepositions were performed on 304 SS coins with a surface area of 2 cm^2 . The coins were initially cleaned in acetone and ethanol for 10 min each in an ultrasonic bath (Branson 2510, 40 kHz). The SS was then cleaned and activated following a modified method presented in ASTM B254 [184]. In summary, the SS coins were cleaned and activated using a cathodic method with an applied current of 43 mA for 5 min. An electrolyte of 0.5 M HCl solution was used along with Pt mesh as the counter electrode.

Two different electrodeposition techniques were used to deposit Mn oxide materials onto SS substrates. The first technique used was similar to that reported by Clark et al. to fabricate electrodes for supercapacitor applications [180]. Mn oxide was electrodeposited using anodic deposition with an applied current density of 20 mA cm^{-2} at 60°C for 5 min onto SS coins. A solution of 0.01 M $\text{Mn}(\text{CH}_3\text{COO})_2$, 0.02 M $\text{NH}_4(\text{CH}_3\text{COO})$ and 10% $\text{C}_2\text{H}_6\text{OS}$ (dimethyl sulfoxide, DMSO), containing a stir bar rotating at 80 rpm, was used as the electrolyte. The SS coin was the working electrode and Pt mesh was used as the counter electrode. After deposition, the material was washed with deionized water and dried in air at 100°C for 60 min. This type of deposition is referred to as deposition 1.

The second technique was similar to that reported by Xiong et al. to produce the air electrode for Zn-air batteries [183]. Essentially, Mn_3O_4 was electrodeposited using a pulsed anodic

technique with an applied current of 1.17 mA cm^{-2} . A 0.25 s ON cycle and a 0.5 s OFF cycle were used for total of 2400 cycles. The SS coin and Pt mesh were the working and counter electrodes, respectively. The electrolyte solution consisted of 0.02 M of $\text{Mn}(\text{CH}_3\text{COO})_2$, 100 mg L^{-1} of sodium dodecyl sulfide (SDS), and 0.02 M of NaCH_3COO . During deposition, the cell was placed in an ultrasonic bath (Branson 2510, 40 kHz). Upon completion of the deposition, the material was rinsed with deionized water and annealed for 30 min at 300°C . Samples typically had a mass loading of $0.2 - 0.3 \text{ mg cm}^{-2}$. This type of deposition is referred to as deposition 2.

3.2.2 Material Characterization

Scanning electron microscopy (Tescan Vega3 SEM, operated at 20 kV) and energy dispersive X-ray spectroscopy (EDS) were used to characterize the microstructure and composition of the fabricated samples. Samples for SEM were prepared by attaching the Mn oxide samples to Al stubs using double sided Cu tape. Transmission/scanning transmission electron microscopy (JEOL JEM-ARM200CF TEM/STEM, operated at 200 kV) and EDS mapping were also used to examine the microstructure and composition of the sample at higher magnifications, as well as to generate crystal structure information. TEM samples were prepared by scraping the deposited Mn oxide from the SS and dispersing the powder in 1 mL of ethanol, while agitating in an ultrasonic bath. One or two drops of the suspension were placed onto holey carbon coated grids using a pipette and then the ethanol was allowed to evaporate. X-ray diffraction (XRD) was also utilized to examine the crystal structure of the samples with a $\text{Cu K}\alpha$ ($\lambda = 0.154 \text{ nm}$) X-ray source (Rigaku Ultima IV). XRD data were collected either in powder mode or in thin film mode using an incident angle of 2° .

3.2.3 Electrochemical Measurements and Battery Testing

Electrochemical testing was completed using a Biologic SP-300 or VSP-350 potentiostat with five port electrochemical cells (AKCELL1, Pine Instruments) and CR 2032-coin cells. Cyclic voltammetry (CV) tests were done using the five port electrochemical cells. For both types of depositions, Ag/AgCl in 3.5 M KCl was used as the reference electrode and Zn foil as the counter electrode. The working electrode was either the cathode fabricated using deposition 1 or deposition

2. An electrolyte solution of 1 M ZnSO₄ + 0.1 M MnSO₄ was utilized for electrochemical testing of samples from both deposition 1 and deposition 2. A scan rate of 0.5 mV s⁻¹ was employed for CV testing with a potential range of 1.0 V to 1.8 V vs Zn/Zn²⁺.

Galvanostatic charge and discharge (GCD) testing was done using samples from deposition 2 but not for samples from deposition 1. The coin cells were used for GCD testing and were assembled using the fabricated cathode as the working electrode, Zn foil as the counter electrode, and a glass fiber separator. Filter paper was used as the separator for the assembled coin cells. GCD tests were conducted between 1.0 and 1.8 V vs Zn/Zn²⁺. The electrolyte was 2M ZnSO₄ + 0.2 M MnSO₄. Applied specific currents of 50 mA g⁻¹ and 300 mA g⁻¹ were used for GCD testing. The initial or conditioning cycle was done at a low specific current of 50 mA g⁻¹ to condition or prime the battery before testing, since the first GCD cycle is different from the subsequent cycles. A specific current of 300 mA g⁻¹ was selected for subsequent cycling based on the specific currents used for testing in the literature. The applied current densities were normalized to the mass of the active material on the electrode. All tests were performed at room temperature and were IR-corrected.

3.3 Results and Discussion

Two different electrochemical deposition methods were used to deposit Mn oxide on SS. Each deposition is discussed separately. As mentioned previously, the first type of deposition is referred to as deposition 1 and the second type as deposition 2.

3.3.1 Deposition 1

3.3.1.1 Materials Characterization

The SEM images presented in Figure 3-1 show the as deposited Mn oxide on SS using deposition 1. The Mn oxide form as rods that possess a flake-like structure, similar to that reported by Clark et al. [180]. The rod and flake morphology provide a large surface area for the cathode. EDS spectra obtained from the bare SS substrate and the deposited Mn oxide on SS are also presented in Figure 3-1. The Fe K_α and Cr K_β peaks overlap with the Mn K_β and K_α peaks,

respectively, making it difficult to determine how much of the peak intensity is actually from the deposited Mn. Additionally, the bare SS also contains a small amount of Mn. However, when comparing the two spectra, the Cr K_{β} peak for the Mn oxide on SS spectrum is more intense compared with the same peak for the bare SS, indicating that Mn is deposited on the substrate as Mn oxide.

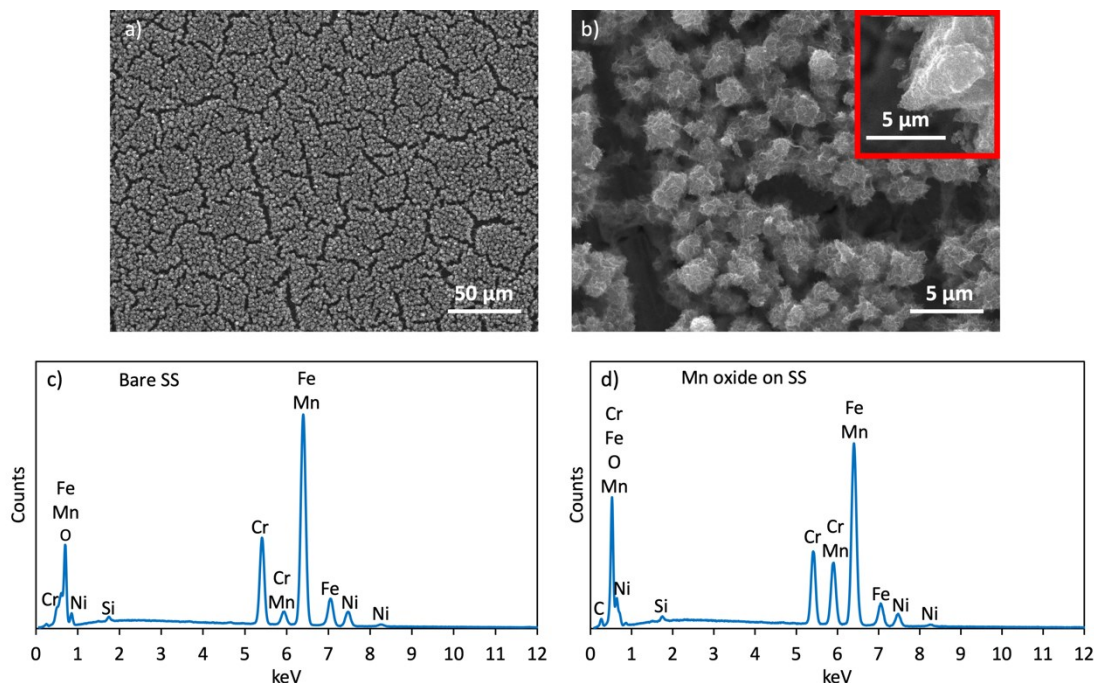


Figure 3-1 SEM secondary electron (SE) images and EDS spectra: a) and b) low and high magnification images of the deposited Mn oxide sample, c) EDS spectrum for the bare SS substrate, d) EDS spectra of the Mn oxide on the SS substrate.

3.3.1.2 Electrochemical Results

The Mn oxide on SS sample was assembled into a ZIB and underwent CV cycling (Figure 3-2). The initial cycle for the CV results is different from the subsequent cycles. This behavior is similar to that reported in the literature and may indicate a phase change occurring in the first cycle [40], [67], [68]. The initial cycle has one large oxidation peak with a small shoulder and two reduction peaks. The oxidation peak is located at 1.59 V with a shoulder at roughly 1.65 V and the reduction peaks are located at roughly 1.18 and 1.26 V. The subsequent cycles also show one pair

of peaks; however, they are positioned at different potentials. The reduction peaks are located at 1.29 V and the oxidation peaks at 1.63 V. From the literature, the pair of redox peaks in the subsequent cycles may indicate the intercalation of Zn [14], [47]. Furthermore, the peak current decreases significantly upon cycling, particularly the reduction current, which can indicate capacity loss on cycling [41]. The decrease in capacity in ZIBs has been attributed to Mn dissolution, material phase change, and increased internal stress from battery cycling [16], [54].

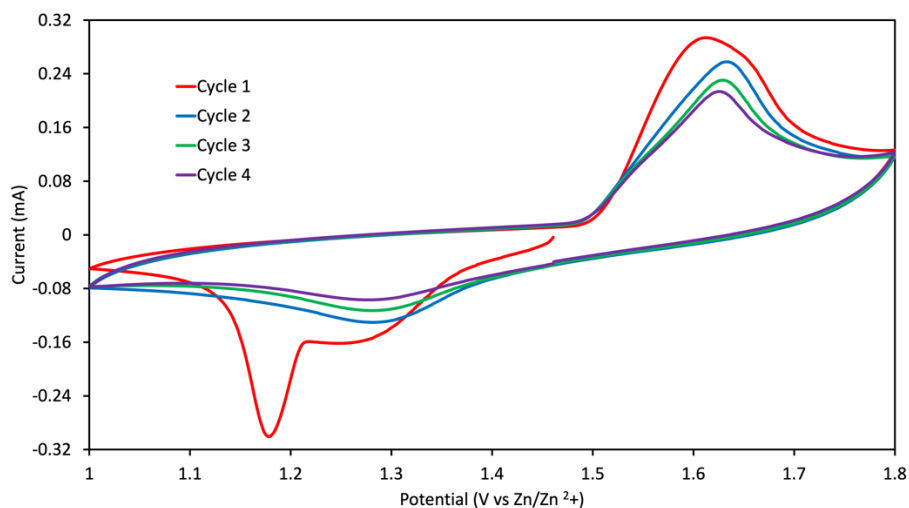


Figure 3-2 CV results for Mn oxide on SS cathode (deposition 1) in a ZIB. The legend indicates the cycle number and the corresponding colour.

When the ZIB was unassembled, the cathode showed a loss of material (Figure 3-3). Even with the acid activation step, the Mn oxide did not adhere very well to the SS and would stick to the separator material. Therefore, the decrease in the peak current during CV cycling is likely due to a combination of delamination of Mn oxide from the SS and dissolution of Mn during cycling. The shift in the potential peaks between the first cycle and the subsequent cycles may be due to an initial phase change of the Mn oxide material, which may also contribute to the poor cycling performance [40], [67].

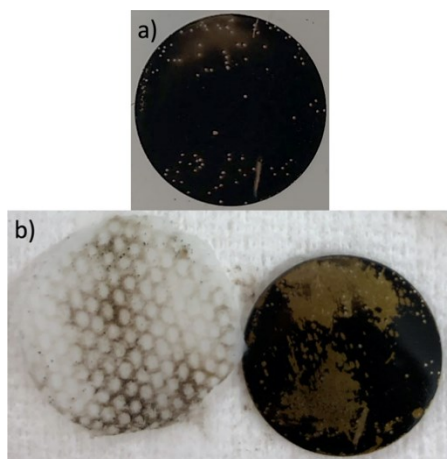


Figure 3-3 Photographs of Mn oxide on SS sample (deposition 1) a) before CV testing and b) after CV testing. The image on the left in (b) is the separator.

Further materials and electrochemical analysis were not done for deposition 1, as it was apparent from the CV testing and observed material loss that the fabricated cathode would not perform well when assembled into a ZIB.

3.3.2 Deposition 2

3.3.2.1 Materials Characterization

The SEM images presented in Figure 3-4 show the pristine as deposited Mn_3O_4 on SS. The oxide covers the entire surface of the SS and has a flake-like morphology, somewhat similar to what was reported by Xiong et al. [183]. EDS spectra for the bare SS and the deposited Mn_3O_4 are presented in Figure 3-4 as well. As with deposition 1, there is overlap between the Fe K_α and Cr K_β peaks and the Mn K_β and K_α peaks, respectively, but Mn has clearly been deposited.

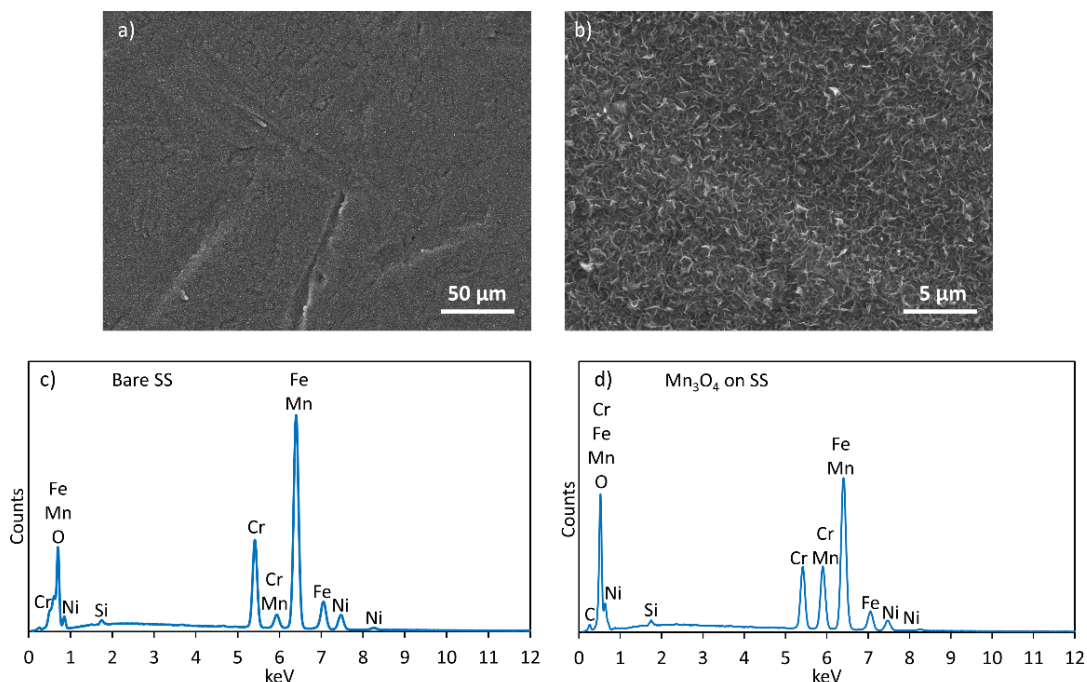


Figure 3-4 SEM SE images and EDS spectra: a) and b) low and high magnification images of the deposited Mn oxide sample, c) EDS spectrum for the bare SS substrate, d) EDS spectrum of Mn oxide on the SS substrate.

XRD analysis (powder mode) was done on the sample and the pattern is presented in Figure 3-5. The deposit peaks are fairly weak; the most intense and sharpest peak is from the SS. The weak intensities and broad nature of the deposit peaks are likely due to their nanocrystalline nature, high defect density, and limited amount of material available for analysis. However, the pattern can still be reasonably indexed to two different Mn oxide phases, cubic spinel Mn_3O_4 (PDF#00-013-0162) or tetragonal hausmannite Mn_3O_4 (PDF#01-071-6262). The hausmannite structure is the more thermodynamically stable of the two different phases [185]. The experimental pattern is also similar to an XRD pattern indexed to hausmannite in the literature [136].

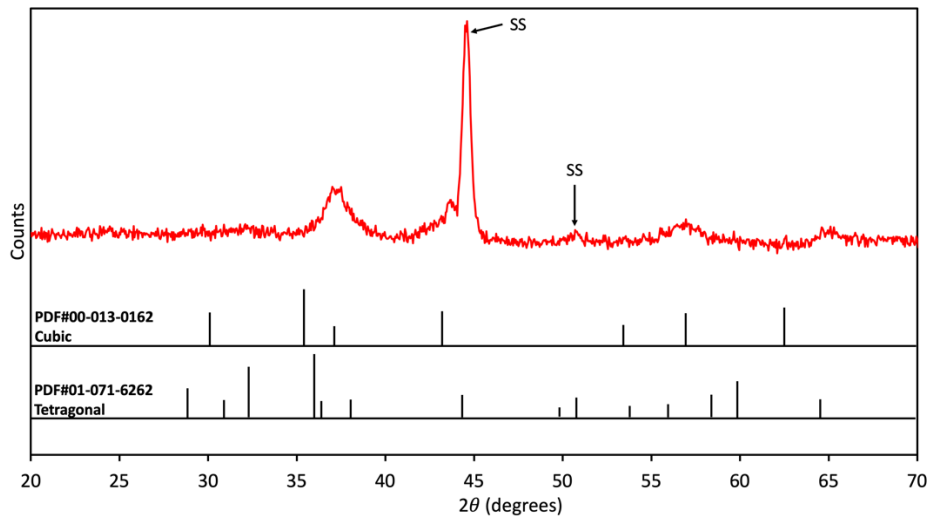


Figure 3-5 XRD pattern for Mn_3O_4 on SS. PDF cards for cubic spinel Mn_3O_4 (PDF#00-013-0162) and hausmannite Mn_3O_4 (PDF#01-071-6262) are superimposed on the pattern.

3.3.2.2 Electrochemical Results

The Mn_3O_4 cathode was assembled into a ZIB and underwent CV testing, with the results shown in Figure 3-6a. For the first scan, one reduction peak occurs at 1.11 V and two oxidation peaks occur at 1.50 V and 1.54 V, respectively. The reduction peak at 1.11 V decreases in intensity on subsequent cycling and the peak is shifted to a lower potential of 1.08 V. Also, with cycling, two reduction peaks are observed at roughly 1.17 V and 1.32 V during the cathodic scan. As with deposition 1, the peak currents for both oxidation and reduction decrease as the sample cycles. The reduction and oxidation peaks located at 1.17 V and 1.50 V, respectively, show a significant decrease in peak current. The other reduction and oxidation peaks located at 1.33 V and 1.54 V also decrease in intensity as the material is cycled. The reduction in the peak currents for both oxidation and reduction can indicate a reduction in battery performance and capacity. GCD test results are presented in Figure 3-6b. The initial cycle is referred to as the conditioning cycle and involved using an applied specific current of 50 mA g^{-1} to condition or prime the battery for cycling before testing, since the initial GCD cycle for the sample is different from the subsequent cycles. Subsequent cycling was completed using an applied specific current of 300 mA g^{-1} . The battery exhibited a high maximum discharge capacity of 317 mAh g^{-1} during the conditioning cycle. For the first cycle under an applied load of 300 mA g^{-1} , the battery exhibited a discharge capacity of

287 mAh g⁻¹. The conditioning cycle plateaus during GCD testing correspond with the current peaks in the initial CV scan. During battery cycling after the conditioning cycle, two discharge plateaus occur at about 1.36 V and 1.25 V, with the charge plateaus occurring at roughly 1.55 V and 1.60 V. The peak currents from CV testing also correspond very well with the GCD plateaus for the cycles after conditioning, with some variation due to the scan rate used for CV and the specific current applied for GCD. From the literature, the difference between the first and subsequent CV cycles and the conditioning and subsequent GCD cycles has been attributed to a phase change of the active material upon initial discharge [40], [67], [125]. Additionally, the two sets of CV peaks and the two charge and two discharge GCD plateaus suggest that a two-step reaction mechanism occurs on battery cycling. Furthermore, the battery capacity during GCD testing fades very quickly, which indicates poor cyclability. From the GCD plots, the second discharge plateau (1.25 V) and first charge plateau (1.55 V) fade very quickly compared with the first discharge plateau and second charge plateau. This is similar to what was observed in CV cycling; the reduction and oxidation peaks currents at 1.17 V and 1.50 V, respectively, decrease rapidly on cycling while the other redox peaks gradually decrease. After 35 GCD cycles, the assembled battery was able to achieve a capacity of 102 mAh g⁻¹, corresponding to a capacity retention of 35.5%.

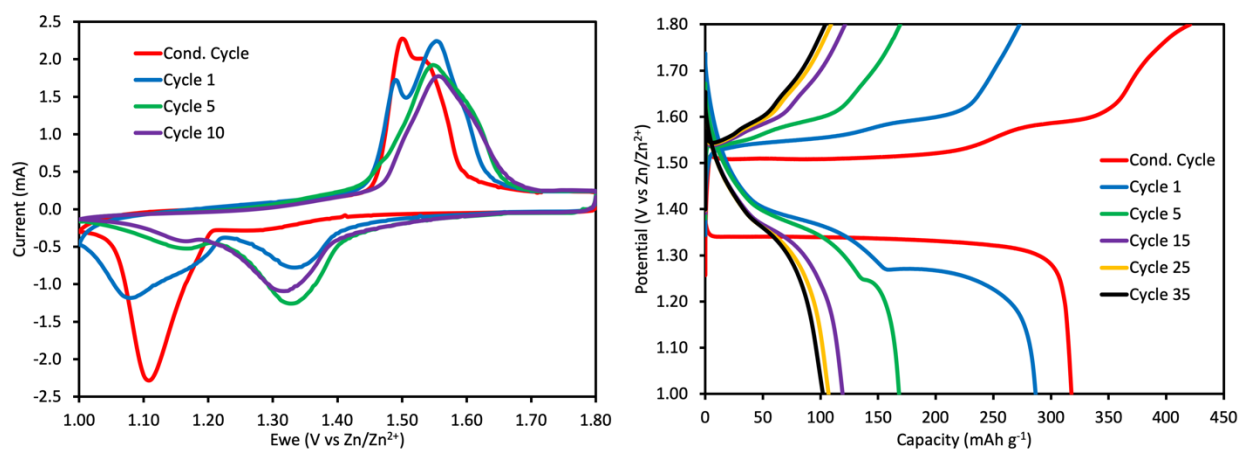


Figure 3-6 Electrochemical and battery performance of Mn_3O_4 on SS in an assembled ZIB: a) CV results at a scan rate of 2 mV s^{-1} and b) GCD test with the conditioning cycle completed at an applied specific current of 50 mA g^{-1} and the subsequent cycles at 300 mA g^{-1} .

3.3.2.3 Reaction Mechanism

Figure 3-7 shows SEM and STEM EDS images of the cathode after the conditioning cathodic (discharge) CV sweep. Figure 3-7a shows the CV curve for the full cycle; the test was stopped at 1.0 V after discharge and the ZIB was dismantled to allow for examination of the cathode (Figure 3-7b). Large plate-like structures are present over the entire surface of the cathode. These plate-like structures have a similar morphology to zinc sulfate hydroxide (ZSH, $\text{Zn}(\text{OH})_2\text{ZnSO}_4 \cdot x\text{H}_2\text{O}$) that has been observed in the literature [71], [143]. The STEM EDS mapping results (Figure 3-7d to Figure 3-7h) show that the plate-like structure does not contain any Mn, but is rich in Zn, S, as well as O, indicating the plates are indeed ZSH. It has been reported that the formation of ZSH is detrimental to the performance of ZIBs and could contribute to the poor cycling performance of the assembled ZIB [71].

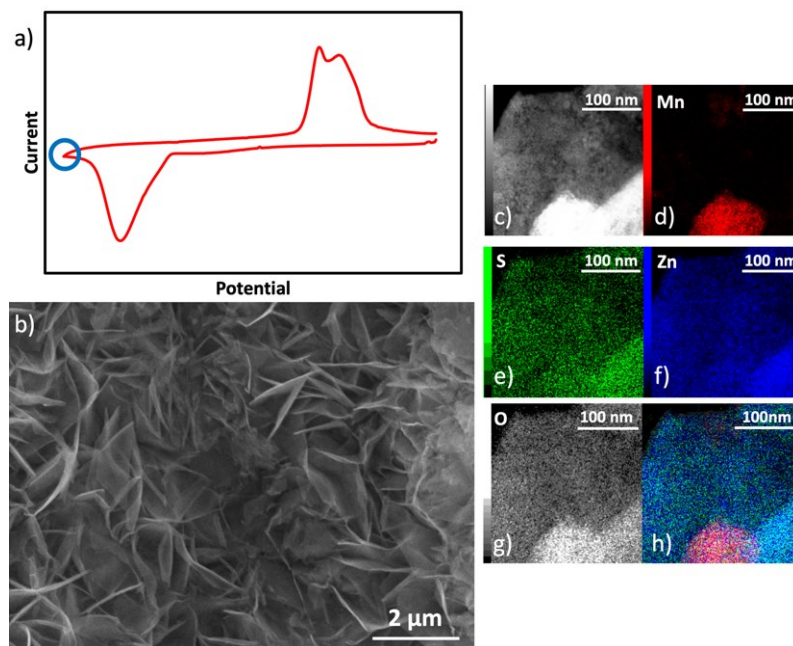


Figure 3-7 a) CV plot showing that the cathodic (discharge) scan was stopped at 1.0 V for analysis, b) SEM SE image showing plate-like formation on the cathode surface, c) STEM annular dark field (ADF) image, d)-g) STEM EDS maps corresponding to the ADF image, and g) STEM EDS map showing an overlay of Zn, Mn, and S data.

Figure 3-8 shows SEM and STEM EDS images of the cathode after the conditioning anodic (charge) CV sweep. Figure 3-8a shows that the CV test was stopped at 1.80 V and then the ZIB was taken apart to examine the cathode. The SEM image (Figure 3-8b) of the charged sample shows that the plate-like structure has disappeared. However, the morphology of the cathode surface does not appear to be flake-like anymore, differing from the pristine sample. STEM EDS maps (Figure 3-8d to Figure 3-8g) show that Zn is not completely removed from the sample. Additionally, a very small amount of S is still present. However, it should be noted that the detected S in the sample may arise from the SDS used during electrodeposition. Combining the SEM and STEM EDS analysis with the CV and GCD results, the remaining Zn may be due to a phase change that occurs during the conditioning discharge. In the literature, it is suggested that Mn oxide materials transform to ZnMn_2O_4 spinel structures after the first discharge, with the ZnMn_2O_4 spinel structure providing the electrochemical performance for the subsequent cycles [67]. The poor cycling performance of the sample can be attributed to a combination of several factors; the formation of ZSH all over the surface of the cathode, the suggested initial phase transformation, and the battery cycling [40], [42], [45], [56], [71]. Based on the analysis here, a definitive discharge/charge mechanism for the Mn_3O_4 on SS cathode could not be determined. The reaction mechanism could be any of the proposed reaction mechanisms for Mn oxide materials in the literature: Zn^{2+} and H^+ intercalation, a conversion reaction, and/or a combination of intercalation and conversion [17], [31], [67], [71]. Phase changes and the formation of ZSH have been reported to occur for all reaction mechanisms involving Mn oxide materials. Due to the poor electrochemical performance of the cathode when assembled into a ZIB, further electrochemical and materials characterization testing were not conducted.

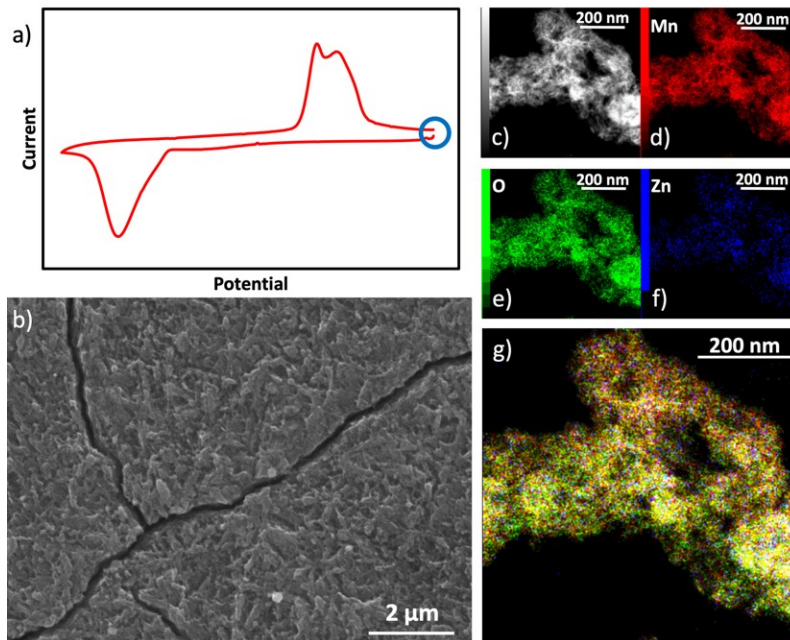


Figure 3-8 a) CV plot showing that the anodic (charge) scan was stopped at 1.8 V for analysis, b) SEM SE image showing the cathode after the first charge cycle is completed, c) STEM ADF image, d)-g) STEM EDS maps corresponding to the ADF image, g) STEM EDS map showing an overlay of Zn, Mn, and S data.

3.4 Summary

Electrodeposition offers many advantages compared with other material production methods, including the elimination of binders, room temperature synthesis, and short fabrication times. Manganese oxide was electrodeposited onto stainless steel (SS) substrates, using two previously developed methods in the Ivey research group, for use as cathode in zinc-ion batteries (ZIBs). The first method was a direct anodic electrodeposition technique. The method deposited Mn oxide as rods perpendicular to the substrate surface, with the rods having a flake-like structure. Through cyclic voltammetry (CV) testing it was revealed that the cathode material showed decreasing current peaks on cycling, indicating poor capacity retention. Combining CV and visual inspection, it was determined that the Mn oxide experienced Mn dissolution and did not adhere well to the SS substrate. The second process used was a pulsed anodic electrodeposition technique. The technique produced Mn oxide on SS with a flake-like morphology. Through X-ray diffraction (XRD) analysis, the material was determined to be Mn_3O_4 spinel. The fabricated electrode exhibited an excellent initial capacity of 287 mAh g^{-1} . However, after 35 cycles, the cathode was only able to

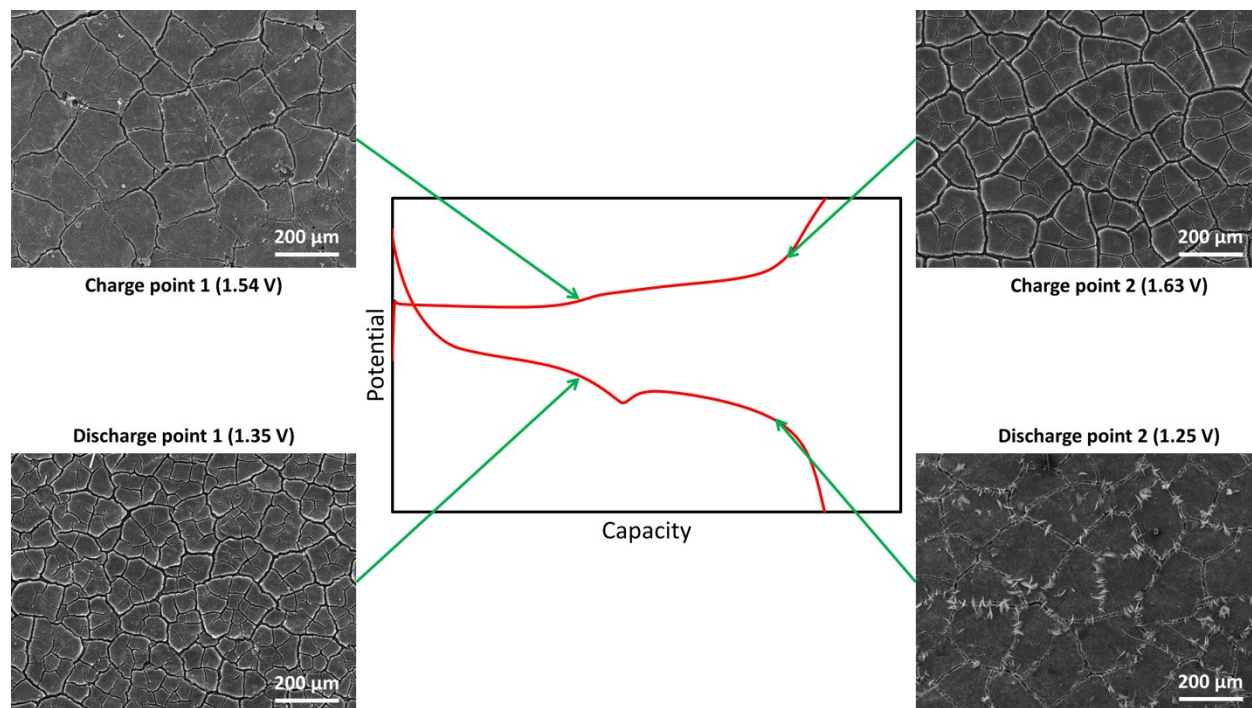
maintain a capacity of 102 mAh g^{-1} , corresponding to a capacity retention of 35.5%. Through a combination of microstructural and electrochemical analysis, the poor performance of the battery was attributed to an initial phase change of the cathode material, and the formation of ZSH all over the cathode surface. Based on the electrochemical results, the Mn_3O_4 undergoes a two-step reaction mechanism; however, an exact mechanism for the cathode could not be confidently proposed.

Chapter 4: Electrodeposited Manganese Oxide on Carbon Paper for Zinc-ion Battery Cathodes

A version of this chapter has been accepted for publication in Batteries & Supercaps:

A. Dhiman, D. G. Ivey, Electrodeposited Manganese Oxide on Carbon Paper for Zinc-ion Battery Cathodes, Batteries & Supercaps, 2019, 2, DOI: 10.1002/batt.201900150

Graphical Abstract



Nano-crystalline, flake-like manganese oxide was electrodeposited onto carbon paper using a pulsed electrodeposition technique. Results indicate good capacity, rate capability, cyclability, and suggest a two-step reaction mechanism. Electrodeposition is a simple and quick method for producing high performing electrodes without the use of additives and binders.

4.1 Introduction

While Li-ion batteries (LIBs) dominate the battery market from portable electronics to vehicles, they face several challenges that limit their future application, such as limited resources for battery materials, cost, and safety concerns [2], [9]. In the literature, there has been increased interest recently in Zn-ion batteries (ZIBs) as a replacement for LIBs. This is largely attributed to the low cost, abundance, high theoretical capacity (820 mAh g^{-1}), compatibility with aqueous and non-aqueous electrolytes, and the low environmental impact of Zn [2], [7]. However, ZIBs face several challenges that have restricted their implementation as an alternative to LIBs. In general, ZIB cathode materials have limited capacities, poor capacity retention, poor rate capabilities, limited potential windows, low operating potentials, or a combination of the aforementioned issues [2], [16], [31].

Presently, several different categories of materials have been explored for use as cathodes, with the most popular ones being V oxide compounds [16], [31], [37], [38], [87], [88], [90], [140], [141], [186], [187], Prussian blue analogues (PBA) [16], [31], [34], [46], [48], [121], and Mn oxide compounds [14], [16], [21], [31]–[33], [39], [40], [42], [53]–[55], [66], [136], [148], [158], [159], [177], [188]. To a lesser extent, sustainable quinone analogs, metal sulfides, Chevrel phase compounds, and polyanion based compounds have also been explored [16], [31], [67]. Of the different materials explored for ZIB cathodes, the most commonly studied material is Mn oxide. This is in large part due to Mn oxide's large theoretical capacity, non-toxicity, abundance, numerous stable valence states, and low cost [31], [67]. Of the different Mn oxide phases that have been studied, there have only been a handful of instances where Mn_3O_4 has been used as a cathode material for ZIBs [32], [33], [42], [66], [136], [177]. Mn_3O_4 has been extensively studied for Zn-air batteries and has been shown to be a good oxygen reduction reaction (ORR) catalyst for the air electrode in Zn-air batteries [183], [189].

Currently, there are still many issues associated with the use of Mn_3O_4 as an electrode for ZIBs that must be addressed if ZIBs are to become a widely accepted technology. Like other Mn oxide compounds, Mn_3O_4 experiences severe capacity fade, poor rate capabilities, low capacities, or a combination of these. These issues have generally been associated with cathode material phase change upon cycling, Mn dissolution, poor Mn oxide conductivity, or the formation of reaction side products [32], [42], [136]. Dissolution of Mn is generally addressed by the addition of Mn

into the electrolyte, while poor conductivity is minimized by the use of carbon additives or conductive substrates [21], [32], [67], [136], [177]. Recently, Fang et al. have shown that the incorporation of K into the cathode can also help suppress Mn dissolution [190]. Reducing particle size and increasing surface area of the active material has also been employed to address the poor conductivity of Mn oxides [159]. Furthermore, the reaction mechanism surrounding Mn_3O_4 materials, and Mn oxide compounds in general, is still not completely understood. In the literature, many groups have argued that Mn oxide materials undergo Zn^{2+} intercalation during battery cycling, with both discharge plateaus corresponding to Zn^{2+} insertion into different sites within the cathode structure [28], [73], [157]. However, other groups contend that Mn oxides undergo a chemical conversion reaction [21]. There have also been reports of a co-intercalation process, where H^+ insertion occurs in the first plateau followed by Zn^{2+} insertion during the second plateau [39], [191]. More recently, Chao et al. have proposed a fourth mechanism involving the deposition and dissolution of MnO_2 for ZIBs [192]. Their battery uses an electrolyte consisting of H_2SO_4 , ZnSO_4 , and MnSO_4 . Zinc in the battery undergoes a plating and stripping reaction at the anode, but Zn is not directly involved in the cathode processes. Regarding Mn_3O_4 in particular, Hao et al. have suggested that Mn_3O_4 undergoes a co-intercalation mechanism during discharge with H^+ insertion followed by Zn^{2+} insertion [42]. They also mention that zinc sulfate hydroxide (ZSH or $\text{Zn}_4(\text{OH})_6(\text{SO}_4) \cdot x\text{H}_2\text{O}$) and manganese oxyhydroxide (MnOOH) form during battery discharge but are dissolved on recharge. Additionally, during the initial charge, Hao et al. propose that Mn_3O_4 is converted to Mn_5O_8 and birnessite ($\delta\text{-MnO}_2$) with no Zn^{2+} involved in this process. On the other hand, Zhu et al. propose that Mn_3O_4 undergoes a chemical conversion reaction with Mn_3O_4 transforming to MnO on discharge, accompanied by the formation of large plate-like ZSH [136]. During recharge, ZSH is dissolved and MnO is converted back to Mn_3O_4 . ZnMn_2O_4 is another spinel structure that has been explored for ZIBs. Zhang et al. and Wu et al. have both proposed that ZnMn_2O_4 undergoes Zn^{2+} intercalation/deintercalation reactions for discharge and charge, without any phase transformation or formation of any side products [32], [33]. Yang et al. used a combined ZnMn_2O_4 and Mn_2O_3 cathode and also proposed that the material only underwent Zn^{2+} intercalation during cycling [66]. However, Chen et al. have reported that the formation of ZSH accompanies Zn intercalation during ZnMn_2O_4 cycling [177].

Hydrothermal methods are commonly used to fabricate the cathode material. This involves keeping the reactants at elevated temperatures and pressures in an autoclave for several hours [32],

[136]. The produced cathode material is ground and combined with carbon black and a binder to create a slurry that is cast onto a substrate. The electrode is then heated for several hours for drying, followed by a sintering step before it is ready for use [33], [66]. The entire fabrication process can easily take more than 24 h to generate a sample. The use of a slurry method to apply the produced material to the substrate can result in significant variations in mass loading from sample to sample [21]. Solution precipitation methods, in combination with the slurry method, can also take a similar length of time to prepare the active material and electrodes for ZIBs [42]. Electrodeposition is a fast, simple, and inexpensive one-step technique that can deposit a wide variety of materials. This technique works by depositing solvated ionic species onto a conductive substrate by applying an external potential or current [109]. The simplicity of electrodeposition allows for fast turnaround for material deposition and testing, which is beneficial when considering scalability. Additionally, electrodeposition is easily reproducible resulting in highly consistent deposits. With electrodeposition, the active cathode materials for ZIBs can be directly deposited onto an electrode substrate at room temperature without the requirement of binders and lengthy fabrication times. Electrodeposition has been utilized previously in the literature to fabricate Mn oxide cathode materials for ZIBs [39], [68], [71]. Sun et al. used a potentiostatic method to deposit MnO_2 onto carbon fiber paper (CFP), which was then employed in a battery with an electrolyte consisting of 2 M ZnSO_4 and 0.2 M MnSO_4 [39]. Li et al. utilized a galvanostatic method to deposit MnO_2 onto carbon electrodes with a battery electrolyte composed of 1 M ZnSO_4 and 0.2 M MnSO_4 [71]

In this study Mn oxide is electrochemically deposited onto carbon paper (CP) via a pulsed electrodeposition technique for use as a cathode for ZIBs. The deposited oxide is identified through a number of microstructural characterization techniques as Mn_3O_4 . As such the oxide is hereafter referred to as Mn_3O_4 . Electrode fabrication can be done in ~ 1 h and does not require the use of binders. The process should also be easily scalable to produce ZIB cathode materials. The Mn_3O_4 -based cathode demonstrates good rate capability and cycling performance during ZIB testing. Furthermore, insight into the reaction mechanisms associated with discharging and charging of Mn_3O_4 -based materials is provided.

4.2 Experimental

4.2.1 Material Synthesis and Electrode Preparation

The electrodeposition technique used is similar to that reported by Xiong et al. to fabricate air electrodes for Zn-air batteries [183]. To summarize, anodic pulsed electrodeposition was employed at an applied current of 4.7 mA with a 0.25 s ON cycle and a 0.5 s OFF cycle, for a total of 2400 cycles. The electrolyte solution consisted of 0.02 M of $\text{Mn}(\text{CH}_3\text{COO})_2$, 100 mg L^{-1} of sodium dodecyl sulfide (SDS), and 0.02 M of NaCH_3COO . Flexible carbon paper (CP, Freudenberg H23C6) and Pt mesh were used as the working electrode and counter electrode, respectively. The nominal deposition area was 4 cm^2 . During the deposition process, the electrodeposition cell was placed in an ultrasonic bath (Branson 2510, 40 kHz) to agitate the solution. Once the Mn oxide was deposited onto the CP, the material was rinsed with deionized water and then annealed for 30 min at 300°C to help increase the oxidation state of the material and improve the crystallinity. The mass loading of the Mn_3O_4 was $\sim 0.3\text{-}0.4$ mg cm^{-2} on the CP substrate.

4.2.2 Material Characterization

Scanning electron microscopy (Tescan Vega3 SEM, operated at 20 kV) and energy dispersive X-ray spectroscopy (EDS) were used to characterize the microstructure and composition of the fabricated samples. Samples for SEM were prepared by mounting the cathode to Al stubs using carbon tape. Transmission/scanning transmission electron microscopy (JEOL JEM-ARM200CF TEM/STEM, operated at 200 kV) and EDS mapping were also used to examine the microstructure and composition of the sample at higher magnifications, as well as to generate crystal structure information. TEM samples were prepared by scraping the deposited Mn_3O_4 from the CP and dispersing the powder in 1 mL of ethanol, while agitating in an ultrasonic bath. One or two drops of the suspension were placed onto holey carbon coated grids using a pipette and then the ethanol was allowed to evaporate. Oxidation states of the components in the samples were examined using X-ray photoelectron spectroscopy (XPS), which was conducted using a monochromatic Al- K_α X-ray source with a pass energy of 20 eV (Kratos AXIS Supra XPS Instrument). The collected XPS spectra were calibrated using the C 1s peak at 284.8 eV and

analyzed using Casa XPS software. X-ray diffraction (XRD) was also utilized to examine the crystal structure of the samples with a Co K_{α} ($\lambda = 0.179$ nm) X-ray source (Rigaku Ultima IV). The patterns were collected in powder mode and converted to a Cu source using JADE 9.6 software for easy comparison with PDF cards. Raman scattering spectroscopy (Thermo DXR2 Raman microscope) was used to help in identifying the type of metal oxide deposited. The spectrum was obtained between 100 and 1000 cm^{-1} at room temperature using an excitation energy of 532 nm^{-1} . Each Raman spectrum collected was an average of 20 scans to help improve the signal to noise ratio.

4.2.3 Electrochemical Measurements and Battery Testing

Electrochemical testing was done using a Biologic SP-300 potentiostat with CR 2032-coin cells. The coin cells were assembled using Mn_3O_4 on CP as the working electrode, Zn foil as the counter electrode, and a glass fiber separator. A solution of 2 M ZnSO_4 + 0.2 M MnSO_4 was used as the electrolyte. Cyclic voltammetry (CV) and galvanostatic charge and discharge (GCD) tests were conducted in a potential window between 1.0 and 1.8 V. A scan rate of 0.1 mV s^{-1} was applied for CV testing. Several different applied specific currents were used for GCD testing, ranging from 300 mA g^{-1} to 2.4 A g^{-1} . The applied current densities were normalized to the mass of Mn_3O_4 on the electrode. All tests were conducted at room temperature and were IR-corrected. Zn/Zn^{2+} was used as the reference electrode for all electrochemical testing.

4.3 Results and Discussion

4.3.1 Material Characterization Results

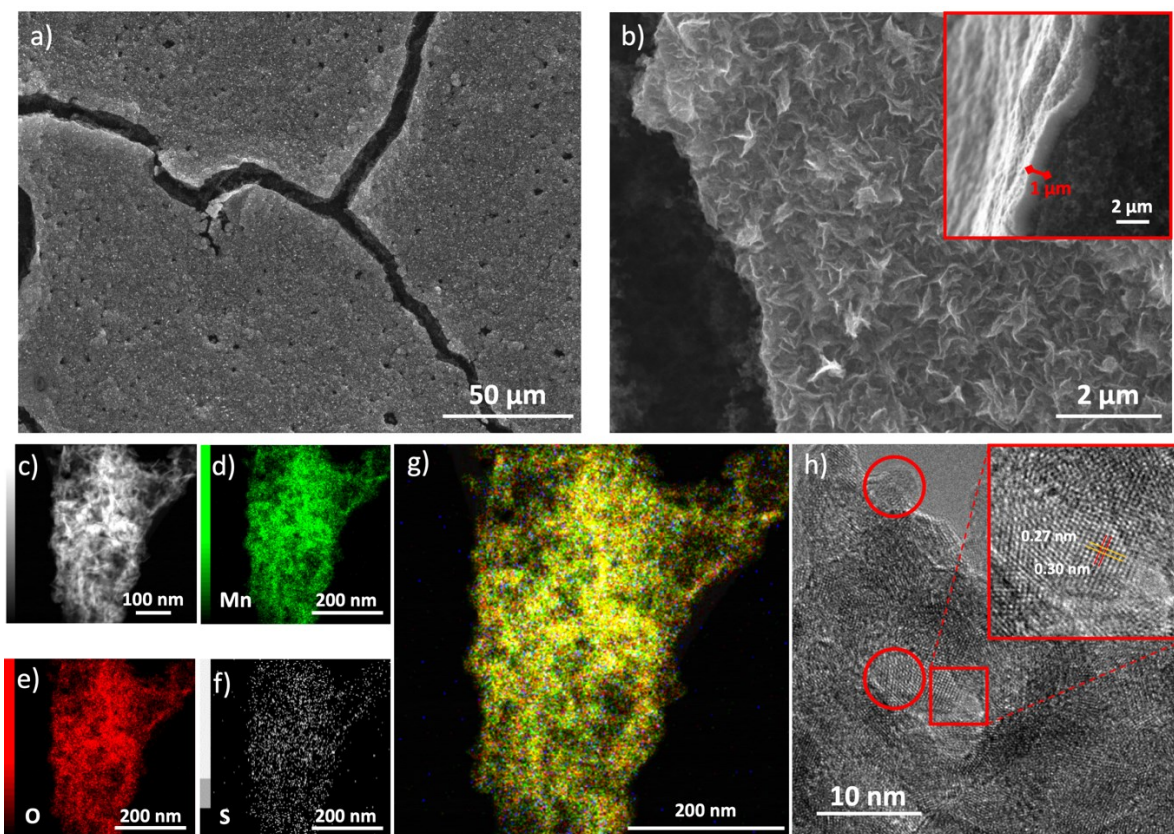


Figure 4-1 Electron microscopy analysis of as deposited Mn_3O_4 on CP: a) and b) SEM secondary electron (SE) images showing island formation and flake-like morphology of Mn_3O_4 . The inset image in b) shows a cross section image of the deposit; c) STEM annular dark field (ADF) image of Mn_3O_4 ; d)-f) EDX maps for Mn, O, and S in the deposit; g) overlain EDX maps (Mn, O, and S) for Mn_3O_4 deposit showing uniform distribution of Mn and O; h) High resolution TEM image depicting nanocrystalline nature of the deposited Mn_3O_4 with circles indicating individual particles. The inset image shows the lattice fringes and determined d-spacing

The SEM images presented in Figure 4-1a and Figure 4-1b show the pristine as deposited Mn_3O_4 on CP. Mn_3O_4 forms islands on the CP and the islands have a flake-like morphology. This flake-like morphology provides a high surface area for exposure to the electrolyte. Additionally, from the higher magnification inset SEM image (Figure 4-1b) it is determined that the Mn_3O_4 islands have a thickness of $\sim 1-2 \mu m$. A high surface area coupled with a thin deposit can improve ZIB performance by reducing the distance electrons need to travel, thus counteracting the

relatively poor conductivity of Mn oxides. STEM EDS mapping confirms that the deposit mainly consists of Mn and O (Figure 4-1d to Figure 4-1g). A small amount of S is also present, which is from the SDS used as an additive in the electrodeposition solution. The STEM EDS maps also show that there is a small amount of S in the as deposited sample. The S is likely from the SDS present in the electrodeposition solution. The high resolution TEM image (Figure 4-1h) shows that the deposited Mn_3O_4 oxide is nanocrystalline in nature with grains measuring approximately 5 nm in size. The inset image in Figure 4-1h shows a magnified view of the region indicated. Lattice spacings of 0.27 nm and 0.30 nm correspond to the (220) and (113) planes, respectively, of cubic Mn_3O_4 ; however, they could correlate with the (200) and (013) planes of tetragonal Mn_3O_4 (hausmannite) as well.

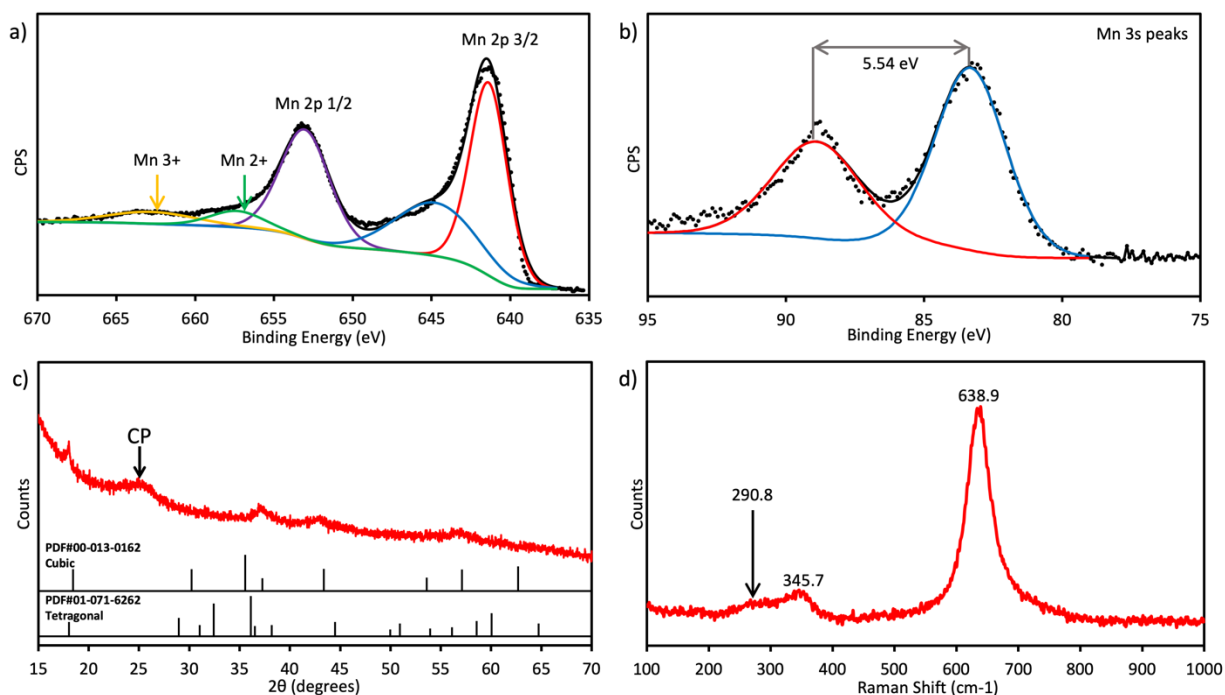


Figure 4-2 Characterization of as deposited Mn_3O_4 : a) Mn 3s XPS spectrum showing the peak splitting used for oxidation state determination, b) Mn 2p XPS spectrum showing two satellite peaks (labeled Mn 3^+ and Mn 2^+) used for oxidation state determination, c) XRD pattern and PDF cards for cubic Mn_3O_4 (PDF#00-013-0162) and hausmannite Mn_3O_4 (PDF#01-071-6262); the CP peak has been labelled as well, d) Raman spectrum with three peaks labeled.

XPS analysis was carried out to ascertain the oxidation state of the Mn in the Mn oxide deposit. A summary of the XPS analysis for the deposited Mn₃O₄ is given in

Table 4-1, along with comparisons with other Mn oxides. Using the area of the Mn 2p satellite features (Figure 4-2a), the average oxidation state of the deposited material was determined to be roughly 2.55, which is close to that of Mn₃O₄ (2.67) [181], [193]. Furthermore, the Mn 3s peak splitting (Figure 4-2b) was determined to be 5.54 eV, which is very similar to the 5.50 eV Mn 3s peak splitting expected for Mn₃O₄[181], [193]. In addition, the difference between the Mn 2p 3/2 and O 1s peak energies also suggests that the deposit could be Mn₃O₄ [193]. Finally, the survey scan for the deposit (Figure S4-1) was used to estimate the relative atomic amounts of the detected elements, giving ~45 at% Mn and 55 at% O, which are close to the composition corresponding to Mn₃O₄.

An XRD pattern of the deposited Mn oxide is presented in Figure 4-2c. The pattern was obtained by scraping off the deposit from the CP and placing the powder on a zero-background plate. The pattern is not well defined, with weak and broad peaks due to the nanocrystalline nature of the Mn oxide and the limited amount of sample powder. The pattern can be indexed reasonably well to two different Mn₃O₄ phases, either cubic spinel Mn₃O₄ (PDF#00-013-0162) or tetragonal hausmannite (PDF#01-071-6262). Hausmannite is the thermodynamically stable form of Mn₃O₄. Additionally, the XRD pattern is similar to the pattern obtained by Zhu et al., who indexed their pattern to hausmannite Mn₃O₄ [136]. The broad peak at ~25-26 degrees is from the CP substrate.

Raman spectroscopy data was collected for the deposited Mn₃O₄ and is presented in Figure 4-2d. The spectrum shows one distinct peak at 638.9 cm⁻¹ and a smaller peak at 345.7 cm⁻¹. There may be an additional peak located at 290.8 cm⁻¹. This pattern most closely fits with patterns observed for Mn₃O₄ (Figure S4-2), further suggesting that the deposit is a Mn₃O₄ [183], [194], [195]. Therefore, based on the combined XRD, XPS, and Raman spectroscopy analysis, the electrodeposited Mn oxide is identified as a Mn₃O₄ spinel, likely hausmannite.

Table 4-1 Summary of XPS data and comparison with other Mn oxide materials.

	Mn (At%)	O (At%)	Mn 2p Avg. Oxidation State	Mn 3s Peak Splitting (eV)	Mn 2p (3/2)/O 1s Binding Energy Difference (eV)
This work	45.3	54.7	2.55	5.54	111.61
Mn ₃ O ₄ [193]	42.9	57.1	2.67	5.50	111.53
Mn ₂ O ₃ [193]	40.0	60.0	3.00	5.41	111.73
MnO[193]	50.0	50.0	2.00	5.79	111.29
MnO ₂ [193]	33.3	66.7	4.00	4.87	112.37

4.3.2 Electrochemical Results

Figure 4-3a shows the CV results for an assembled ZIB using a scan rate of 0.1 mV s⁻¹. For the first cathodic and anodic scans, one reduction peak and one oxidation peak occur at 1.18 V and 1.57 V, respectively. On subsequent cycling, two reduction peaks are present at 1.26 V and 1.37 V on the cathodic scan. Two oxidation peaks are also present during the anodic scan at 1.57 V and a small shoulder at ~1.60 V. The CV results show relatively good overlap upon cycling, suggesting good cyclability and the CV behaviour is similar to that of other Mn oxide ZIBs [42], [66], [67], [71].

Figure 4-3b shows GCD results obtained for the ZIB. The initial or conditioning cycle was done at a low specific current of 50 mA g⁻¹ to condition or prime the battery before testing, since the initial GCD cycle is different from the subsequent cycles. The subsequent charge and discharge cycles were completed at 300 mA g⁻¹. The battery has a high initial capacity of 376 mAh g⁻¹ during the conditioning cycle. At 300 mA g⁻¹, the battery has a capacity of 297 mAh g⁻¹ for the 1st cycle and a maximum capacity of 328 mAh g⁻¹; the capacity retention is 118% after 100 cycles. During cycling, the discharge plateaus occur at about 1.40 V and 1.30 V and the charge plateaus occur at about 1.52 V and 1.58 V. The peaks from the CV testing correspond well with the plateaus observed during GCD testing, with some variation due to the CV scan rate and applied specific

current in GCD testing. Additionally, the two pairs of peaks in the CV results and the two plateaus during both charge and discharge indicate a two-step reaction mechanism for the assembled ZIB.

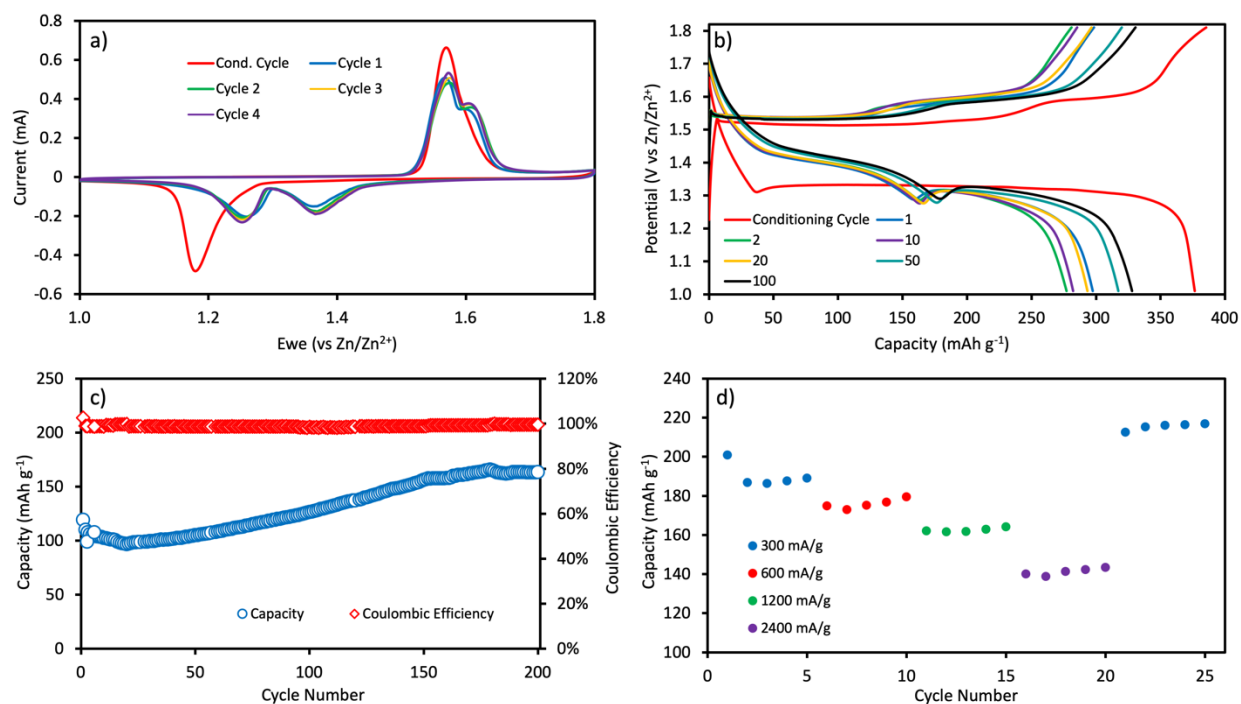


Figure 4-3 Electrochemical and battery performance of assembled ZIB: a) CV results at a scan rate of 0.1 mV s^{-1} , b) GCD testing with the conditioning cycle done at an applied specific current of 50 mA g^{-1} and the subsequent cycles at 300 mA g^{-1} , c) battery cyclability results at an applied specific current of 1 A g^{-1} , d) rate capability test results at various applied current densities.

Cycling performance of the battery under an applied specific current of 1 A g^{-1} is presented in Figure 4-3c. The assembled ZIB has very good performance with a final capacity of 163 mAh g^{-1} and a capacity retention of 137% after 200 charge and discharge cycles. The battery capacity also stabilizes toward the end of the cycling. The assembled battery has a Coulombic efficiency close to 100%, indicating good battery reversibility.

The rate capability of the assembled battery was tested as well and is presented in Figure 4-3d. The Mn_3O_4 cathode was cycled 5 times at different specific currents and exhibited good rate capability. At 300, 600, 1200, 2400, and then again at 300 mA g^{-1} , the battery was able to deliver capacities of 201, 180, 164, 143, and 217 mAh g^{-1} , respectively. This also corresponds to a capacity retention of 110% at a specific current of 300 mAh g^{-1} . The difference in the capacities obtained

at an applied specific current of 300 mA g^{-1} in the GCD test and the rate capability test can be attributed to cathode wettability, gradual activation of the cathode, and sample variation. If the cathode material does not wet properly, the electrolyte may not be in complete contact with the active material, which can reduce battery capacity. Gradual activation of the cathode also affects the capacities in a similar way to wettability. As the cathode cycles, the electrolyte will access more of the active material which will result in an increase in capacity. Additionally, the cathode may not undergo complete activation at higher specific currents, resulting in reduced initial capacities [42]. Improved cathode wettability and gradual cathode material activation may also explain why there is a steady increase in capacity during GCD testing until the capacity stabilizes at close to 200 cycles [143], [157]. Overall, the good performance of the assembled ZIB can be attributed to several factors. The flake-like morphology of the Mn_3O_4 provides a large surface area providing the electrode with better access to the electrolyte. Also, the Mn_3O_4 flakes are very thin ($\sim 2\text{-}3 \text{ }\mu\text{m}$) and are deposited on a conductive CP substrate, which can help counter the relatively poor conductivity of Mn_3O_4 [47]. The addition of 0.2 M MnSO_4 to the electrolyte provides Mn^{2+} ions in the electrolyte, which have been shown to reduce the dissolution of Mn from the electrode and help the electrode and electrolyte reach an equilibrium state [21], [32].

Table 4-2 compares the cycling results for battery testing in this work with those from other batteries using Mn-based spinel cathodes. The batteries from this work either outperform or display comparable performance to other batteries presented in the literature. Galvanostatic intermittent titration testing (GITT) was conducted for the first discharge cycle after conditioning to determine the diffusion coefficient for each plateau (Figure S4-3). The first plateau shows a smaller potential jump during the rest period versus the second plateau. This indicates that the process occurring during the second plateau has a smaller diffusion coefficient compared with the first plateau and is more kinetically limited [39], [71], [143].

Table 4-2 Battery cycling performance comparison between this work and other Mn_3O_4 based ZIBs found in the literature.

Cathode material	Electrolyte	Potential window (V)	Specific current ($mA\ g^{-1}$)	Initial capacity ($mAh\ g^{-1}$)	Final capacity ($mAh\ g^{-1}$)	Capacity retention	Ref
Mn_3O_4	2M $ZnSO_4$ + 0.2M $MnSO_4$	1.0 – 1.8	1000	119	163	137% after 200 cycles	This work
Stainless-steel@ Mn_3O_4	2M $ZnSO_4$ + 0.1M $MnSO_4$	1.0 – 1.8	100	296	290*	98% after 50 cycles	[136]
$ZnMn_2O_4$	1M $ZnSO_4$ + 0.5M $MnSO_4$	0.8 – 1.9	100	86.0	106.5*	124% after 300 cycles*	[32]
$ZnMn_2O_4/Mn_2O_3$	1M $ZnSO_4$	0.8 – 1.9	500	82.6	111.9*	135% after 300 cycles*	[66]
Mn_3O_4	2M $ZnSO_4$	0.8 – 1.9	500	45.5*	106.1*	233% after 300 cycles*	[42]
Cation-deficient $ZnMn_2O_4$	3M $Zn(CF_3SO_3)$	0.8 – 2.0	500	~90*	~85*	94% after 500 cycles	[33]
$ZnMn_2O_4/N$ -doped graphene	1M $ZnSO_4$ + 0.5M $MnSO_4$	0.8 – 1.8	1000	76*	74	97.4% after 2500 cycles	[177]

* Values were determined from data presented in the specific reference.

4.3.3 Reaction Mechanism

The reaction mechanism involving Mn_3O_4 , and Mn oxide compounds in general, is still widely debated and not completely understood. To gain a better understanding of the electrochemical mechanism, the Mn_3O_4 on CP cathode was examined at different stages during charge and discharge for several cycles. In particular, the conditioning cycle, the 1st cycle after conditioning, and the 5th cycle were examined. A specific current of 50 $mA\ g^{-1}$ was applied for all cycles for consistency. For the conditioning cycle, two samples were examined during discharge, at potentials of 1.35 V (pt. 1 on discharge) and 1.25 V (pt. 2 on discharge) and two samples were examined during charge, at potentials of 1.54 V (pt. 1 on charge) and 1.63 V (pt. 2 on charge). These positions correspond to the beginning and end of the discharge plateau and the ends of the two charge plateaus.

Figure 4-4 presents SEM images, STEM images and EDS mapping results for discharge and charge during the conditioning cycle. Inset capacity plots associated with the SEM micrographs show where the battery was stopped during the conditioning cycle for examination.

The SEM image for the first discharge point at 1.35 V (Figure 4-4a) shows the morphology of the cathode, which is very similar to the morphology for the pristine sample (Figure 4-1b). The corresponding STEM image and EDS maps for this sample show carbon particles (~50 nm in size) from the CP, partially covered with Mn oxide particles (bright regions in the STEM annular dark field (ADF) image). Zn is present in this sample, with the Zn map corresponding to the positions of Mn oxide. This result indicates that Zn^{2+} intercalation occurs during the first plateau, which is contradictory to several Mn_3O_4 , and other Mn oxide, reaction mechanisms reported in the literature that suggest only H^+ intercalation occurs within the first plateau [39], [42]. H^+ intercalation may be occurring simultaneously with the observed Zn^{2+} intercalation; however, H is not detectable by EDS and could not be confirmed. There is also a weak STEM EDS signal from S that overlaps with Mn oxide, indicating that some S may be incorporated. The S is likely from the SDS in the electrodeposition solution, as discussed in Section 4.3.1 and shown in Figure 4-1. A pristine cathode (Mn_3O_4 on CP) was immersed in the electrolyte for several days. Post treatment SEM EDS analysis revealed no Zn, confirming that Zn was not surface absorbed from the electrolyte and is actually incorporated in Mn_3O_4 during discharge (Figure S4-4).

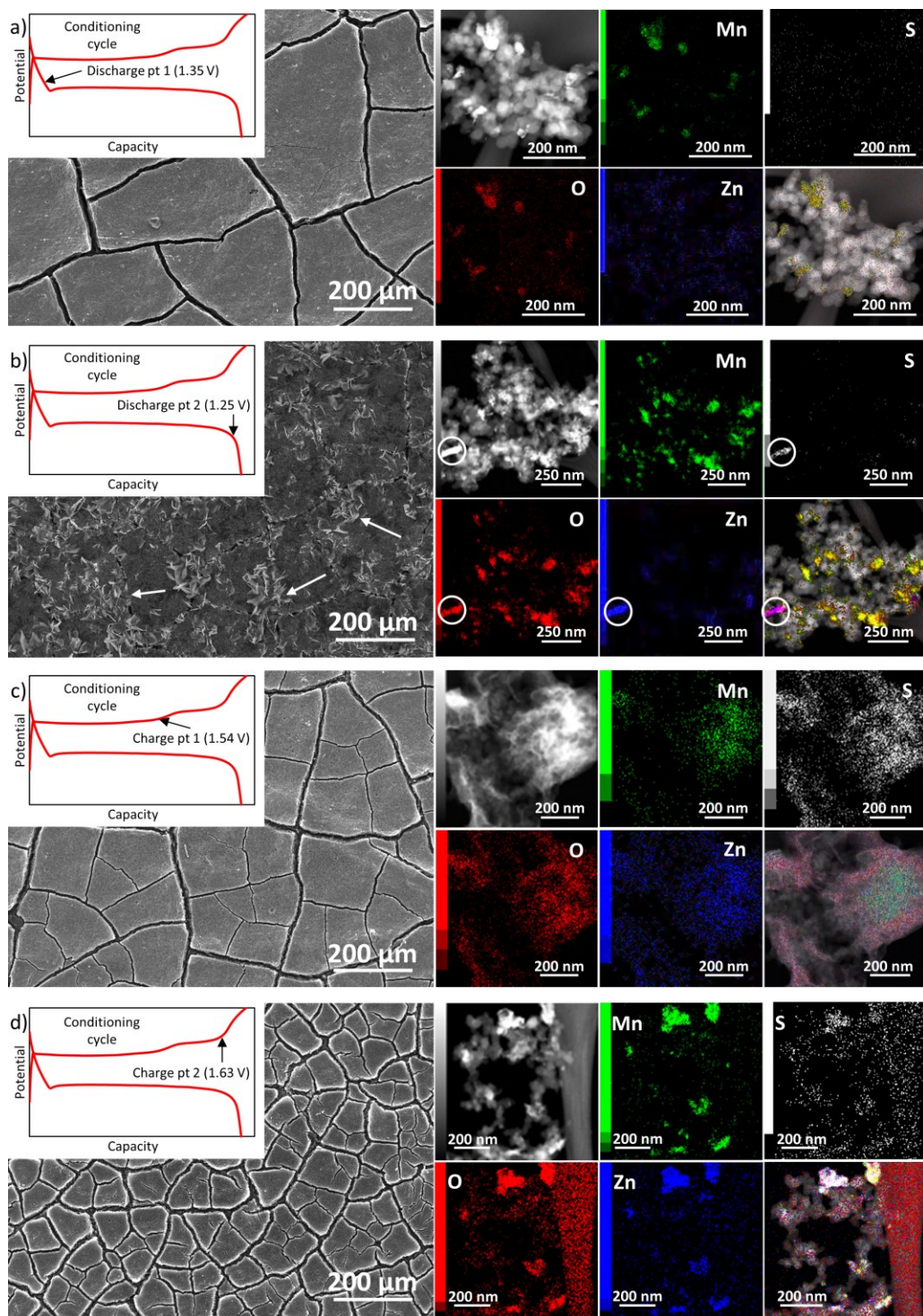


Figure 4-4 SEM SE images, STEM ADF images, and STEM EDS maps for the conditioning cycle at different points along discharge and charge: a) discharge point 1 (1.35 V), b) discharge point 2 (1.25 V) with arrows indicating ZSH plates, c) charge point 1 (1.54 V), and d) charge point 2 (1.63 V). The circled particles in b) indicate the Zn-S-O rich particles. The maps shown in the bottom righthand corner for each potential are overlays of Mn, O, Zn, and S. The inset GCD plots depict the positions along the cycle where the battery was stopped for analysis.

Figure 4-4b shows a similar set of images and EDS maps to Figure 4-4a for the cathode examined at the second discharge point (1.25 V). Large plate-like formations not present in the as deposited sample or the sample from Figure 4-4a, are present. The plates resemble ZSH that has been reported in the literature to form during discharge of Mn oxide electrodes [67], [71]. Interestingly, these plates tend to initially form in the areas between the Mn_3O_4 islands on the CP and so the Mn_3O_4 surface is only partially covered. In the literature, ZSH generally completely covers the surface of the cathode [67], [71]. The edges of the Mn_3O_4 deposits (within the gaps) likely act as preferential nucleation sites (larger surface area per unit volume) for ZSH formation, resulting in ZSH formation between the Mn_3O_4 islands, rather than forming directly on top of the Mn_3O_4 layer. Once the gaps between the Mn_3O_4 islands have been filled with ZSH, further formation occurs across the surface of the Mn_3O_4 [181]. The STEM image and EDS results reveal two different microstructural features. Mn oxide, with Zn incorporation/intercalation, is present (as in Figure 4-4a); however, there is a Zn-O-S rich phase (circled particles in Figure 4-4b) which correlates with the ZSH plates in the SEM image. These regions do not contain Mn and exhibit brighter contrast than Mn oxide in the STEM ADF image. It is generally agreed that ZSH plates form because of a localized change in the pH of the electrolyte from the formation of MnOOH ; however, the presence of MnOOH could not be confirmed in this work [21], [67], [71].

Similar analyses were done for the first charge point (1.54 V) and the second charge point (1.63 V) during the conditioning cycle (Figure 4-4c and Figure 4-4d, respectively). The morphology of the cathode resembles that of the as deposited sample and most of the ZSH plates have dissolved at the first charge point. The STEM/EDS analysis shows that some ZSH is still present on the surface of the cathode (Figure 4-4c). In fact, a Mn oxide particle is covered by ZSH. For the 1.63 V sample, the ZSH plates have completely dissolved (Figure 4-4d). The morphology of the sample is very similar to the as deposited Mn_3O_4 . Zn is still present within the Mn oxide after the electrode is almost fully charged. This may be due to a phase change of the Mn_3O_4 to ZnMn_2O_4 (which has a crystal structure very similar to hausmannite Mn_3O_4) during the discharge portion of the conditioning cycle [55], [67], [71] and may account for the different shape of the GCD curves during subsequent cycles. It should be noted that some S remains in the Mn oxide (or ZnMn_2O_4) and is likely from the fabrication process, as previously discussed.

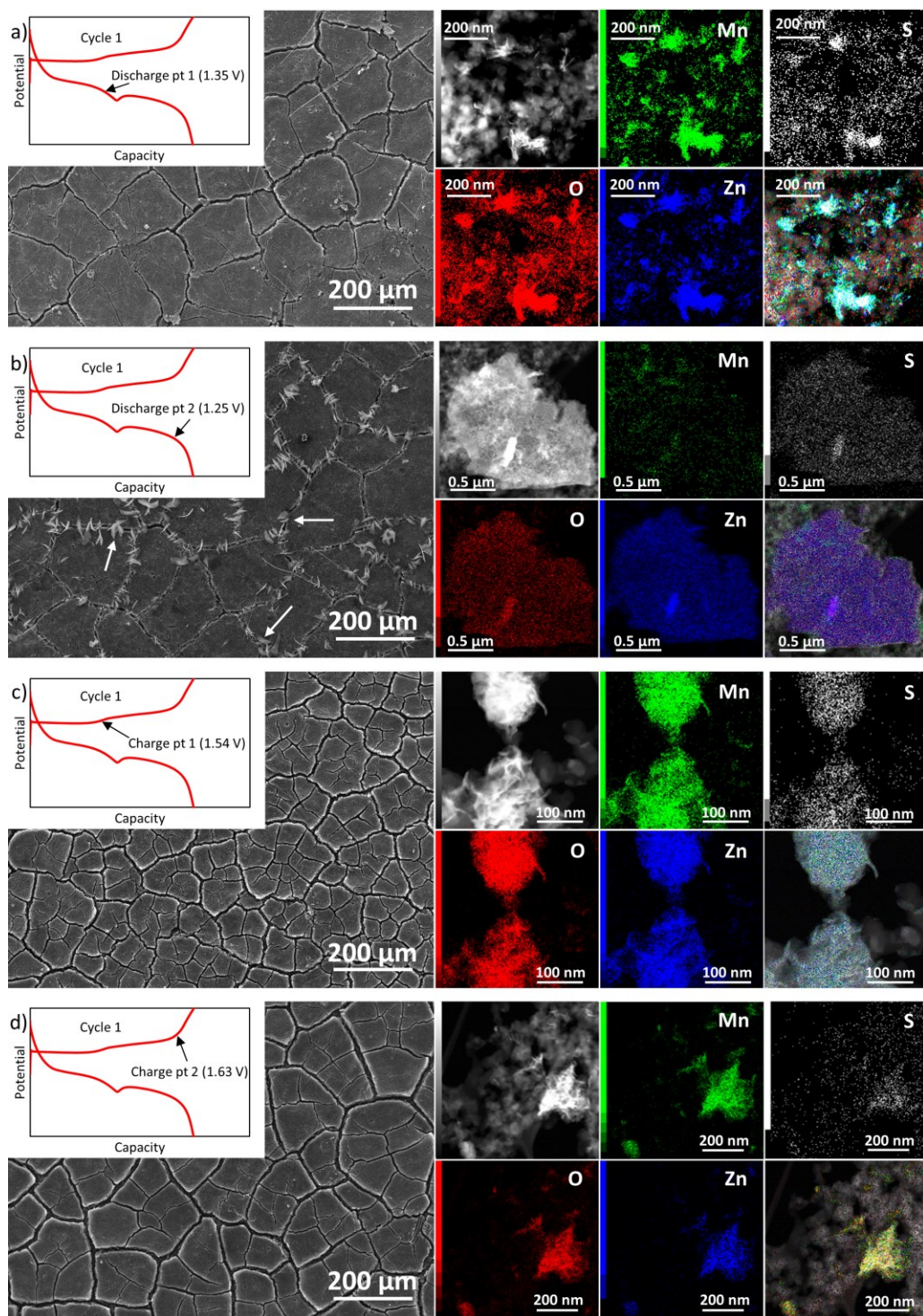


Figure 4-5 SEM SE images, STEM ADF images, and STEM EDS maps for the 1st cycle after conditioning at different points along discharge and charge: a) discharge point 1 (1.54 V), b) discharge point 2 with the arrows indicating ZSH plates (1.25 V), c) charge point 1 (1.54 V), and d) charge point 2 (1.63 V). The maps shown in the bottom right-hand corner for each potential are overlays of Mn, O, Zn, and S. The inset GCD plots depict the positions along the cycle where the battery was stopped for analysis.

Microstructural analysis was done for the 1st cycle (Figure 4-5) and the 5th cycle (Figure S4-5) after conditioning. The positions selected correspond to the ends of the first and second plateaus on charge and discharge. The cathode material at the first point of discharge (1.35 V) of the 1st cycle (Figure 4-5a) has a morphology similar to the first point of discharge during the conditioning cycle (Figure 4-4a). Mn oxide particles, with Zn intercalation and some S, are present; no ZSH plates were detected. The detected S is most likely from the cathode fabrication process as previously discussed. At the second point of discharge (1.25 V - Figure 4-5b), ZSH plates reappear; one such plate is shown in the STEM image and EDS maps. An electron diffraction pattern was obtained from the ZSH plate in Figure 4-5b and was indexed to ZSH (Figure S4-6 and Table S4-1), confirming that the plates are indeed ZSH. Additionally, less ZSH is formed when compared with the conditioning cycle discharge. The lower amount of ZSH correlates with a smaller second discharge plateau for the first cycle after conditioning relative to the second discharge plateau for the conditioning cycle. Furthermore, the reduced formation of ZSH after the conditioning cycle may account for the excellent GCD performance of the battery, since ZSH formation on the cathode surface has been described as detrimental to cyclability [71]. Combining the GITT results for the 1st cycle after conditioning with the electron microscopy results, ZSH formation during the second plateau is confirmed and its formation is most likely kinetically limited [67], [71]. Similar electron microscopy results were obtained for the 5th cycle after conditioning and are presented in Figure S4-5. Figure 4-5c and Figure 4-5d show the two different charge points at the end of each charge plateau (1.54 and 1.63 V) for the 1st cycle after conditioning. The results shown are similar to those for the conditioning cycle. The ZSH plates have dissolved by the end of the 1st plateau and the morphology is similar to that for the as deposited sample. The Mn oxide particles still contain Zn and some S. Although the GCD curves for the conditioning cycle and first cycle after conditioning are different, the results from SEM and STEM EDS are very similar. This further supports the proposed transformation of Mn₃O₄ to ZnMn₂O₄ during the conditioning cycle discharge. The electron microscopy results for the 5th charge cycle after conditioning are similar to those for the 1st charge cycle and are presented in Figure S4-5.

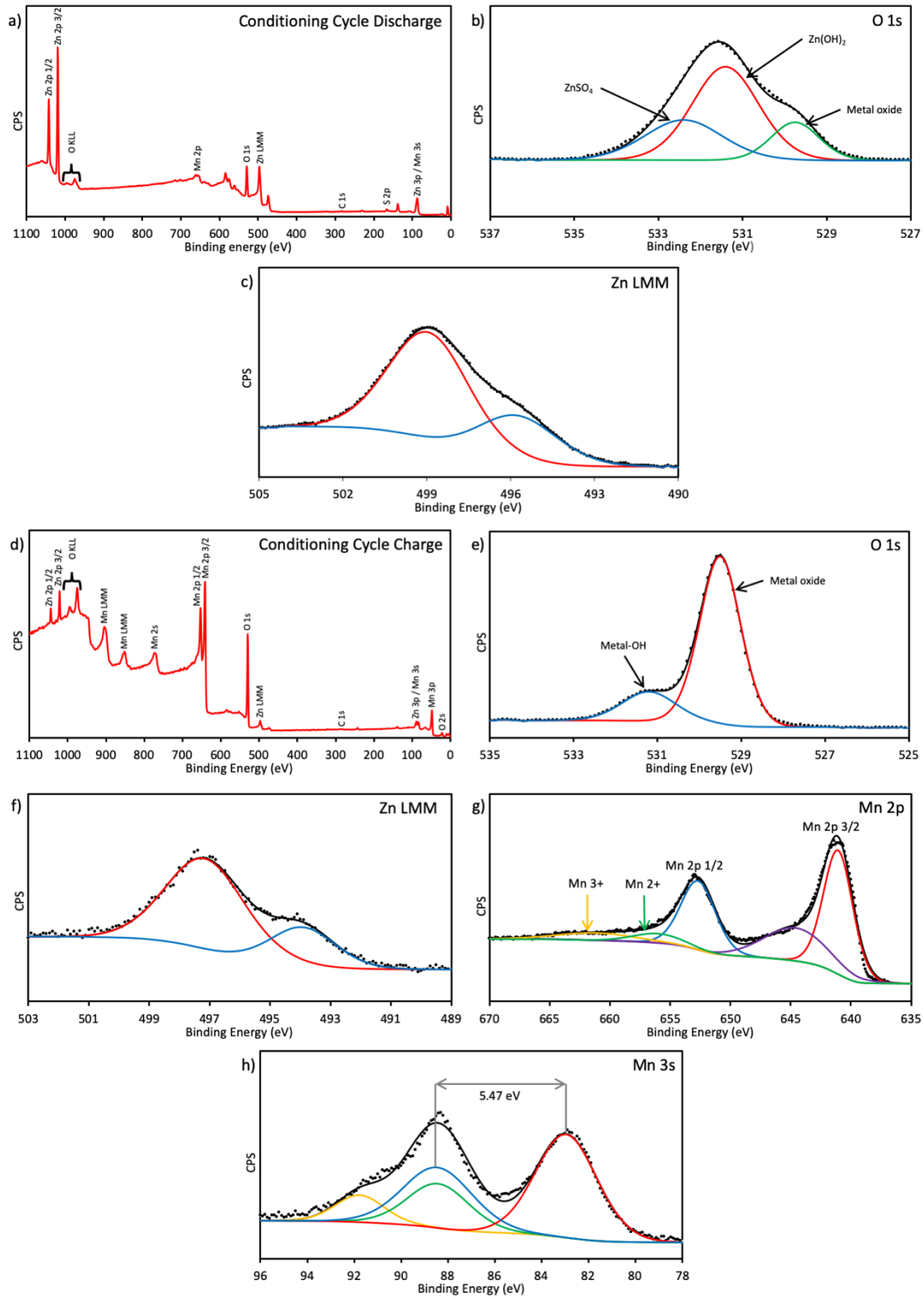


Figure 4-6 XPS results for the full conditioning cycle discharge (1.0 V) and charge (1.8 V): a) Discharge survey scan, b) discharge O 1s spectrum, c) discharge Zn Auger LMM peak, d) charge survey scan, e) charge O 1s spectrum, f) charge Zn Auger LMM spectrum, g) charge Mn 2p spectrum, and h) charge Mn 3s spectrum.

Fully charged (1.8 V) and discharged (1.0 V) samples after the conditioning cycle and the 5th cycle after conditioning were examined using XPS. The XPS data are summarized in Table 4-3. For the fully discharged conditioning cycle, there are intense Zn 2p peaks and quantification shows a significant increase in the amount of Zn, which supports Zn intercalation and the formation of ZSH during discharge (Figure 4-6a). The position of the S peak in the survey scan corresponds to ZnSO₄, most likely present as ZSH [196]. Additionally, the strong Mn peaks are significantly reduced in intensity (Mn 2p and Mn 3s peaks) and some peaks have completely disappeared (Mn LMM Auger and Mn 2s peaks) when compared to the pristine Mn₃O₄ survey scan (Figure S4-1). The position of the main O 1s peak and left shoulder, as well as the main Zn (Auger) LMM peak, indicate that ZnSO₄ and Zn(OH)₂ are present on the cathode surface, most likely in the form of ZSH (Figure 4-6b and Figure 4-6c) [197]–[199]. The O 1s peak has a shoulder at 529.7 eV which indicates that a metal oxide is also present, possibly in the form of ZnMn₂O₄ (Figure 4-6b) [32], [193], [200]. The oxidation state of the compound could not be reliably determined due to significant overlap of the Zn 3s peak and Mn 3p peaks, as well as the poor Mn 2p satellite feature signal because of the formation of ZSH on the surface of the cathode. After full charge for the conditioning cycle, the survey scan shows the return of the Mn 2s and Mn Auger peaks and a significant increase in intensity of the Mn 2p and Mn 3s peaks (Figure 4-6d). However, Zn 2p and Zn Auger peaks are still present, but reduced in intensity, indicating incomplete Zn extraction on charge. Additionally, the survey scan does not show any S, indicating that the ZSH has all been dissolved. The strong O 1s peak at 529.5 eV is associated with the presence of metal oxides, most likely in the form of ZnMn₂O₄ (Figure 4-6e) [32], [193], [200]. The small shoulder at 531.2 eV for the O 1s spectrum corresponds with surface adsorbed OH [183], [193], [200]. The change in the Zn LMM (Auger) peak shape and position (989.5 eV) on recharge indicates that a Zn containing oxide remains on charge, possibly in the form of ZnMn₂O₄ (Figure 4-6f) [198], [201]. The Mn 2p satellite peak areas and Mn 3s peak splitting signify a return to a Mn spinel structure, further suggesting ZnMn₂O₄ remains on recharge (Figure 4-6g and Figure 4-6h) [32], [200]. The decrease in the Mn 3s peak splitting value compared with the pristine sample also indicates an increase in the average oxidation state of the Mn oxide (Table 4-3) [181]. This supports the formation of ZnMn₂O₄; as Mn²⁺ is replaced with Zn²⁺, the average oxidation state of Mn would increase closer to 3. It is noted that there is significant overlap between the Mn 3s and Zn 3p peaks, which reduces the accuracy of determining oxidation states from Mn 3s peak splitting.

The XPS results for the conditioning cycle, both charge and discharge, corroborate the electron microscopy results. Overall, the microstructural analysis for the conditioning cycle indicates that the difference in shape between conditioning cycle CV and GCD curves and the curves for the subsequent cycles is most likely due to a phase change from Mn_3O_4 to ZnMn_2O_4 .

The XPS data collected after full discharge for the 5th cycle after conditioning are similar to the results obtained after discharge for the conditioning cycle. The survey scan shows strong Zn 2p and Zn LMM Auger peaks and a marked reduction in intensity of the Mn peaks, indicating significant amounts of Zn incorporated in Mn_3O_4 and/or forming ZSH during discharge (Figure 4-7a). The O 1s peak and shoulder at 531.0 eV and 532.3 eV, respectively, correlate with ZSH, while the shoulder at 529.4 eV suggests a metal oxide is also present (Figure 4-7b) [32], [197], [198]. The Zn Auger peak position (988.0 eV) and shape suggests the formation of a Zn-S containing compound, most likely in the form of ZSH (Figure 4-7c) [196], [198]. XPS data for the 5th charge cycle after conditioning are also similar to the data for the conditioning charge cycle. The survey scan shows the return of the strong Mn peaks, but the Zn peaks (2p and Zn LMM) intensities are significantly reduced indicating that most of the Zn has been removed (Figure 4-7d). The position and shape of the O 1s peaks (Figure 4-7e) and the Zn Auger peaks (Figure 4-7f) indicate that a Zn containing oxide may be present on the cathode, likely as ZnMn_2O_4 [32], [200], [201]. The small shoulder at 531.2 of the O 1s peak is most likely from surface adsorbed OH [183], [193], [200]. The oxidation state determined from Mn 2p satellite features (Figure 4-7g) and the Mn 3s peak splitting (Figure 4-7h) indicate a return to a Mn-based spinel, further suggesting that ZnMn_2O_4 remains on charge [32], [200]. Furthermore, the Mn 3s peak splitting is shown to decrease further when compared with the conditioning cycle, indicating an increase in the oxidation state of the Mn oxide as it is cycled [181]. The increase is likely due to additional Mn^{2+} substitution by Zn^{2+} , further supporting the formation of ZnMn_2O_4 . The XPS data also shows an increase in the amount of Zn for the 5th cycle versus the conditioning cycle, which supports the increase in Mn oxidation state due to Zn substitution and the formation of ZnMn_2O_4 (Table 4-3). The XPS data for the 5th cycle after conditioning corroborates the electron microscopy results for both the 1st cycle after conditioning and the 5th cycle after conditioning.

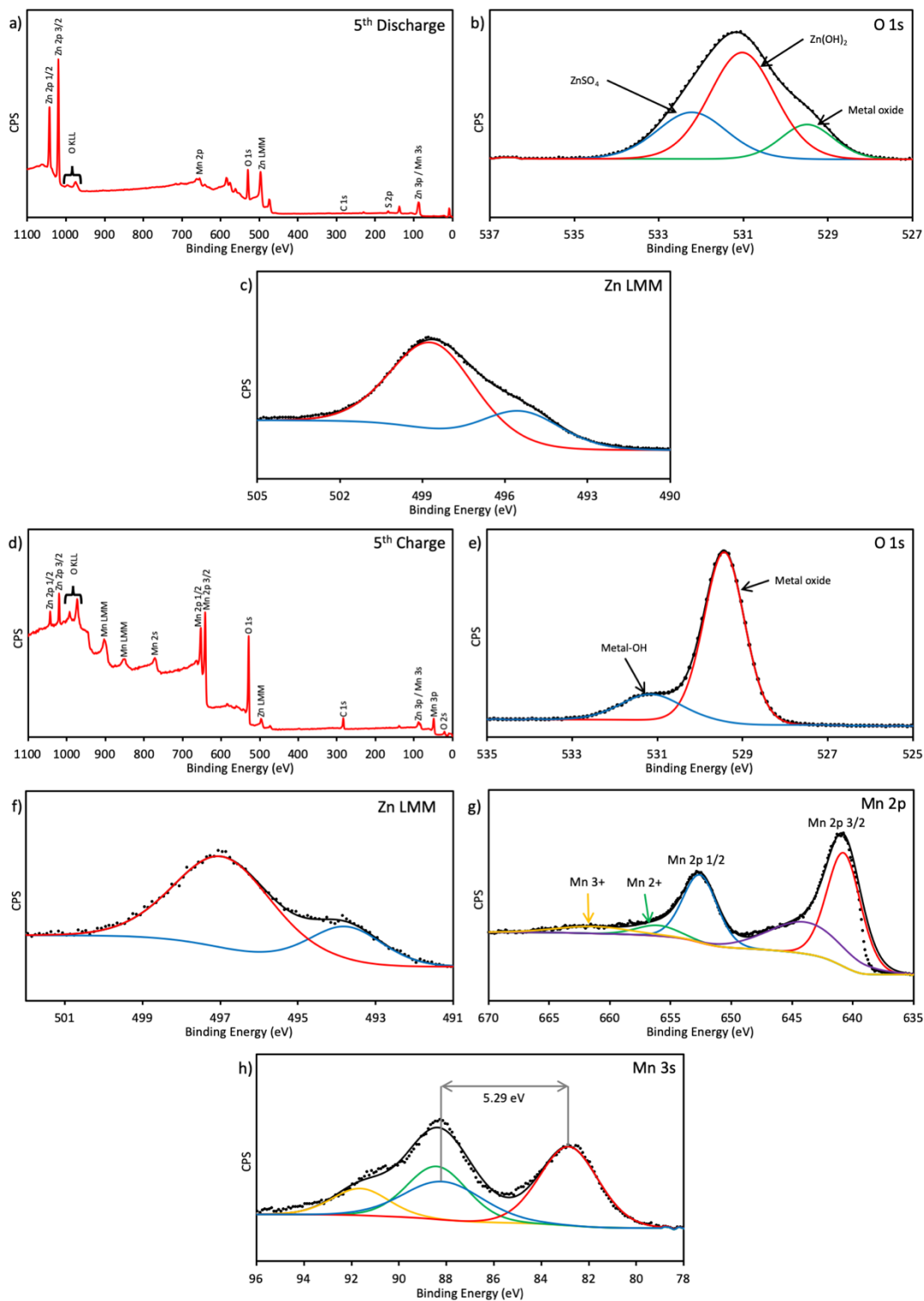


Figure 4-7 XPS results for the full discharge (1.0 V) and charge (1.8 V) of the 5th cycle after conditioning: a) Discharge survey scan, b) discharge O 1s spectrum, c) discharge Zn Auger LMM spectrum, d) charge survey scan, e) charge O 1s spectrum, f) charge Zn Auger LMM spectrum, g) charge Mn 2p spectrum, and h) charge Mn 3s spectrum.

Table 4-3 Summary of XPS data collected for as deposited Mn_3O_4 cathode, cathode after the conditioning cycle, and cathode after the 5th cycle after conditioning

	Mn (At%)	O (At%)	Zn (At%)	S (At%)	Mn 2p Avg Ox State	Mn 3s Splitting (eV)	Mn 2p (3/2) / O 1s Difference (eV)	Zn LMM Kinetic Energy (eV)	O 1s (eV)	S 2p (eV)
Deposited Mn_3O_4	45.3	54.7	-	-	2.55	5.54	111.62	-	-	-
Conditioning discharge	8.8	52.1	31.1	8.0	-	-	-	987.7	531.5	168.6
Conditioning charge	43.9	53.6	2.5	-	2.54	5.47	111.55	989.5	529.5	-
5th discharge	9.1	52.8	31.7	6.3	-	-	-	988.0	531.0	168.0
5th charge	44.0	52.1	3.9	-	2.52	5.29	111.47	989.7	529.4	-
Mn_3O_4 [193]	42.9	57.1	-	-	2.67	5.5	111.53	-	-	-

Based on the electrochemical and microstructural characterization data for the conditioning cycle, the 1st cycle after conditioning, and the 5th cycle after conditioning, some insight can be provided regarding the reaction mechanism for the Mn_3O_4 -based cathode. The results indicate a mechanism similar to that for $ZnMn_2O_4$ proposed by Chen et al. [177] and somewhat similar to that for MnO_2 proposed by Huang et al. and Yun et al. [67], [71]. Overall, the proposed reaction mechanism can be summarized as follows. During the conditioning cycle discharge, Zn^{2+} and possibly H^+ intercalation occur during the first plateau. This is followed by the formation of ZSH from Zn and S in the electrolyte during the second plateau. Furthermore, during the conditioning cycle, the Mn_3O_4 cathode undergoes a phase transformation to $ZnMn_2O_4$ as more Zn^{2+} is intercalated into the cathode. Both Mn_3O_4 and $ZnMn_2O_4$ have very similar crystal structures and lattice parameters, which facilitates the transformation. During the conditioning cycle charge, ZSH is dissolved during the first charge plateau and Zn^{2+} (and H^+ if present) ions are extracted from the cathode during the second charge plateau. However, a finite amount of Zn is not extracted and remains, most likely as $ZnMn_2O_4$ from the initial phase transformation. During subsequent discharge cycles after conditioning, the formed $ZnMn_2O_4$ will intercalate Zn^{2+} (and possibly H^+) ions during the first plateau. ZSH again forms during the second plateau. On charge, ZSH will

dissolve during the first plateau and most of the Zn^{2+} (and H^+) ions are extracted during the second plateau. This analysis indicates a reaction mechanism different from what has been previously proposed for Mn_3O_4 and other Mn spinels used for ZIBs cathodes. Other Mn_3O_4 mechanisms propose only H^+ intercalation during the first plateau, with Zn^{2+} intercalation and ZSH formation in the second [42], [136]. This work clearly shows that Zn is present in the Mn oxide during the first plateau on both charge and discharge. Additionally, other proposed Mn_3O_4 mechanisms involve a phase change to MnO_2 or MnO while this work proposes the transformation of Mn_3O_4 to ZnMn_2O_4 . ZnMn_2O_4 spinel structures are generally proposed to undergo only Zn intercalation within both plateaus, without the formation of ZSH, while this work clearly shows ZSH forms during the second plateau [32], [33]. However, further tests and analysis are needed to further elucidate the mechanism(s) for charge and discharge of Mn_3O_4 .

4.4 Summary

Nanocrystalline Mn_3O_4 cathodes for zinc-ion batteries (ZIBs) were fabricated by simple pulsed electrodeposition onto carbon paper (CP). Electrodeposition offers several advantages including the elimination of binders, room temperature deposition, and very short fabrication times. The maximum capacity for a ZIB using electrodeposited Mn_3O_4 as the cathode was 376 mAh g^{-1} . The battery was able to achieve a capacity retention of 139% after 200 cycles at a specific current of 1 A g^{-1} . The fabricated electrode also showed excellent rate capability performance with capacities of 201, 180, 164, 143, and 217 mAh g^{-1} at specific currents of 300, 600, 1200, 2400, and again at 300 mA g^{-1} , respectively. The excellent battery performance of the Mn_3O_4 is proposed to be a result of several different factors: the crystal structure of the deposited oxide, oxide morphology and thickness, limited formation of zinc sulfate hydroxide (ZSH, $\text{Zn}(\text{OH})_2\text{ZnSO}_4 \cdot x\text{H}_2\text{O}$) only within Mn_3O_4 cracks during cycling, and the CP substrate providing good electronic conductivity. Through a combination of microstructural analysis, using electron microscopy and X-ray photoelectron spectroscopy, and electrochemical testing, additional insight into the reaction mechanisms has been obtained and points to a two-step reaction mechanism for ZIBs using Mn_3O_4 cathodes. The first discharge potential plateau during discharge likely involves intercalation of Zn^{2+} and possibly H^+ , followed by a conversion reaction forming ZSH during the second discharge potential plateau. The reverse occurs on charge.

4.5 Supplementary Information

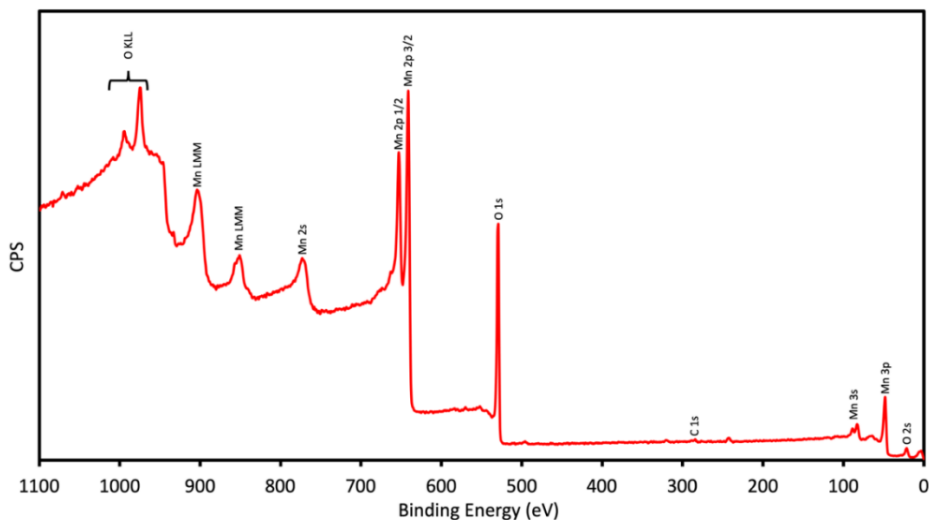


Figure S4-1 XPS survey scan for the as deposited Mn_3O_4 sample, showing strong Mn 2p and O 1s peaks, as well as a small Mn 3s peak.

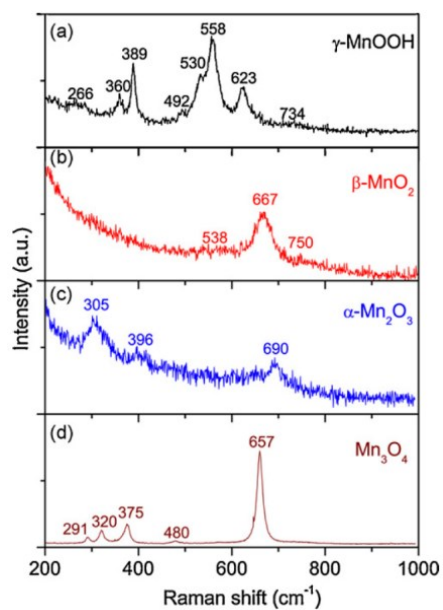


Figure S4-2 Room temperature Raman spectra for (a) γ -MnOOH, (b) β -MnO₂, (c) α -Mn₂O₃, and (d) Mn₃O₄ [194]. It should be noted that several factors can influence Raman spectroscopy results including type of laser used, power of the laser, material crystallinity, amount of material, material stress and orientation, and material defects [167], [168].

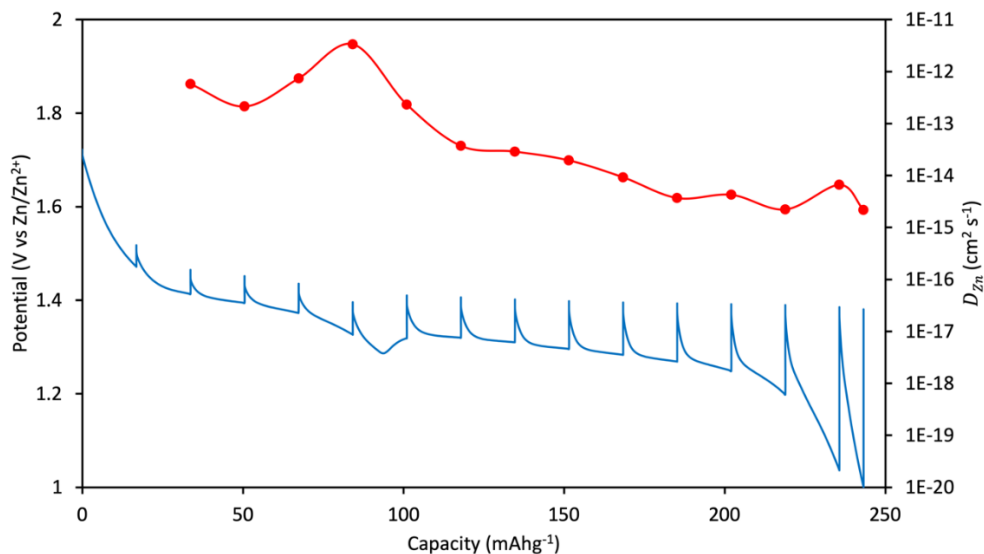


Figure S4-3 GITT results for the first cycle after conditioning. A 10 min ON period and a 20 min REST period were used. A specific current of 100 mA g^{-1} was applied during the ON period. The red circles and line show the calculated diffusion coefficient for Zn^{2+} for different points along the discharge cycle.

The following equation was used to determine the diffusion coefficient for Zn^{2+} in the active material at different points across the discharge cycle using data obtained from the galvanostatic intermittent titration technique (GITT) [45], [177]. The diffusion coefficient for Zn^{2+} in the first plateau is significantly larger than the Zn^{2+} diffusion coefficient in the second plateau.

$$D_{\text{Zn}} = \frac{4}{\pi\tau} \left(\frac{m_{\text{B}} v_{\text{m}}}{M_{\text{B}} S} \right)^2 \left(\frac{\Delta E_{\text{s}}}{\Delta E_{\tau}} \right)^2 \quad (4-1)$$

where D_{Zn} ($\text{cm}^2 \text{ s}^{-1}$) is the diffusion coefficient of Zn^{2+} ; τ (s) is the current pulse time, m_{B} (g) is the amount of active material in the electrode, v_{m} ($\text{cm}^3 \text{ mol}^{-1}$) is the molar volume of the active material, M_{B} (g mol^{-1}) is the molecular weight of the active material, S (cm^2) is the geometric contact area of electrode with the electrolyte, ΔE_{s} (V) is the potential change between two consecutive relaxation steps, ΔE_{τ} (V) is the potential change during the constant current pulse, [45], [177]. It is noted that the applied specific current, applied specific current time, rest period

time, and the actual surface area of the electrode will influence the calculated diffusion coefficient values [176].

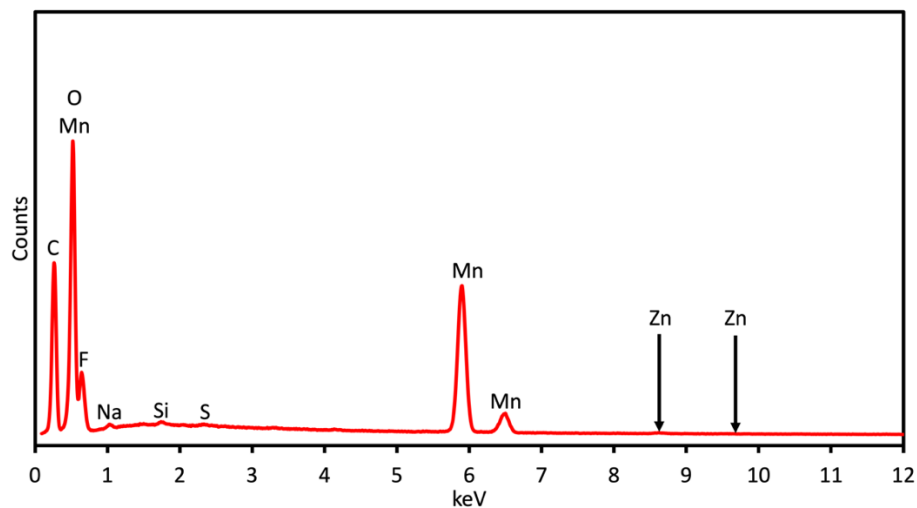


Figure S4-4 SEM EDS spectrum for an uncycled Mn_3O_4 on CP sample that was submerged in ZIB electrolyte (2M ZnSO_4 and 0.2M MnSO_4) for one week. The arrows on the image indicate where the Zn peaks would be found if they were present in the sample.

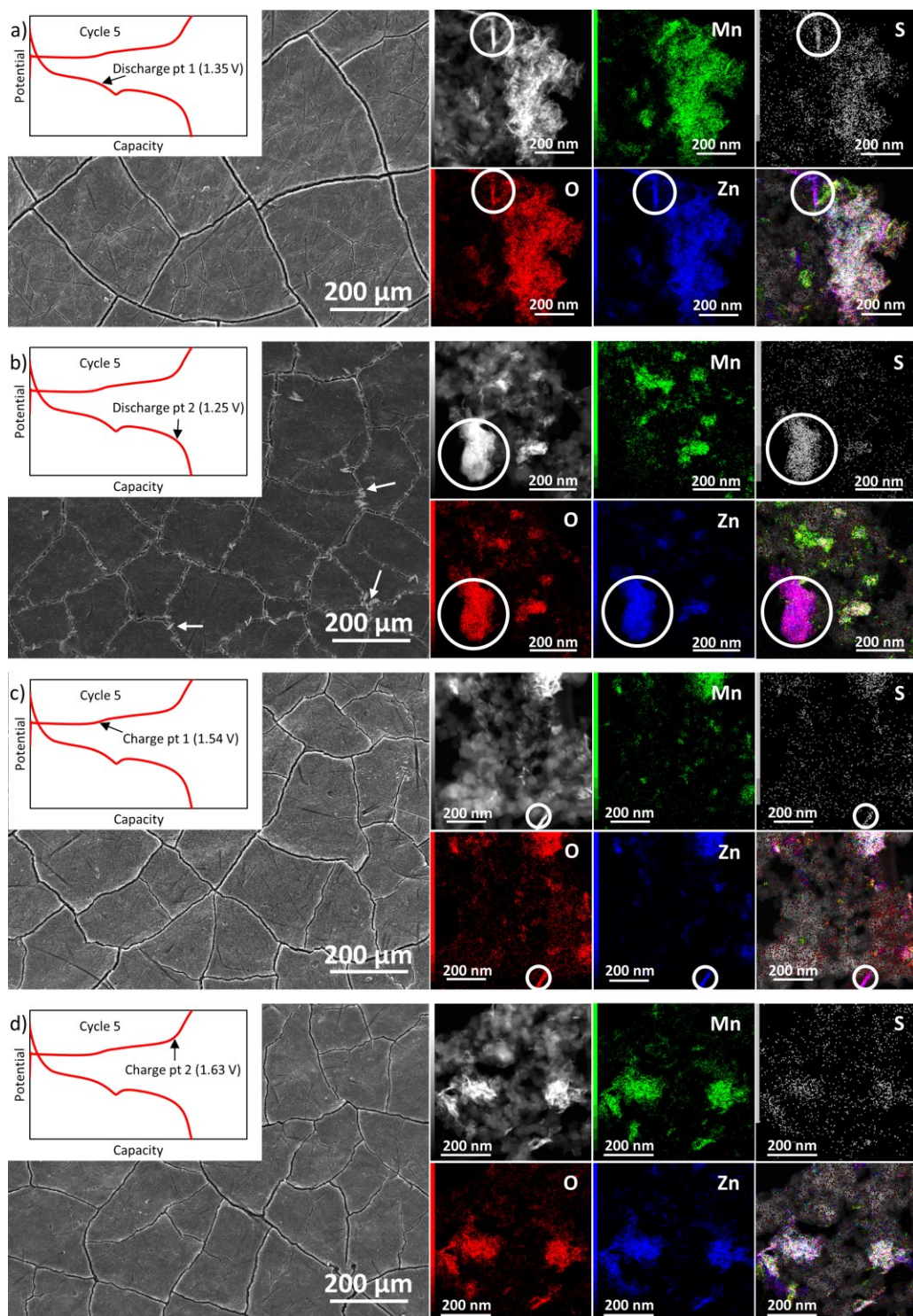


Figure S4-5 SEM SE images, STEM ADF images, and STEM EDS maps for the 5th cycle after conditioning at different points along discharge and charge: a) discharge point 1 (1.35 V), b) discharge point 2 with the arrow indicating ZSH (1.25 V), c) charge point 1 (1.54 V), and d) charge point 2 (1.63 V). The maps shown in the bottom righthand corner for each potential are overlays of Mn, O, Zn, and S. The inset GCD plots depict the positions along the cycle where the battery was stopped for analysis.

Figure S4-5 presents SEM and STEM images and EDS mapping results for discharge and charge during the 5th cycle after conditioning. The results are very similar to those obtained for the first cycle after conditioning. The morphology of the sample shown in the SEM for the first discharge point (1.35 V) in Figure S4-5a is similar to that of the as deposited Mn₃O₄ sample. The STEM EDS mapping shows Mn particles with Zn intercalation and a small amount of S present (from cathode fabrication). There is a small ZSH flake (circled in Figure S4-5a) which may have been left over from previous discharge/charge cycles. The SEM image for the second point of discharge (1.25 V) shows large ZSH flakes present on the sample surface (Figure S4-5b). There is a large Zn-O-S rich area (circled in Figure S4-5b) present in the STEM ADF image that corresponds to ZSH. For the first point during the charge cycle (1.54 V), the large ZSH flakes have mostly dissolved; however, some Z-O-S rich areas remain (circled in Figure S4-5c) that correspond to ZSH. This indicates that there is still some ZSH present near the end of the first recharge plateau. The SEM image for the second point of charge (1.63 V) shows a morphology similar to that of the as deposited Mn₃O₄ and the ZSH flakes have completely dissolved (Figure S4-5d). STEM EDS mapping shows Mn-O-Zn rich areas, with some S, that could correspond to ZnMn₂O₄.

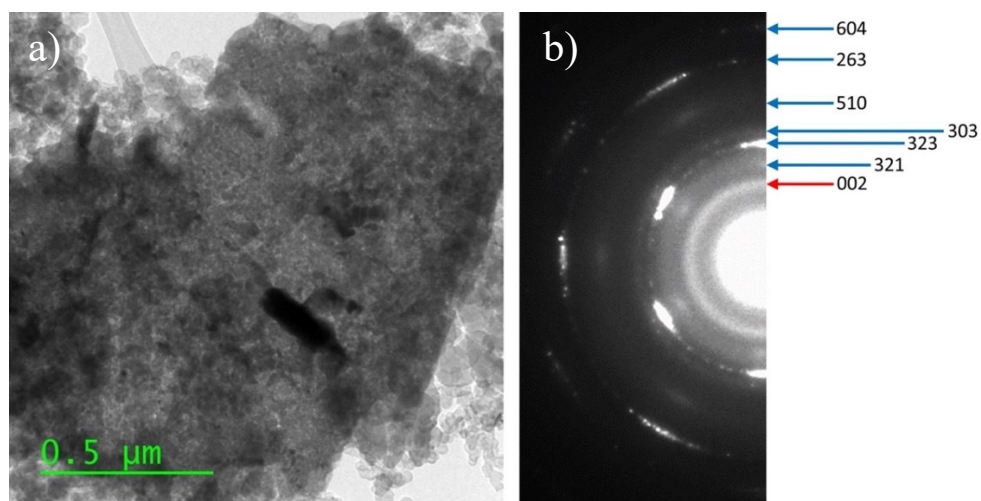


Figure S4-6 a) TEM BF image of a ZSH flake and b) selected area diffraction (SAD) pattern obtained from the ZSH flake. The rings are labeled with corresponding Miller indices. The red arrow represents carbon and the blue arrows represent ZSH (CIF 9001719).

Table S4-1 Indexing of diffracted rings from SAD pattern in Figure S4-7b

d (nm) from SAD pattern	I (rank)	C (hkl)	ZSH d (nm) (CIF 9001719)	ZSH (hkl) (CIF 9001719)	I (%) (CIF 9001719)
0.338	diffuse	002			
0.267	faint		0.265	<u>321</u>	56
0.220	1		0.215	<u>323</u>	36
0.200	faint		0.198	<u>303</u>	3
0.154	faint		0.157	<u>510</u>	70
0.126	2		0.127	<u>263</u>	14
0.109	3		0.109	604	2

Chapter 5: Conclusions and Recommendations

5.1 Conclusions

This thesis presents exploratory work to develop a foundation for the research of zinc-ion batteries (ZIBs) in the Ivey research group. Previously developed electrodepositions techniques were used to fabricate cathode materials for use in ZIBs. Initially, two different electrodeposition techniques were used to fabricate Mn oxide cathodes. Manganese oxide was electrodeposited on stainless steel (SS) substrates and characterized. Following, the cathodes were assembled into ZIBs and underwent electrochemical testing to determine performance. The second study focused on developing a high performing ZIB cathode using a pulsed anodic electrodeposition technique. The Mn oxide was deposited on carbon paper (CP) and initially characterized using several materials techniques. Electrochemical testing was conducted to determine the performance of the cathode when assembled into a ZIB. Finally, combining the materials and electrochemical data, further insight into the reaction mechanism was provided. The main achievements of the work are highlighted in the following subsections.

5.1.1 Mn Oxide on Stainless Steel (SS) Work

Two initial electrodeposition techniques, previously developed in the Ivey research group, were used to deposit Mn oxide materials onto a SS substrate. The first method used was a direct anodic electrodeposition. The deposition resulted in micron-scale Mn oxide rods growing perpendicular from the SS substrate. However, when used as a cathode material for ZIBs, the Mn oxide on SS displayed poor performance and further materials and electrochemical analysis were not pursued. The second method used was a pulsed anodic electrodeposition. The process resulted in a Mn oxide deposit with a flake-like morphology covering the entire surface of the SS. Through XRD analysis, the deposited material was determined to be spinel Mn_3O_4 . When used a cathode in a ZIB, the battery was able to achieve a maximum capacity of 317 mAh g^{-1} at a specific current of 50 mA g^{-1} . Additionally, the battery was able to retain 35.5% of its initial capacity after 35 cycles under an applied specific current of 300 mA g^{-1} . On discharge, a plate-like deposit formed and covered the surface of the cathode, and was identified as zinc sulfate hydroxide (ZSH,

Zn(OH)₂3ZnSO₄*xH₂O). During recharge, the plate-like deposit disappeared, and the surface morphology changed. Further materials and electrochemical analysis were not conducted due to the poor cycling performance of the cathode.

5.1.2 Mn Oxide on Carbon Paper (CP) Work

Continuing with the pulsed anodic electrodeposition explored in the previous study, Mn oxide was successfully deposited onto a CP substrate for use as a cathode in ZIBs. The deposit formed islands on the CP, possessed a flake-like morphology, and was nanocrystalline in nature. Based on a combination of X-ray diffraction (XRD), X-ray photoelectron spectroscopy (XPS), and Raman spectroscopy the deposit was determined to tetragonal Mn₃O₄, which is the stable form of the spinel phase. The assembled ZIB was able to achieve a high capacity of 376 mAh g⁻¹ at a specific current of 50 mA g⁻¹, while achieving a capacity retention of 137% after 200 cycles at a specific current of 1 A g⁻¹. The battery also showed excellent rate capabilities. At 300, 600, 1200, 2400, and then again at 300 mA g⁻¹, the battery was able to deliver capacities of 201, 180, 164, 143, and 217 mAh g⁻¹, respectively. Through a combination of electron microscopy, XPS, and electrochemical testing, additional insight into the reaction mechanism for Mn₃O₄ was obtained and points towards a two-step reaction mechanism. The first discharge plateau most likely involves co-intercalation of Zn²⁺ and H⁺, while the second plateau involves a conversion reaction resulting in the formation of ZSH. The reverse processes occur on charge. Further detailed characterization is required to determine the exact reaction mechanism(s) occurring during battery charge and discharge.

5.2 Future Work and Recommendations

5.2.1 Optimization of the Cathode and ZIB

The anodic electrodeposition technique used to deposit Mn oxide on CP was developed previously in the Ivey group and was not altered for use in ZIBs. However, changing the deposition parameters, including time, additives, temperature, and precursor concentrations can result in dramatic changes in the deposit. This includes, but is not limited to, valence state, morphology, defects, and composition. The deposition parameters can be optimized to improve performance of

the deposit for ZIB applications. Furthermore, the electrolyte of 2 M ZnSO₄ and 0.2 M MnSO₄ was selected based on the most common electrolytes utilized in the literature. By varying the concentration of both components of the electrolyte, the battery performance may be improved. For this work, Zn foil was used as the anode material when assembling ZIBs. However, the literature shows that other forms of Zn, such as electrodeposited Zn on a carbon substrate, can provide improved anode cyclability. Combining cathode improvements with anode and electrolyte optimization may yield a ZIB with improved capacity and cyclability.

5.2.2 Reaction Mechanism(s)

As discussed in Chapter 2 and Chapter 4, the reaction mechanism(s) surrounding Mn oxide materials in ZIBs is still not completely understood. Additionally, studying the reaction mechanism using electrodeposited Mn oxide presents additional challenges, as the phase(s) of the starting material are not known with certainty. Therefore, a systematic approach to studying the reaction mechanism should be employed, using purchased Mn oxides of known phase(s) and composition. Several stages along each of the charge and discharge plateaus should be examined, using various microscopy and spectroscopy methods, as the battery is cycled to provide more insight into the mechanisms. Additionally, other techniques could be employed, such as Raman spectroscopy and XPS, in combination with XRD to aid in material identification. The ZIB studied in Chapter 4 used an electrolyte containing both ZnSO₄ and MnSO₄. Studying the effects of the different electrolyte components separately and together may prove beneficial in understanding the reaction mechanism(s) occurring during charge and discharge.

5.2.3 Synthesis Methods

While electrodeposition is a simple and quick method to deposit materials onto a substrate, other methods may be better suited for battery development. Most commonly, a slurry method is used for the application of active material to a substrate to be used as electrodes for LIBs and ZIBs. While on a laboratory scale this method is time consuming, slurry methods may improve electrode performance as there will be better integration between the active material and other additives. For

example, Mn oxide materials are inherently not very conductive, but mixing with conductive additives such as carbon black has been shown to improve battery performance.

References

- [1] BP, “Statistical Review of World Energy,” 2019.
- [2] J. Ming, J. Guo, C. Xia, W. Wang, and H. N. Alshareef, “Zinc-ion batteries: Materials, mechanisms, and applications,” *Mater. Sci. Eng. R*, vol. 135, pp. 58–84, 2019.
- [3] D. Larcher and J. M. Tarascon, “Towards greener and more sustainable batteries for electrical energy storage,” *Nat. Chem.*, vol. 7, no. 1, pp. 19–29, 2015.
- [4] S. Chu and A. Majumdar, “Opportunities and challenges for a sustainable energy future,” *Nature*, vol. 488, no. 7411, pp. 294–303, 2012.
- [5] Z. Yang, J. Zhang, M. C. W. Kintner-Meyer, X. Lu, D. Choi, J. P. Lemmon, and J. Liu, “Electrochemical Energy Storage for Green Grid,” *Chem. Rev.*, vol. 111, no. 5, pp. 3577–3613, 2011.
- [6] B. Dunn, H. Kamath, and J. M. Tarascon, “Electrical energy storage for the grid: A battery of choices,” *Science (80-.)*, vol. 334, no. 6058, pp. 928–935, 2011.
- [7] R. Guduru and J. Icaza, “A Brief Review on Multivalent Intercalation Batteries with Aqueous Electrolytes,” *Nanomaterials*, vol. 6, no. 3, p. 41, 2016.
- [8] Y. Wang, R. Chen, T. Chen, H. Lv, G. Zhu, L. Ma, C. Wang, Z. Jin, and J. Liu, “Emerging non-lithium ion batteries,” *Energy Storage Mater.*, vol. 4, pp. 103–129, 2016.
- [9] J. Liu, C. Xu, Z. Chen, S. Ni, and Z. X. Shen, “Progress in Aqueous Rechargeable Batteries,” *Green Energy Environ.*, vol. 3, no. 1, pp. 20–41, 2017.
- [10] T. Moynihan, “Samsung Finally Reveals Why the Note 7 Kept Exploding,” *Wired*, 2017. [Online]. Available: <https://www.wired.com/2017/01/why-the-samsung-galaxy-note-7-kept-exploding/>. [Accessed: 13-Jul-2018].
- [11] J. Farchy and M. Gurman, “Apple in talks to buy cobalt directly from miners,” *Bloomberg*, 2018. [Online]. Available: <https://www.bloomberg.com/news/articles/2018-02-21/apple-is-said-to-negotiate-buying-cobalt-direct-from-miners>. [Accessed: 13-Jul-2018].
- [12] B. Tang, L. Shan, S. Liang, and J. Zhou, “Issues and Opportunities Facing Aqueous Zinc-

- ion Batteries,” *Energy Environ. Sci.*, 2019.
- [13] C. Xu, Y. Chen, S. Shi, J. Li, F. Kang, and D. Su, “Secondary batteries with multivalent ions for energy storage,” *Sci Rep*, vol. 5, p. 14120, 2015.
- [14] C. Xu, B. Li, H. Du, and F. Kang, “Energetic zinc ion chemistry: The rechargeable zinc ion battery,” *Angew. Chem. Int. Ed.*, vol. 51, no. 4, pp. 933–935, 2012.
- [15] D. Selvakumaran, A. Pan, S. Liang, and G. Cao, “A review on recent developments and challenges of cathode materials for rechargeable aqueous Zn-ion batteries,” *J. Mater. Chem. A*, vol. 7, no. 31, pp. 18209–18236, 2019.
- [16] M. Song, H. Tan, D. Chao, and H. J. Fan, “Recent Advances in Zn-Ion Batteries,” *Adv. Func. Mater.*, vol. 28, no. 41, p. 1802564, 2018.
- [17] A. Konarov, N. Voronina, J. H. Jo, Z. Bakenov, Y. K. Sun, and S. T. Myung, “Present and Future Perspective on Electrode Materials for Rechargeable Zinc-Ion Batteries,” *ACS Energy Lett.*, vol. 3, no. 10, pp. 2620–2640, 2018.
- [18] D. Linden and T. B. Reddy, *Handbook of Batteries*, 3rd ed. New York, USA: McGraw Hill, 2002.
- [19] J. B. Goodenough, “Battery Fundamentals,” in *Electrochemical Engineering*, T. F. Fuller and J. N. Harb, Eds. Hoboken NJ: John Wiley & Sons, 2018, pp. 151–174.
- [20] R. A. Huggins, *Advanced batteries: Materials science aspects*. New York, USA: Springer Science+Business Media LLC, 2009.
- [21] H. Pan, Y. Shao, P. Yan, Y. Cheng, S. K. Han, Z. Nie, C. Wang, J. Yang, X. Li, P. Bhattacharya, K. T. Mueller, and J. Liu, “Reversible aqueous zinc/manganese oxide energy storage from conversion reactions,” *Nat Energy*, vol. 1, p. 16039, 2016.
- [22] B. Lee, H. R. Seo, H. R. Lee, C. S. Yoon, J. H. Kim, K. Y. Chung, B. W. Cho, and S. H. Oh, “Critical Role of pH Evolution of Electrolyte in the Reaction Mechanism for Rechargeable Zinc Batteries,” *ChemSusChem*, vol. 9, no. 20, pp. 2948–2956, 2016.
- [23] D. C. Hannah, G. Sai Gautam, P. Canepa, and G. Ceder, “On the Balance of Intercalation and Conversion Reactions in Battery Cathodes,” *Adv. Energy Mater.*, vol. 8, no. 20, p. 1800379, 2018.

- [24] N. S. Hudak, "Conversion Electrodes," in *Lithium-Ion Batteries - Advances and Applications*, 1st ed., G. Pistoia, Ed. Elsevier, 2014, pp. 64–65.
- [25] Battery University, "BU-808C: Coulombic and Energy Efficiency with the Battery," 2017. [Online]. Available: http://batteryuniversity.com/learn/article/bu_808c_coulombic_and_energy_efficiency_with_the_battery. [Accessed: 21-May-2018].
- [26] Battery University, "BU-216: Summary Table of Lithium-based Batteries," 2019. [Online]. Available: https://batteryuniversity.com/learn/article/bu_216_summary_table_of_lithium_based_batteries. [Accessed: 14-Nov-2019].
- [27] J. Kang, F. Yan, P. Zhang, and C. Du, "A novel way to calculate energy efficiency for rechargeable batteries," *J. Power Sources*, vol. 206, pp. 310–314, 2012.
- [28] M. H. Alfaruqi, J. Gim, S. Kim, J. Song, J. Jo, S. Kim, V. Mathew, and J. Kim, "Enhanced reversible divalent zinc storage in a structurally stable α -MnO₂ nanorod electrode," *J. Power Sources*, vol. 288, pp. 320–327, 2015.
- [29] Knovel, "Properties of the Elements," *Knovel Critical Tables (2nd Edition)*, 2008. [Online]. Available: <https://app.knovel.com/hotlink/toc/id:kpKCTE000X/knovel-critical-tables/knovel-critical-tables>. [Accessed: 17-May-2018].
- [30] J. Lee, J. B. Ju, W. Il Cho, B. W. Cho, and S. H. Oh, "Todorokite-type MnO₂ as a zinc-ion intercalating material," *Electrochim. Acta*, vol. 112, pp. 138–143, 2013.
- [31] G. Fang, J. Zhou, A. Pan, and S. Liang, "Recent Advances in Aqueous Zinc-ion Batteries," *ACS Energy Lett.*, vol. 3, no. 10, pp. 2480–2501, 2018.
- [32] X. Wu, Y. Xiang, Q. Peng, X. Wu, Y. Li, F. Tang, R. Song, Z. Liu, Z. He, and X. Wu, "Green-low-cost rechargeable aqueous zinc-ion batteries using hollow porous spinel ZnMn₂O₄ as the cathode material," *J. Mater. Chem. A*, vol. 5, pp. 17990–17997, 2017.
- [33] N. Zhang, F. Cheng, Y. Liu, Q. Zhao, K. Lei, C. Chen, X. Liu, and J. Chen, "Cation-Deficient Spinel ZnMn₂O₄ Cathode in Zn(CF₃SO₃)₂ Electrolyte for Rechargeable Aqueous Zn-Ion Battery," *J. Am. Chem. Soc.*, vol. 138, no. 39, pp. 12894–12901, 2016.

- [34] Z. Liu, P. Bertram, and F. Endres, "Bio-degradable zinc-ion battery based on a prussian blue analogue cathode and a bio-ionic liquid-based electrolyte," *J Solid State Electrochem*, vol. 21, no. 7, pp. 2021–2027, 2017.
- [35] T. J. Simons, M. Salsamendi, P. C. Howlett, M. Forsyth, D. R. Macfarlane, and C. Pozo-Gonzalo, "Rechargeable Zn/PEDOT Battery with an Imidazolium-Based Ionic Liquid as the Electrolyte," *ChemElectroChem*, vol. 2, no. 12, pp. 2071–2078, 2015.
- [36] M. S. Chae, J. W. Heo, H. H. Kwak, H. Lee, and S. T. Hong, "Organic electrolyte-based rechargeable zinc-ion batteries using potassium nickel hexacyanoferrate as a cathode material," *J. Power Sources*, vol. 337, pp. 204–211, 2017.
- [37] M. Yan, P. He, Y. Chen, S. Wang, Q. Wei, K. Zhao, X. Xu, Q. An, Y. Shuang, Y. Shao, K. T. Mueller, L. Mai, J. Liu, and J. Yang, "Water-Lubricated Intercalation in $V_2O_5 \cdot nH_2O$ for High-Capacity and High-Rate Aqueous Rechargeable Zinc Batteries," *Adv. Mater.*, vol. 30, no. 1, pp. 1–6, 2018.
- [38] D. Kundu, B. D. Adams, V. Duffort, S. H. Vajargah, and L. F. Nazar, "A high-capacity and long-life aqueous rechargeable zinc battery using a metal oxide intercalation cathode," *Nat Energy*, vol. 1, p. 16119, 2016.
- [39] W. Sun, F. Wang, S. Hou, C. Yang, X. Fan, Z. Ma, T. Gao, F. Han, R. Hu, M. Zhu, and C. Wang, "Zn/MnO₂ Battery Chemistry With H^+ and Zn^{2+} Coinsertion," *J. Am. Chem. Soc.*, vol. 139, no. 29, pp. 9775–9778, 2017.
- [40] N. Zhang, F. Cheng, J. Liu, L. Wang, X. Long, X. Liu, F. Li, and J. Chen, "Rechargeable aqueous zinc-manganese dioxide batteries with high energy and power densities," *Nat Commun*, vol. 8, no. 1, p. 405, 2017.
- [41] B. Jiang, C. Xu, C. Wu, L. Dong, J. Li, and F. Kang, "Manganese Sesquioxide as Cathode Material for Multivalent Zinc Ion Battery with High Capacity and Long Cycle Life," *Electrochim. Acta*, vol. 229, pp. 422–428, 2017.
- [42] J. Hao, J. Mou, J. Zhang, L. Dong, W. Liu, C. Xu, and F. Kang, "Electrochemically induced spinel-layered phase transition of Mn_3O_4 in high performance neutral aqueous rechargeable zinc battery," *Electrochim. Acta*, vol. 259, pp. 170–178, 2018.
- [43] L. Dong, X. Ma, Y. Li, L. Zhao, W. Liu, J. Cheng, C. Xu, B. Li, Q. H. Yang, and F. Kang,

- “Extremely safe, high-rate and ultralong-life zinc-ion hybrid supercapacitors,” *Energy Storage Mater.*, vol. 13, pp. 96–102, 2018.
- [44] C. Xia, J. Guo, Y. Lei, H. Liang, C. Zhao, and H. N. Alshareef, “Rechargeable Aqueous Zinc-Ion Battery Based on Porous Framework Zinc Pyrovanadate Intercalation Cathode,” *Adv. Mater.*, vol. 30, p. 1705580, 2018.
- [45] B. Lee, H. R. Lee, H. Kim, K. Y. Chung, B. W. Cho, and S. H. Oh, “Elucidating the intercalation mechanism of zinc ions into α -MnO₂ for rechargeable zinc batteries,” *Chem. Commun.*, vol. 51, no. 45, pp. 9265–9268, 2015.
- [46] R. Trócoli and F. La Mantia, “An aqueous zinc-ion battery based on copper hexacyanoferrate,” *ChemSusChem*, vol. 8, no. 3, pp. 481–485, 2015.
- [47] D. Xu, B. Li, C. Wei, Y. B. He, H. Du, X. Chu, X. Qin, Q. H. Yang, and F. Kang, “Preparation and characterization of MnO₂/acid-treated CNT nanocomposites for energy storage with zinc ions,” *Electrochim. Acta*, vol. 133, pp. 254–261, 2014.
- [48] Z. Jia, B. Wang, and Y. Wang, “Copper hexacyanoferrate with a well-defined open framework as a positive electrode for aqueous zinc ion batteries,” *Mater. Chem. Phys.*, vol. 149, pp. 601–606, 2015.
- [49] L. Zhang, L. Chen, X. Zhou, and Z. Liu, “Towards high-voltage aqueous metal-ion batteries beyond 1.5 V: The zinc/zinc hexacyanoferrate system,” *Adv. Energy Mater.*, vol. 5, no. 2, pp. 1–5, 2015.
- [50] Y. Xia, D. Zhu, S. Si, D. Li, and S. Wu, “Nickel foam-supported polyaniline cathode prepared with electrophoresis for improvement of rechargeable Zn battery performance,” *J. Power Sources*, vol. 283, pp. 125–131, 2015.
- [51] Fisher Scientific, “Zinc trifluoromethanesulfonate, 98%, ACROS Organics™.” [Online]. Available: <https://www.fishersci.ca/shop/products/zinc-trifluoromethanesulfonate-98-acros-organics-2/p-3756745#?keyword=zinc+triflate>. [Accessed: 04-Jun-2018].
- [52] Fisher Scientific, “Alfa Aesar™ Zinc sulfate heptahydrate, 98%.” [Online]. Available: <https://www.fishersci.ca/shop/products/zinc-sulfate-heptahydrate-98-2/p-7020831#?keyword=zinc+sulfate+98%25>. [Accessed: 04-Jun-2018].

- [53] M. H. Alfaruqi, S. Islam, J. Gim, J. Song, S. Kim, D. T. Pham, J. Jo, Z. Xiu, V. Mathew, and J. Kim, "A high surface area tunnel-type α -MnO₂ nanorod cathode by a simple solvent-free synthesis for rechargeable aqueous zinc-ion batteries," *Chem. Phys. Lett.*, vol. 650, pp. 64–68, 2016.
- [54] M. H. Alfaruqi, S. Islam, D. Y. Putro, V. Mathew, S. Kim, J. Jo, S. Kim, Y. K. Sun, K. Kim, and J. Kim, "Structural transformation and electrochemical study of layered MnO₂ in rechargeable aqueous zinc-ion battery," *Electrochim. Acta*, vol. 276, pp. 1–11, 2018.
- [55] M. H. Alfaruqi, V. Mathew, J. Gim, S. Kim, J. Song, J. P. Baboo, S. H. Choi, and J. Kim, "Electrochemically Induced Structural Transformation in a γ -MnO₂ Cathode of a High Capacity Zinc-Ion Battery System," *Chem. Mater.*, vol. 27, no. 10, pp. 3609–3620, 2015.
- [56] B. Lee, C. S. Yoon, H. R. Lee, K. Y. Chung, B. W. Cho, and S. H. Oh, "Electrochemically-induced reversible transition from the tunneled to layered polymorphs of manganese dioxide," *Sci Rep*, vol. 4, p. 6066, 2014.
- [57] C. Xu, H. Du, B. Li, F. Kang, and Y. Zeng, "Reversible Insertion Properties of Zinc Ion into Manganese Dioxide and Its Application for Energy Storage," *Electrochem. Solid-State Lett.*, vol. 12, no. 4, pp. A61–A65, 2009.
- [58] C. Xu, S. W. Chiang, J. Ma, and F. Kang, "Investigation on Zinc Ion Storage in Alpha Manganese Dioxide for Zinc Ion Battery by Electrochemical Impedance Spectrum," *J. Am. Chem. Soc.*, vol. 160, no. 1, pp. A93–A97, 2012.
- [59] C. Yuan, Y. Zhang, Y. Pan, X. Liu, G. Wang, and D. Cao, "Investigation of the intercalation of polyvalent cations (Mg²⁺, Zn²⁺) into λ -MnO₂ for rechargeable aqueous battery," *Electrochim. Acta*, vol. 116, pp. 404–412, 2014.
- [60] W. Wei, X. Cui, W. Chen, and D. G. Ivey, "Manganese oxide-based materials as electrochemical supercapacitor electrodes," *Chem. Soc. Rev.*, vol. 40, no. 3, pp. 1697–1721, 2011.
- [61] S. Devaraj and N. Munichandraiah, "Effect of crystallographic structure of MnO₂ on its electrochemical capacitance properties," *J. Phys. Chem. C*, vol. 112, no. 11, pp. 4406–4417, 2008.
- [62] V. Soundharrajan, B. Sambandam, S. S. S. S. S. Kim, V. Mathew, J. Jo, S. S. S. S. S. Kim,

- J. Lee, S. Islam, K. Kim, Y. K. K. Sun, and J. Kim, "Aqueous Magnesium Zinc Hybrid Battery: An Advanced High-Voltage and High-Energy MgMn_2O_4 Cathode," *ACS Energy Lett.*, vol. 3, no. 8, pp. 1998–2004, 2018.
- [63] J. Huang, Z. Wang, M. Hou, X. Dong, Y. Liu, Y. Wang, and Y. Xia, "Polyaniline-intercalated manganese dioxide nanolayers as a high-performance cathode material for an aqueous zinc-ion battery," *Nat Commun*, vol. 9, no. 1, pp. 1–8, 2018.
- [64] N. Qiu, H. Chen, Z. Yang, S. Sun, and Y. Wang, "Synthesis of manganese-based complex as cathode material for aqueous rechargeable batteries," *RSC Adv.*, vol. 8, no. 28, pp. 15703–15708, 2018.
- [65] Y. Zeng, X. Zhang, Y. Meng, M. Yu, J. Yi, Y. Wu, X. Lu, and Y. Tong, "Achieving Ultrahigh Energy Density and Long Durability in a Flexible Rechargeable Quasi-Solid-State Zn– MnO_2 Battery," *Adv. Mater.*, vol. 29, no. 26, pp. 1–7, 2017.
- [66] S. Yang, M. Zhang, X. Wu, X. Wu, F. Zeng, Y. Li, S. Duan, D. Fan, Y. Yang, and X. Wu, "The excellent electrochemical performances of $\text{ZnMn}_2\text{O}_4/\text{Mn}_2\text{O}_3$: The composite cathode material for potential aqueous zinc ion batteries," *J. Electroanal. Chem.*, vol. 832, no. August 2018, pp. 69–74, 2019.
- [67] Y. Huang, J. Mou, W. Liu, X. Wang, L. Dong, F. Kang, and C. Xu, "Novel Insights into Energy Storage Mechanism of Aqueous Rechargeable Zn/ MnO_2 Batteries with Participation of Mn^{2+} ," *Nano-Micro Lett.*, vol. 11, no. 1, p. 49, 2019.
- [68] G. Sun, X. Jin, H. Yang, J. Gao, and L. Qu, "An aqueous Zn– MnO_2 rechargeable microbattery," *J. Mater. Chem. A*, vol. 6, no. 23, pp. 10926–10931, 2018.
- [69] D. C. Golden, C. C. Chen, and J. B. Dixon, "Transformation of Birnessite to Buserite, Todorokite, and Manganite Under Mild Hydrothermal Treatment," *Clays Clay Miner.*, vol. 35, no. 4, pp. 271–280, 1987.
- [70] J. E. Post, "Manganese oxide minerals : Crystal structures and economic and environmental significance," *Proc. Natl. Acad. Sci.*, vol. 96, pp. 3447–3454, 1999.
- [71] Y. Li, S. Wang, J. R. Salvador, J. Wu, B. Liu, W. Yang, J. Yang, W. Zhang, J. Liu, and J. Yang, "Reaction Mechanisms for Long-Life Rechargeable Zn/ MnO_2 Batteries," *Chem. Mater.*, vol. 31, pp. 2036–2047, 2019.

- [72] S. Islam, M. H. Alfaruqi, J. Song, S. Kim, D. T. Pham, J. Jo, S. Kim, V. Mathew, J. P. Baboo, Z. Xiu, and J. Kim, "Carbon-coated manganese dioxide nanoparticles and their enhanced electrochemical properties for zinc-ion battery applications," *J. Energy Chem.*, vol. 26, no. 4, pp. 815–819, 2017.
- [73] B. Wu, G. Zhang, M. Yan, T. Xiong, P. He, L. He, X. Xu, and L. Mai, "Graphene Scroll-Coated α -MnO₂ Nanowires as High-Performance Cathode Materials for Aqueous Zn-Ion Battery," *Small*, vol. 14, no. 13, pp. 1–8, 2018.
- [74] W. Qiu, Y. Li, A. You, Z. Zhang, G. Li, X. Lu, and Y. Tong, "High-performance flexible quasi-solid-state Zn-MnO₂ battery based on MnO₂ nanorod arrays coated 3D porous nitrogen-doped carbon cloth," *J. Mater. Chem. A*, vol. 5, no. 28, pp. 14838–14846, 2017.
- [75] Y. Huang, J. Liu, Q. Huang, Z. Zheng, P. Hiralal, F. Zheng, D. Ozgit, S. Su, S. Chen, P.-H. Tan, S. Zhang, and H. Zhou, "Flexible high energy density zinc-ion batteries enabled by binder-free MnO₂/reduced graphene oxide electrode," *npj Flex. Electron.*, vol. 2, no. 1, 2018.
- [76] Z. Liu, G. Pulletikurthi, and F. Endres, "A Prussian Blue/Zinc Secondary Battery with a Bio-Ionic Liquid-Water Mixture as Electrolyte," *ACS Appl. Mater. Interfaces*, vol. 8, no. 19, pp. 12158–12164, 2016.
- [77] R. Y. Wang, B. Shyam, K. H. Stone, J. N. Weker, M. Pasta, H. W. Lee, M. F. Toney, and Y. Cui, "Reversible Multivalent (Monovalent, Divalent, Trivalent) Ion Insertion in Open Framework Materials," *Adv. Energy Mater.*, vol. 5, no. 12, pp. 1–10, 2015.
- [78] P. He, Y. Quan, X. Xu, M. Yan, W. Yang, Q. An, L. He, and L. Mai, "High-Performance Aqueous Zinc-Ion Battery Based on Layered H₂V₃O₈ Nanowire Cathode," *Small*, vol. 13, no. 47, p. 1702551, 2017.
- [79] P. Hu, M. Yan, T. Zhu, X. Wang, X. Wei, J. Li, L. Zhou, Z. Li, L. Chen, and L. Mai, "Zn/V₂O₅ Aqueous Hybrid-Ion Battery with High Voltage Platform and Long Cycle Life," *ACS Appl. Mater. Interfaces*, vol. 9, no. 49, pp. 42717–42722, 2017.
- [80] J. Zhou, L. Shan, Z. Wu, X. Guo, G. Fang, and S. Liang, "Investigation of V₂O₅ as a low-cost rechargeable aqueous zinc ion battery cathode," *Chem. Commun.*, vol. 54, no. 35, pp. 4457–4460, 2018.

- [81] N. Zhang, Y. Dong, M. Jia, X. Bian, Y. Wang, M. Qiu, J. Xu, Y. Liu, L. Jiao, and F. Cheng, "Rechargeable Aqueous Zn-V₂O₅ Battery with High Energy Density and Long Cycle Life," *ACS Energy Lett.*, vol. 3, no. 6, pp. 1366–1372, 2018.
- [82] X. Chen, L. Wang, H. Li, F. Cheng, and J. Chen, "Porous V₂O₅ nanofibers as cathode materials for rechargeable aqueous zinc-ion batteries," *J. Energy Chem.*, vol. 38, pp. 20–25, 2019.
- [83] J. Zhao, H. Ren, Q. Liang, D. Yuan, S. Xi, C. Wu, W. Manalastas, J. Ma, W. Fang, Y. Zheng, C.-F. Du, M. Srinivasan, and Q. Yan, "High-performance flexible quasi-solid-state zinc-ion batteries with layer-expanded vanadium oxide cathode and zinc/stainless steel mesh composite anode," *Nano Energy*, vol. 62, no. April, pp. 94–102, 2019.
- [84] H. Qin, L. Chen, L. Wang, X. Chen, and Z. Yang, "V₂O₅ hollow spheres as high rate and long life cathode for aqueous rechargeable zinc ion batteries," *Electrochim. Acta*, vol. 306, pp. 307–316, 2019.
- [85] J. L. Domingo, "Vanadium: A review of the reproductive and developmental toxicity," *Reprod. Toxicol.*, vol. 10, no. 3, pp. 175–182, 1996.
- [86] D. G. Barceloux, "Vanadium," *J. Toxicol. - Clin. Toxicol.*, vol. 37, no. 2, pp. 265–278, 1999.
- [87] F. Wan, L. Zhang, X. Dai, X. Wang, Z. Niu, and J. Chen, "Aqueous rechargeable zinc/sodium vanadate batteries with enhanced performance from simultaneous insertion of dual carriers," *Nat Commun*, vol. 9, no. 1, pp. 1656–1667, 2018.
- [88] T. Wei, Q. Li, G. Yang, and C. Wang, "High-rate and durable aqueous zinc ion battery using dendritic V₁₀O₂₄·12H₂O cathode material with large interlamellar spacing," *Electrochim. Acta*, vol. 287, pp. 60–67, 2018.
- [89] D. Kundu, S. Hosseini Vajargah, L. Wan, B. Adams, D. Prendergast, and L. F. Nazar, "Aqueous: Vs. nonaqueous Zn-ion batteries: Consequences of the desolvation penalty at the interface," *Energy Environ. Sci.*, vol. 11, no. 4, pp. 881–892, 2018.
- [90] B. Tang, G. Fang, J. Zhou, L. Wang, Y. Lei, C. Wang, T. Lin, Y. Tang, and S. Liang, "Potassium vanadates with stable structure and fast ion diffusion channel as cathode for rechargeable aqueous zinc-ion batteries," *Nano Energy*, vol. 51, pp. 579–587, 2018.

- [91] W. Kaveevivitchai and A. Manthiram, "High-capacity zinc-ion storage in an open-tunnel oxide for aqueous and nonaqueous Zn-ion batteries," *J. Mater. Chem. A*, vol. 4, no. 48, pp. 18737–18741, 2016.
- [92] X. Guo, G. Fang, W. Zhang, J. Zhou, L. Shan, L. Wang, C. Wang, T. Lin, Y. Tang, and S. Liang, "Mechanistic Insights of Zn²⁺ Storage in Sodium Vanadates," *Adv. Energy Mater.*, vol. 1801819, p. 1801819, 2018.
- [93] W. Li, K. Wang, S. Cheng, and K. Jiang, "A long-life aqueous Zn-ion battery based on Na₃V₂(PO₄)₂F₃ cathode," *Energy Storage Mater.*, vol. 15, pp. 14–21, 2018.
- [94] P. Hu, T. Zhu, X. Wang, X. Zhou, X. Wei, X. Yao, W. Luo, C. Shi, K. A. Owusu, L. Zhou, and L. Mai, "Aqueous Zn//Zn(CF₃SO₃)₂//Na₃V₂(PO₄)₃ batteries with simultaneous Zn²⁺/Na⁺ intercalation/de-intercalation," *Nano Energy*, vol. 58, no. January, pp. 492–498, 2019.
- [95] G. Li, Z. Yang, Y. Jiang, C. Jin, W. Huang, X. Ding, and Y. Huang, "Towards polyvalent ion batteries: A zinc-ion battery based on NASICON structured Na₃V₂(PO₄)₃," *Nano Energy*, vol. 25, pp. 211–217, 2016.
- [96] H. B. Zhao, C. J. Hu, H. W. Cheng, J. H. Fang, Y. P. Xie, W. Y. Fang, T. N. L. Doan, T. K. A. Hoang, J. Q. Xu, and P. Chen, "Novel rechargeable M₃V₂(PO₄)₃//Zinc (M = Li, Na) hybrid aqueous batteries with excellent cycling performance," *Sci Rep*, vol. 6, no. April, pp. 1–10, 2016.
- [97] Q. Zhao, W. Huang, Z. Luo, L. Liu, Y. Lu, Y. Li, L. Li, J. Hu, H. Ma, and J. Chen, "High-capacity aqueous zinc batteries using sustainable quinone electrodes," *Sci. Adv.*, vol. 4, no. 3, 2018.
- [98] Y. Liang, Y. Jing, S. Gheytani, K. Y. Lee, P. Liu, A. Facchetti, and Y. Yao, "Universal quinone electrodes for long cycle life aqueous rechargeable batteries," *Nat Mater*, vol. 16, no. 8, pp. 841–848, 2017.
- [99] Y. Cheng, L. Luo, L. Zhong, J. Chen, B. Li, W. Wang, S. X. Mao, C. Wang, V. L. Sprenkle, G. Li, and J. Liu, "Highly Reversible Zinc-Ion Intercalation into Chevrel Phase Mo₆S₈ Nanocubes and Applications for Advanced Zinc-Ion Batteries," *ACS Appl. Mater. Interfaces*, vol. 8, no. 22, pp. 13673–13677, 2016.

- [100] M. S. Chae, J. W. Heo, S. C. Lim, and S. T. Hong, "Electrochemical Zinc-Ion Intercalation Properties and Crystal Structures of ZnMo₆S₈ and Zn₂Mo₆S₈ Chevrel Phases in Aqueous Electrolytes," *Inorg. Chem.*, vol. 55, no. 7, pp. 3294–3301, 2016.
- [101] W. Xu, K. Zhao, and Y. Wang, "Electrochemical activated MoO₂/Mo₂N heterostructured nanobelts as superior zinc rechargeable battery cathode," *Energy Storage Mater.*, vol. 15, no. June, pp. 374–379, 2018.
- [102] W. Liu, J. Hao, C. Xu, J. Mou, L. Dong, F. Jiang, Z. Kang, J. Wu, B. Jiang, and F. Kang, "Investigation of zinc ion storage of transition metal oxides, sulfides, and borides in zinc ion battery systems," *Chem. Commun.*, vol. 53, no. 51, pp. 6872–6874, 2017.
- [103] B. Zhang, Y. Liu, X. Wu, Y. Yang, Z. Chang, Z. Wen, and Y. Wu, "An aqueous rechargeable battery based on zinc anode and Na_{0.95}MnO₂," *Chem. Commun.*, vol. 50, no. 10, pp. 1209–1211, 2014.
- [104] F. Wang, Y. Liu, X. Wang, Z. Chang, Y. Wu, and R. Holze, "Aqueous Rechargeable Battery Based on Zinc and a Composite of LiNi_{1/3}Co_{1/3}Mn_{1/3}O₂," *ChemElectroChem*, vol. 2, no. 7, pp. 1024–1030, 2015.
- [105] F. Wang, F. Yu, X. Wang, Z. Chang, L. Fu, Y. Zhu, Z. Wen, Y. Wu, and W. Huang, "Aqueous Rechargeable Zinc/Aluminum Ion Battery with Good Cycling Performance," *ACS Appl. Mater. Interfaces*, vol. 8, no. 14, pp. 9022–9029, 2016.
- [106] T. Athar, "Metal Oxide Nanopowder," in *Emerging Nanotechnologies for Manufacturing*, W. Ahmed and M. J. Jackson, Eds. Oxford, UK: Elsevier, 2009, pp. 325–353.
- [107] S.-J. Cho, M.-J. Uddin, and P. Alaboina, "Review of Nanotechnology for Cathode Materials in Batteries," in *Emerging Nanotechnologies in Rechargeable Energy Storage Systems*, L. M. Rodriguez-Martinez and N. Omar, Eds. Amsterdam, Netherlands: Elsevier, 2017, pp. 83–129.
- [108] I. Baker, "Magnetic nanoparticle synthesis," in *Nanobiomaterials - Nanostructured Materials for Biomedical Applications*, R. Narayan, Ed. Duxford, UK: Woodhead Publishing, 2018, pp. 197–229.
- [109] G. H. A. Therese and P. V. Kamath, "Electrochemical synthesis of metal oxides and hydroxides," *Chem. Mater.*, vol. 12, no. 5, pp. 1195–1204, 2000.

- [110] Y. Parcharoen and S. Sirivisoot, "Surface modifications of orthopedic implant materials using an electroplating process," in *Biomedical Nanomaterials - From Design to Implementation*, T. J. Webster and Y. Hilal, Eds. London, UK: The Institution of Engineering and Technology, 2016, pp. 25–36.
- [111] F. Nasirpouri, *Electrodeposition of Nanostructured Materials*, Vol 62. Cham, Switzerland: Springer International Publishing, 2017.
- [112] P. Senguttuvan, S. D. Han, S. Kim, A. L. Lipson, S. Tepavcevic, T. T. Fister, I. D. Bloom, A. K. Burrell, and C. S. Johnson, "A High Power Rechargeable Nonaqueous Multivalent Zn/V₂O₅Battery," *Adv. Energy Mater.*, vol. 6, no. 24, 2016.
- [113] D. Chen, X. Rui, Q. Zhang, H. Geng, L. Gan, W. Zhang, C. Li, S. Huang, and Y. Yu, "Persistent zinc-ion storage in mass-produced V₂O₅ architectures," *Nano Energy*, vol. 60, no. March, pp. 171–178, 2019.
- [114] L. Shan, Y. Yang, W. Zhang, H. Chen, G. Fang, J. Zhou, and S. Liang, "Observation of combination displacement/intercalation reaction in aqueous zinc-ion battery," *Energy Storage Mater.*, no. July, pp. 0–1, 2018.
- [115] J. S. Ko, M. B. Sassin, J. F. Parker, D. R. Rolison, and J. W. Long, "Combining battery-like and pseudocapacitive charge storage in 3D MnOx@carbon electrode architectures for zinc-ion cells," *Sustain. Energy Fuels*, pp. 626–636, 2018.
- [116] C. Xia, J. Guo, P. Li, X. Zhang, and H. N. Alshareef, "Highly Stable Aqueous Zinc-Ion Storage Using a Layered Calcium Vanadium Oxide Bronze Cathode," *Angew. Chem. Int. Ed.*, vol. 57, no. 15, pp. 3943–3948, 2018.
- [117] L. Ma, S. Chen, H. Li, Z. Ruan, Z. Tang, Z. Liu, Z. Wang, Y. Huang, Z. Pei, J. A. Zapien, and C. Zhi, "Initiating a mild aqueous electrolyte Co₃O₄/Zn battery with 2.2 V-high voltage and 5000-cycle lifespan by a Co(III) rich-electrode," *Energy Environ. Sci.*, vol. 11, no. 9, pp. 2521–2530, 2018.
- [118] Y. Yang, Y. Tang, S. Liang, Z. Wu, G. Fang, X. Cao, C. Wang, T. Lin, A. Pan, and J. Zhou, "Transition metal ion-preintercalated V₂O₅ as high-performance aqueous zinc-ion battery cathode with broad temperature adaptability," *Nano Energy*, vol. 61, no. April, pp. 617–625, 2019.

- [119] Q. Pang, C. Sun, Y. Yu, K. Zhao, Z. Zhang, P. M. Voyles, G. Chen, Y. Wei, and X. Wang, "H₂V₃O₈ Nanowire/Graphene Electrodes for Aqueous Rechargeable Zinc Ion Batteries with High Rate Capability and Large Capacity," *Adv. Energy Mater.*, vol. 8, no. 19, pp. 1–9, 2018.
- [120] B. Sambandam, V. Soundharrajan, S. Kim, M. H. Alfaruqi, J. Jo, S. Kim, V. Mathew, Y. K. Sun, and J. Kim, "K₂V₆O₁₆·2.7H₂O nanorod cathode: An advanced intercalation system for high energy aqueous rechargeable Zn-ion batteries," *J. Mater. Chem. A*, vol. 6, no. 32, pp. 15530–15539, 2018.
- [121] L. Zhang, L. Chen, X. Zhou, and Z. Liu, "Morphology-Dependent Electrochemical Performance of Zinc Hexacyanoferrate Cathode for Zinc-Ion Battery," *Sci Rep*, vol. 5, no. July, pp. 1–11, 2015.
- [122] F. Wang, E. Hu, W. Sun, T. Gao, X. Ji, X. Fan, F. Han, X. Q. Yang, K. Xu, and C. Wang, "A rechargeable aqueous Zn²⁺-battery with high power density and a long cycle-life," *Energy Environ. Sci.*, vol. 11, no. 11, pp. 3168–3175, 2018.
- [123] M. H. Alfaruqi, V. Mathew, J. Song, S. Kim, S. Islam, D. T. Pham, J. Jo, S. Kim, J. P. Baboo, Z. Xiu, K. S. Lee, Y. K. Sun, and J. Kim, "Electrochemical Zinc Intercalation in Lithium Vanadium Oxide: A High-Capacity Zinc-Ion Battery Cathode," *Chem. Mater.*, vol. 29, no. 4, pp. 1684–1694, 2017.
- [124] W. Xu, K. Zhao, W. Huo, Y. Wang, G. Yao, X. Gu, H. Cheng, L. Mai, C. Hu, and X. Wang, "Diethyl ether as self-healing electrolyte additive enabled long-life rechargeable aqueous zinc ion batteries," *Nano Energy*, vol. 62, no. April, pp. 275–281, 2019.
- [125] M. Chamoun, W. R. Brant, C. W. Tai, G. Karlsson, and D. Noréus, "Rechargeability of aqueous sulfate Zn/MnO₂ batteries enhanced by accessible Mn²⁺ ions," *Energy Storage Mater.*, vol. 15, no. December 2017, pp. 351–360, 2018.
- [126] X. Yu, Y. Fu, X. Cai, H. Kafafy, H. Wu, M. Peng, S. Hou, Z. Lv, S. Ye, and D. Zou, "Flexible fiber-type zinc-carbon battery based on carbon fiber electrodes," *Nano Energy*, vol. 2, no. 6, pp. 1242–1248, 2013.
- [127] Y. Fu, Q. Wei, G. Zhang, X. Wang, J. Zhang, Y. Hu, D. Wang, L. Zuin, T. Zhou, Y. Wu, and S. Sun, "High-Performance Reversible Aqueous Zn-Ion Battery Based on Porous

- MnO_x Nanorods Coated by MOF-Derived N-Doped Carbon,” *Adv. Energy Mater.*, vol. 1801445, p. 1801445, 2018.
- [128] H. Liang, Z. Cao, F. Ming, W. Zhang, D. H. Anjum, Y. Cui, L. Cavallo, and H. N. Alshareef, “Aqueous Zinc-Ion Storage in MoS₂ by Tuning the Intercalation Energy,” *Nano Lett.*, 2019.
- [129] B. She, L. Shan, H. Chen, J. Zhou, X. Guo, G. Fang, X. Cao, and S. Liang, “Investigation of sodium vanadate as a high-performance aqueous zinc-ion battery cathode,” *J. Energy Chem.*, vol. 37, pp. 172–175, 2019.
- [130] P. He, G. Zhang, X. Liao, M. Yan, X. Xu, Q. An, J. Liu, and L. Mai, “Sodium Ion Stabilized Vanadium Oxide Nanowire Cathode for High-Performance Zinc-Ion Batteries,” *Adv. Energy Mater.*, vol. 8, no. 10, pp. 1–6, 2018.
- [131] Y. Cai, F. Liu, Z. Luo, G. Fang, J. Zhou, A. Pan, and S. Liang, “Pilotaxitic Na_{1.1}V₃O_{7.9} nanoribbons/graphene as high-performance sodium ion battery and aqueous zinc ion battery cathode,” *Energy Storage Mater.*, vol. 13, no. January, pp. 168–174, 2018.
- [132] P. Hu, T. Zhu, X. Wang, X. Wei, M. Yan, J. Li, W. Luo, W. Yang, W. Zhang, L. Zhou, Z. Zhou, and L. Mai, “Highly Durable Na₂V₆O₁₆·1.63H₂O Nanowire Cathode for Aqueous Zinc-Ion Battery,” *Nano Lett.*, vol. 18, no. 3, pp. 1758–1763, 2018.
- [133] V. Soundharajan, B. Sambandam, S. Kim, M. H. Alfaruqi, D. Y. Putro, J. Jo, S. Kim, V. Mathew, Y. K. Sun, and J. Kim, “Na₂V₆O₁₆·3H₂O Barnesite Nanorod: An Open Door to Display a Stable and High Energy for Aqueous Rechargeable Zn-Ion Batteries as Cathodes,” *Nano Lett.*, vol. 18, no. 4, pp. 2402–2410, 2018.
- [134] D. Kundu, P. Oberholzer, C. Glaros, A. Bouzid, E. Tervoort, A. Pasquarello, and M. Niederberger, “Organic Cathode for Aqueous Zn-Ion Batteries: Taming a Unique Phase Evolution toward Stable Electrochemical Cycling,” *Chem. Mater.*, vol. 30, no. 11, pp. 3874–3881, 2018.
- [135] G. Dawut, Y. Lu, L. Miao, and J. Chen, “High-performance rechargeable aqueous Zn-ion batteries with a poly(benzoquinonyl sulfide) cathode,” *Inorg. Chem. Front.*, vol. 5, no. 6, pp. 1391–1396, 2018.

- [136] C. Zhu, G. Fang, J. Zhou, J. Guo, Z. Wang, C. Wang, J. Li, Y. Tang, and S. Liang, “Binder-free stainless steel@Mn₃O₄ nanoflower composite: A high-activity aqueous zinc-ion battery cathode with high-capacity and long-cycle-life,” *J. Mater. Chem. A*, vol. 6, no. 20, pp. 9677–9683, 2018.
- [137] J. H. Jo, Y.-K. Sun, and S.-T. Myung, “Hollandite-type Al-doped VO_{1.52}(OH)_{0.77} as a zinc ion insertion host material,” *J. Mater. Chem. A*, vol. 5, no. 18, pp. 8367–8375, 2017.
- [138] Y. Li, Z. Huang, P. K. Kalambate, Y. Zhong, Z. Huang, M. Xie, Y. Shen, and Y. Huang, “V₂O₅ nanopaper as a cathode material with high capacity and long cycle life for rechargeable aqueous zinc-ion battery,” *Nano Energy*, vol. 60, no. January, pp. 752–759, 2019.
- [139] F. Liu, Z. Chen, G. Fang, Z. Wang, Y. Cai, B. Tang, J. Zhou, and S. Liang, “V₂O₅ Nanospheres with Mixed Vanadium Valences as High Electrochemically Active Aqueous Zinc-Ion Battery Cathode,” *Nano-Micro Lett.*, vol. 11, no. 1, p. 25, 2019.
- [140] J. Shin, D. S. Choi, H. J. Lee, Y. Jung, and J. W. Choi, “Hydrated Intercalation for High-Performance Aqueous Zinc Ion Batteries,” *Adv. Energy Mater.*, vol. 1900083, pp. 1–11, 2019.
- [141] J. Ding, Z. Du, L. Gu, B. Li, L. Wang, S. Wang, and Y. Gong, “Ultrafast Zn²⁺ Intercalation and Deintercalation in Vanadium Dioxide,” *Adv. Mater.*, vol. 30, no. 1800762, pp. 1–6, 2018.
- [142] P. He, M. Yan, G. Zhang, R. Sun, L. Chen, Q. An, and L. Mai, “Layered VS₂ Nanosheet-Based Aqueous Zn Ion Battery Cathode,” *Adv. Energy Mater.*, vol. 7, no. 11, pp. 2–6, 2017.
- [143] J. Wang, J. G. Wang, H. Liu, C. Wei, and F. Kang, “Zinc ion stabilized MnO₂ nanospheres for high capacity and long lifespan aqueous zinc-ion batteries,” *J. Mater. Chem. A*, vol. 7, no. 22, pp. 13727–13735, 2019.
- [144] B. Sambandam, V. Soundharrajan, S. Kim, M. H. Alfaruqi, J. Jo, S. Kim, V. Mathew, Y. K. Sun, and J. Kim, “Aqueous rechargeable Zn-ion batteries: An imperishable and high-energy Zn₂V₂O₇ nanowire cathode through intercalation regulation,” *J. Mater. Chem. A*, vol. 6, no. 9, pp. 3850–3856, 2018.

- [145] S. Zhao, B. Han, D. Zhang, Q. Huang, L. Xiao, L. Chen, D. G. Ivey, Y. Deng, and W. Wei, “Unravelling the reaction chemistry and degradation mechanism in aqueous Zn/MnO₂ rechargeable batteries,” *J. Mater. Chem. A*, vol. 6, no. 14, pp. 5733–5739, 2018.
- [146] K. Lu, B. Song, Y. Zhang, H. Ma, and J. Zhang, “Encapsulation of zinc hexacyanoferrate nanocubes with manganese oxide nanosheets for high-performance rechargeable zinc ion batteries,” *J. Mater. Chem. A*, vol. 5, no. 45, pp. 23628–23633, 2017.
- [147] F. Mo, H. Li, Z. Pei, G. Liang, L. Ma, Q. Yang, D. Wang, Y. Huang, and C. Zhi, “A smart safe rechargeable zinc ion battery based on sol-gel transition electrolytes,” *Sci. Bull.*, vol. 63, no. 16, pp. 1077–1086, 2018.
- [148] N. Palaniyandy, M. A. Kebede, K. Raju, K. I. Ozoemena, L. le Roux, M. K. Mathe, and R. Jayaprakasam, “ α -MnO₂ nanorod/onion-like carbon composite cathode material for aqueous zinc-ion battery,” *Mater. Chem. Phys.*, vol. 230, no. June 2018, pp. 258–266, 2019.
- [149] H. Li, C. Han, Y. Huang, Y. Huang, M. Zhu, Z. Pei, Q. Xue, Z. Wang, Z. Liu, Z. Tang, Y. Wang, F. Kang, B. Li, and C. Zhi, “An extremely safe and wearable solid-state zinc ion battery based on a hierarchical structured polymer electrolyte,” *Energy Environ. Sci.*, vol. 11, no. 4, pp. 941–951, 2018.
- [150] L. Zhao, L. Dong, W. Liu, and C. Xu, “Binary and Ternary Manganese Dioxide Composites Cathode for Aqueous Zinc-ion Battery,” *ChemistrySelect*, vol. 3, no. 44, pp. 12661–12665, Nov. 2018.
- [151] S. Islam, M. H. Alfaruqi, V. Mathew, J. Song, S. Kim, S. Kim, J. Jo, J. P. Baboo, D. T. Pham, D. Y. Putro, Y. K. Sun, and J. Kim, “Facile synthesis and the exploration of the zinc storage mechanism of β -MnO₂ nanorods with exposed (101) planes as a novel cathode material for high performance eco-friendly zinc-ion batteries,” *J. Mater. Chem. A*, vol. 5, no. 44, pp. 23299–23309, 2017.
- [152] Z. Deng, J. Huang, J. Liu, L. Ren, L. Zhu, X. Xiao, and M. Tan, “ β -MnO₂ nanolayer coated on carbon cloth as a high-activity aqueous zinc-ion battery cathode with high-capacity and long-cycle-life,” *Mater. Lett.*, vol. 248, pp. 207–210, 2019.
- [153] G. G. Kumar and S. Sampath, “Electrochemical characterization of

- poly(vinylidene fluoride)-zinc triflate gel polymer electrolyte and its application in solid-state zinc batteries,” *Solid State Ionics*, vol. 160, no. 3–4, pp. 289–300, 2003.
- [154] X. Guo, J. Li, X. Jin, Y. Han, Y. Lin, Z. Lei, S. Wang, L. Qin, S. Jiao, and R. Cao, “A Hollow-Structured Manganese Oxide Cathode for Stable Zn-MnO₂ Batteries,” *Nanomaterials*, vol. 8, no. 5, p. 301, 2018.
- [155] S. D. Han, S. Kim, D. Li, V. Petkov, H. D. Yoo, P. J. Phillips, H. Wang, J. J. Kim, K. L. More, B. Key, R. F. Klie, J. Cabana, V. R. Stamenkovic, T. T. Fister, N. M. Markovic, A. K. Burrell, S. Tepavcevic, and J. T. Vaughey, “Mechanism of Zn Insertion into Nanostructured δ -MnO₂: A Nonaqueous Rechargeable Zn Metal Battery,” *Chem. Mater.*, vol. 29, no. 11, pp. 4874–4884, 2017.
- [156] M. Eckert, W. Peters, J.-F. Drillet, M. Eckert, W. Peters, and J.-F. Drillet, “Fast Microwave-Assisted Hydrothermal Synthesis of Pure Layered δ -MnO₂ for Multivalent Ion Intercalation,” *Materials (Basel)*, vol. 11, no. 12, p. 2399, 2018.
- [157] M. H. Alfaruqi, J. Gim, S. Kim, J. Song, D. T. Pham, J. Jo, Z. Xiu, V. Mathew, and J. Kim, “A layered δ -MnO₂ nanoflake cathode with high zinc-storage capacities for eco-friendly battery applications,” *Electrochem. commun.*, vol. 60, pp. 121–125, 2015.
- [158] C. Guo, H. Liu, J. Li, Z. Hou, J. Liang, J. Zhou, Y. Zhu, and Y. Qian, “Ultrathin δ -MnO₂ nanosheets as cathode for aqueous rechargeable zinc ion battery,” *Electrochim. Acta*, vol. 304, pp. 370–377, 2019.
- [159] S. Khamsanga, R. Pornprasertsuk, T. Yonezawa, A. A. Mohamad, and S. Kheawhom, “ δ -MnO₂ nanoflower/graphite cathode for rechargeable aqueous zinc ion batteries,” *Sci Rep*, vol. 9, no. 1, p. 8441, 2019.
- [160] Y. Leng, *Materials Characterization: Introduction to Microscopic and Spectroscopic Methods*, 2nd ed. Weinheim, Germany: Wiley-VCH, 2013.
- [161] J. I. Goldstein, D. E. Newbury, J. R. Michael, N. W. M. Ritchie, J. H. J. Scott, and D. C. Joy, *Scanning Electron Microscopy and X-Ray Microanalysis*, 4th ed. New York, USA: Springer-Verlag, 2018.
- [162] B. J. Inkson, “Scanning Electron Microscopy (SEM) and Transmission Electron Microscopy (TEM) for Materials Characterization,” in *Materials Characterization Using*

- Nondestructive Evaluation (NDE) Methods*, G. Hübschen, I. Altpeter, R. Tschuncky, and H.-G. Herrmann, Eds. Duxford, UK, UK: Elsevier Ltd, 2016, pp. 17–43.
- [163] Z. Gou and T. Li, *Fundamentals and Applications of Nanomaterials*. Norwood, USA: Artech House, 2009.
- [164] D. B. Williams and C. B. Carter, *Transmission Electron Microscopy: A Textbook for Materials Science*, 2nd Editio. New York, NY: Springer Science+Business Media LLC, 2009.
- [165] B. Fultz and J. M. Howe, *Transmission Electron Microscopy and Diffractometry of Materials*, 3rd Editio. Springer-Verlag Berlin Heidelberg, 2008.
- [166] Y. Huang, “X-ray Photoelectron Spectroscopy (XPS),” in *Nanocomposite Coatings and Nanocomposite Materials*, A. Ochsner, W. Ahmed, and N. Ali, Eds. Zurich, Switzerland: Trans Tech Publications LTD, 2009, pp. 77–81.
- [167] E. Smith and G. Dent, *Modern Raman Spectroscopy – A Practical Approach*. West Sussex: John Wiley & Sons, 2005.
- [168] D. J. Gardiner, P. R. Graves, H. J. Bowley, D. L. Gerrard, J. D. Loudon, and G. Turrell, *Practical Raman Spectroscopy*. Springer-Verlag Berlin Heidelberg, 1989.
- [169] S. N. Lvov, *Introduction to Electrochemical Science and Engineering*. Boca Raton, USA: CRC Press, 2014.
- [170] A. J. Bard and L. R. Faulkner, *Electrochemical Methods: Fundamentals and Applications*, 2nd Ed. John Wiley & Sons, 2001.
- [171] D. A. C. Brownson and C. E. Banks, “Interpreting Electrochemistry,” in *The Handbook of Graphene Electrochemistry*, 1st ed., Springer London, 2014, pp. 23–77.
- [172] R. O’hayre, S.-W. Cha, W. G. Colella, and F. B. Prinz, *Fuel Cell Fundamentals*, 3rd ed. Hoboken, USA: John Wiley & Sons, 2016.
- [173] D. Pletcher, R. Greff, R. Peat, L. M. Peter, and J. Robinson, “Potential sweep techniques and cyclic voltammetry,” in *Instrumental Methods in Electrochemistry*, Woodhead Publishing, 2010, pp. 178–228.
- [174] Y. Zhu and C. Wang, “Galvanostatic intermittent titration technique for phase-

- transformation electrodes,” *J. Phys. Chem. C*, vol. 114, no. 6, pp. 2830–2841, 2010.
- [175] W. Weppner and R. A. Huggins, “Electrochemical investigation of the chemical diffusion, partial ionic conductivities, and other kinetic parameters in Li_3Sb and Li_3Bi ,” *J. Solid State Chem.*, vol. 22, no. 3, pp. 297–308, 1977.
- [176] E. Markevich, M. D. Levi, and D. Aurbach, “Comparison between potentiostatic and galvanostatic intermittent titration techniques for determination of chemical diffusion coefficients in ion-insertion electrodes,” *J. Electroanal. Chem.*, vol. 580, no. 2, pp. 231–237, 2005.
- [177] L. Chen, Z. Yang, H. Qin, X. Zeng, and J. Meng, “Advanced electrochemical performance of $\text{ZnMn}_2\text{O}_4/\text{N}$ -doped graphene hybrid as cathode material for zinc ion battery,” *J. Power Sources*, vol. 425, pp. 162–169, 2019.
- [178] Metrohm, “Galvanostatic Intermittent Titration Technique,” 2018. [Online]. Available: <https://www.metrohm.com/en/applications/AN-BAT-003#>. [Accessed: 12-Oct-2019].
- [179] B. Babakhani and D. G. Ivey, “Anodic deposition of manganese oxide electrodes with rod-like structures for application as electrochemical capacitors,” *J. Power Sources*, vol. 195, no. 7, pp. 2110–2117, 2010.
- [180] M. P. Clark, W. Qu, and D. G. Ivey, “Nanostructured manganese oxide and manganese oxide/polyethylenedioxythiophene rods electrodeposited onto nickel foam for supercapacitor applications,” *J Appl Electrochem*, vol. 47, no. 1, pp. 39–49, 2017.
- [181] M. Clark and D. G. Ivey, “Nucleation and growth of electrodeposited Mn oxide rods for supercapacitor electrodes,” *Nanotechnology*, vol. 26, no. 38, p. 384001, 2015.
- [182] M. Xiong and D. G. Ivey, “Sequentially Electrodeposited $\text{MnO}_x/\text{Co-Fe}$ as Bifunctional Electrocatalysts for Rechargeable Zinc-Air Batteries,” *J. Am. Chem. Soc.*, vol. 164, no. 6, pp. A1012–A1021, 2017.
- [183] M. Xiong, M. P. Clark, M. Labbe, and D. G. Ivey, “A horizontal zinc-air battery with physically decoupled oxygen evolution/reduction reaction electrodes,” *J. Power Sources*, vol. 393, pp. 108–118, 2018.
- [184] ASTM International, “B254 - Standard Practice for Preparation of and Electroplating on

Stainless Steel.”

- [185] H. J. Van Hook and M. L. Keith, “The System $\text{Fe}_3\text{O}_4\text{-Mn}_3\text{O}_4$,” *Am. Mineral.*, vol. 43, no. 56, pp. 69–83, 1958.
- [186] D. Chao, C. (Rose) Zhu, M. Song, P. Liang, X. Zhang, N. H. Tiep, H. Zhao, J. Wang, R. Wang, H. Zhang, and H. J. Fan, “A High-Rate and Stable Quasi-Solid-State Zinc-Ion Battery with Novel 2D Layered Zinc Orthovanadate Array,” *Adv. Mater.*, vol. 30, no. 32, pp. 1–7, 2018.
- [187] X. Chen, L. Wang, H. Li, F. Cheng, and J. Chen, “Porous V_2O_5 nanofibers as cathode materials for rechargeable aqueous zinc-ion batteries,” *J. Energy Chem.*, vol. 38, pp. 20–25, 2019.
- [188] G. G. Yadav, J. Cho, D. Turney, B. Hawkins, X. Wei, J. Huang, S. Banerjee, and M. Nyce, “Going beyond Intercalation Capacity of Aqueous Batteries by Exploiting Conversion Reactions of Mn and Zn electrodes for Energy-Dense Applications,” *Adv. Energy Mater.*, vol. 1902270, 2019.
- [189] D. Aasen, M. Clark, and D. G. Ivey, “A Gas Diffusion Layer Impregnated with Mn_3O_4 -Decorated N-Doped Carbon Nanotubes for the Oxygen Reduction Reaction in Zinc-Air Batteries,” *Batter. Supercaps*, vol. 2, pp. 1–13, 2019.
- [190] G. Fang, C. Zhu, M. Chen, J. Zhou, B. Tang, X. Cao, X. Zheng, A. Pan, and S. Liang, “Suppressing Manganese Dissolution in Potassium Manganate with Rich Oxygen Defects Engaged High-Energy-Density and Durable Aqueous Zinc-Ion Battery,” *Adv. Func. Mater.*, 2019.
- [191] V. Soundharajan, B. Sambandam, S. Kim, V. Mathew, J. Jo, S. Kim, J. Lee, S. Islam, K. Kim, Y. K. Sun, and J. Kim, “Aqueous Magnesium Zinc Hybrid Battery: An Advanced High-Voltage and High-Energy MgMn_2O_4 Cathode,” *ACS Energy Lett.*, vol. 3, no. 8, pp. 1998–2004, 2018.
- [192] D. Chao, W. Zhou, C. Ye, Q. Zhang, Y. Chen, L. Gu, K. Davey, and S. Z. Qiao, “An Electrolytic Zn– MnO_2 Battery for High-Voltage and Scalable Energy Storage,” *Angew. Chemie - Int. Ed.*, vol. 58, no. 23, pp. 7823–7828, 2019.
- [193] M. Chigane and M. Ishikawa, “Manganese oxide thin film preparation by potentiostatic

- electrolyses and electrochromism,” *J. Am. Chem. Soc.*, vol. 147, no. 6, pp. 2246–2251, 2000.
- [194] T. Gao, H. Fjellvåg, and P. Norby, “A comparison study on Raman scattering properties of α - and β -MnO₂,” *Anal. Chim. Acta*, vol. 648, no. 2, pp. 235–239, 2009.
- [195] J. Jiang and A. Kucernak, “Electrochemical supercapacitor material based on manganese oxide: Preparation and characterization,” *Electrochim. Acta*, vol. 47, no. 15, pp. 2381–2386, 2002.
- [196] R. V. Siriwardane and J. A. Poston, “Interaction of H₂S with zinc titanate in the presence of H₂ and CO,” *Appl. Surf. Sci.*, vol. 45, no. 2, pp. 131–139, 1990.
- [197] G. Deroubaix and P. Marcus, “X-ray photoelectron spectroscopy analysis of copper and zinc oxides and sulphides,” *Surf. Interface Anal.*, vol. 18, no. 1, pp. 39–46, 1992.
- [198] B. R. Strohmeier and D. M. Hercules, “Surface spectroscopic characterization of the interaction between zinc ions and γ -alumina,” *J. Catal.*, vol. 86, no. 2, pp. 266–279, 1984.
- [199] V. I. Nefedov, “A comparison of results of an ESCA study of nonconducting solids using spectrometers of different constructions,” *J. Electron Spectros. Relat. Phenomena*, vol. 25, no. 1, pp. 29–47, 1982.
- [200] N. Guo, X. Q. Wei, X. L. Deng, and X. J. Xu, “Synthesis and property of spinel porous ZnMn₂O₄ microspheres,” *Nanoscale Res. Lett.*, vol. 356, pp. 1127–1134, 2015.
- [201] M. C. Biesinger, B. P. Payne, A. P. Grosvenor, L. W. M. Lau, A. R. Gerson, and R. S. C. Smart, “Resolving surface chemical states in XPS analysis of first row transition metals, oxides and hydroxides: Cr, Mn, Fe, Co and Ni,” *Appl. Surf. Sci.*, vol. 257, no. 7, pp. 2717–2730, 2011.